Structure Analysis of Adsorbates on Single Crystal Surfaces using Photoelectron Diffraction

Gareth Nisbet

Supervised by Dr C.L.A. Lamont

A thesis submitted to the University of Huddersfield
in partial fulfilment of the requirements for
the degree of Doctor of Philosophy

The University of Huddersfield in collaboration with the
Fritz-Haber-Institut der Max-Planck-Gesellschaft

October 2007

Abstract

The structural determination of the Pt(111)c(5x√3)rect.-CO phase formed by 0.6 ML of adsorbed CO has been undertaken using scanned-energy mode photoelectron diffraction utilising the two distinct components of the C 1s photoemission peak. Earlier assignments of CO to atop and bridge sites have been confirmed as well as the respective 2:1 ratio of these assignments. Additionally, quantitative local structural details have been obtained. In particular, the Pt-C chemisorption bond lengths for the atop and bridging sites are 1.86 ± 0.02 Å and 2.02 ± 0.04 Å respectively. These values are similar to those obtained in previous studies for the 0.5 ML coverage c(4 x 2) phase involving an atop:bridge occupation ratio of 1:1. The results also indicate a definite tilt in the atop CO species of 10.7º +1.5º/-3.1º consistent with earlier investigations using electron-stimulated desorption ion angular distribution, LEED, Monte Carlo simulations and IR.

The local structure of benzene adsorbed on Si(001) has also been investigated using scanned energy photoelectron diffraction. The standard butterfly (SB), tilted (T), tight bridge (TB), pedestal (P), twisted bridge (TB), and diagonal bridge butterfly (DDB) models were optimized and compared with the lowest R-factors being achieved for SB and TB models (0.2337 and 0.2641 respectively). Further optimization was performed for a mixed overlayer (0.25 ML) consisting of SB and TB structures in various proportions. A significant improvement in the R-factor was achieved for a combined model in which 58 ± 35 % of the overlayer is composed of the SB structure.

Using the structural data for the CO/Pt(111), and benzene/Si(001) adsorption systems, comparative simulations have been undertaken to explore the effect of using vertically and horizontally polarized radiation on PhD modulation amplitudes and more importantly the sensitivity of each method to various structural parameters.

It has been shown theoretically that perpendicularly polarized photoelectron diffraction (PPPhD) yields modulation functions with intensities often being several times those observed in PhD. The new technique is shown to be more sensitive when the parameters involve mainly lateral displacements. The sensitivity of PhD on the other hand exceeds that of PPPhD only when dealing with bond lengths involving mainly vertical displacements. Parameters involving similar vertical and lateral displacements show similar sensitivities for both methods. Despite potential weaknesses such as a reduced signal to noise ratio and the sensitivity of PPPhD to the sample positioning, the potential gains of this technique especially when considering systems in which the adsorbates lie across the substrate such as benzene adsorbed on Si(001), make it ripe for experimental validation.

Index

1 Introduction

A major driving force for studying chemical reactions on surfaces is the need to understand heterogeneous catalysis. The sheer scale of the subject's significance can be expressed in the fact that heterogeneous catalysis is involved in literally billions of pounds worth of economic activity [1].

A catalyst is 'an active chemical spectator' [2], while it speeds up a reaction it cannot affect the position of equilibrium of a reversible reaction, and is chemically unchanged at the end of the reaction. A good catalyst can not only speed up a reaction but can do it selectively.

Heterogeneous reactions occur at the interface between systems in different phases. Gas-solid and liquid-solid interfaces are of particular interest because it is on the solid surface that catalytic substances can be deposited (if the solid, itself, is not the catalyst) and thereby immobilised. The obvious benefit of this is that the catalyst isn't lost in the stream of products resulting in expensive recovery techniques. Furthermore, for some applications outside of the lab or chemical plant such as catalytic converters in car exhaust systems, the use of heterogeneous catalysis is essential.

A better understanding of heterogeneous catalysis may lie in the accurate structural determination of relevant surfaces and the molecules adsorbed on them. To this end, a detailed structural analysis of the economically significant CO/Pt adsorption system has been undertaken, more specifically CO adsorption on Pt(111).

Another area of surface science which is of increasing interest is the area of nanotechnology especially in the context of the semiconductor industry which in February 2006 accounted for an annualised $238 billion in global sales [3]. Gordon Moore, a co-founder of Intel made an observation in 1965 which has now become known as Moore's Law. Moore's Law states that in effect the progress of technological development is such that, the complexity of integrated circuits (IC) doubles every 18 months. This was revised in 1975 allowing two years for each technological leap [4, 5].

As the demand for faster, smaller and more efficient computers increases, surface interactions become more and more relevant.

Recent AMD (Advanced Micro Devices) technology utilises copper interconnects which previously proved impossible to implement since the copper was found to diffuse into the silicon dioxide layers [6]. When critical dimensions in the region of 62 nm are required, this becomes a significant problem. However the problem has been circumvented by coating the chip with a barrier layer after photolithography [7] to prevent the copper from reacting with the silicon dioxide. As the miniaturisation of IC technology continues further, the interfacial areas will undoubtedly increase with respect to the bulk material, highlighting the necessity of atomic scale surface analysis. One of the problems that naturally arise with increased IC complexity and faster clock cycles is that of heat dissipation; the lack of which can have a detrimental effect on the semiconducting properties of silicon based semiconductors. While this can be resolved to some extent by the use of various heat dissipation techniques such as pneumatic or liquid (water or liquid nitrogen) cooling, another approach is to use a semiconductor which is more stable at higher temperatures. A strong candidate material for such a semiconductor is diamond [8]. Diamond is a wide band-gap semiconductor and as such retains its semiconducting properties at higher temperatures. The diamond can be produced artificially by heating ordinary carbon to around 1500 K under a pressure of 50,000 bar but this is an expensive process. Another method is to use chemical vapour deposition to build the diamond on a suitable substrate. One potentially suitable precursor for this process is benzene adsorbed on Si(001) [9]. An important step in ascertaining the suitability of such a system for this application is the detailed determination of the adsorption behaviour and structure. This has been undertaken in this thesis and is detailed in chapter 5.

Clearly, atomic scale structural analysis is technologically important and for this reason amongst others, many surface analysis techniques have been developed in recent years. These include surface XRD (X-ray diffraction), LEED (low energy electron diffraction), and PhD (photoelectron diffraction). PhD has been used in this project because of its advantages over the other techniques. For example, XRD relies on diffraction as does PhD, however PhD relies on the diffraction of core level electrons not photons and therefore has the added advantage of being element specific. LEED, while similar to PhD in that it relies on the diffraction of electrons, is not element specific and is further limited by the fact that it requires long range order in the overlayer. Furthermore, the incident electron beam is more destructive than the ‘soft’ X-ray radiation used in PhD.

The aim of this project is in part, the structural determination of the above mentioned adsorbate/substrate systems using PhD, and also to use the analysis of these systems to explore the feasibility of a new technique built upon PhD using out of plane polarized radiation. As will be discussed in section 2.2.2, PhD uses the interference between a directly emitted reference wave component and the scattered wave components. However when analysing systems in which the substrate is a weak photoelectron scatterer such as Pt or Si, the reference wave can be excessively dominant meaning some of the finer structural details can be lost. By using out of plane polarized radiation the reference wave is removed altogether leaving only the scattered components and thereby potentially exposing previously inaccessible structural information (see chapter 6).

Before these aims can be meaningfully discussed some background to the theoretical concepts of XPS, PhD and LEED is necessary.

2 Theory

2.1 XPS (X-ray Photoelectron Spectroscopy)

2.1.1 Principles of XPS

Core level electrons have a binding energy corresponding to that of photons in the soft X-ray region. When a material absorbs a photon with an energy greater than the binding energy of a core level electron, the electron, now referred to as a photoelectron, is ejected. The binding energy and the photon energy are related by the equation:

$$E_K = h\nu - E_B \qquad 2.1$$

Where: E_K = Kinetic energy of the photoelectron (J)
h = Planks Constant (6.6261×10^{-34} J.s)
ν = Frequency of photon radiation (Hz)
E_B = Binding Energy (J)

In order for photoemission to occur, the photoelectron must possess sufficient energy not only to free itself from the atom but also from the material's surface. This additional energy is equal to the work function potential (ϕ). Thus the equation becomes:

$$E_K = h\nu - E_B - \phi \qquad 2.2$$

Where: ϕ = Work Function (J)

The energies involved in equations 2.1 and 2.2 are small and are more conveniently expressed in electron volts (1 eV = 1.60219 x 10^{-19} J).

A typical value for the work function of a transition metal lies in the region of a few eV, for example 6.35, 5.01, 4.7 for Pt, Ni and Cu, respectively [10]. The use of the work function is complicated by the fact that it is not only a property of the material but also the geometry of the material's surface and whatever atoms or molecules are adsorbed onto it. However, while significant, the work function for a given material is small, and the variations even smaller, when compared with the differences in the core level binding energies for any successive element and certainly for those used in this project. For example, C 1s, N 1s, and O 1s have respective binding energies of 284.2 eV, 409.9 eV and 543.1 eV [11].

Deep core electrons do not participate in bonding and are therefore characteristic of the atoms from which they come, thus making XPS an excellent tool for elemental analysis. In addition to this, XPS can distinguish between different species of the same element. This is possible due to small yet detectable shifts in the core level binding energies. These chemical shifts depend on the atom's environment and in particular, the oxidation state of the atom [12]. This can be explained by the following argument.

The electron binding energy, E_B, is given by the Einstein equation:

$$E_B = h\nu - E_K \qquad 2.3$$

This is simply a rearrangement of equation 2.1 but can also be expressed in terms of the energy difference between the initial and final energy states of the atom,

$$E_B = E_f(n-1) - E_i(n) \qquad 2.4$$

where $E_i(n)$ is the initial state energy and $E_f(n-1)$ is the final state energy. If there was no relaxation of the spectator electrons and no extra-atomic relaxation, the binding energy would simply be equal to the negative of the orbital energy of the initial state of the electron and only a single peak for a given element would be observed. The fact that this is not the case is what gives XPS its extra versatility. The atom does experience electronic relaxation along with some extra-atomic relaxation, factors which are both influenced by the atom's coordination. The extent of this influence is manifested in a shift in the binding energy. In general, the binding energy increases with oxidation state and with the electron withdrawing power of the substituents bound to the atom.

2.1.2 XPS Measurements

When a sample is irradiated by monochromatic radiation of energy sufficient to eject a core level electron, an array of electrons of different energies is emitted. These electrons originate from a range of orbitals of lower binding energy than the target orbital. Take for example, CO adsorbed on Pt. If the C 1s orbital is targeted, C 2s and the C 2p electrons will also be ejected, as well as O 2s, O 2p, and Pt 4f (and above) electrons (see fig.2.1). A suitable detector, such as the Omicron EA 125 HR, which has a resolution of less than 5 meV, can easily distinguish between these photoelectrons. Distinguishing between core level electrons for the same element in different geometries is more difficult. For example the chemical shift for C 1s is 0.7 eV when comparing CO adsorbed in atop and bridged positions, which lies well within the resolution of the analyser. The difficulty however is due to the fact that the signal recorded is a superposition of both elastically and inelastically scattered electrons. The result is a spreading of the signal or a broadening of the peak representing the signal leading to an overlap of the discrete peaks for each species. Another factor which can contribute to this problem is the monochromator resolution. This was one of the reasons the above mentioned system could not be measured at BESSY I (a second generation synchrotron). When measured at BESSY II (a third generation synchrotron), a more sophisticated monochromator of better resolution was used. The broadening was reduced and the peaks were clearly distinguishable as shown in fig.2.2.

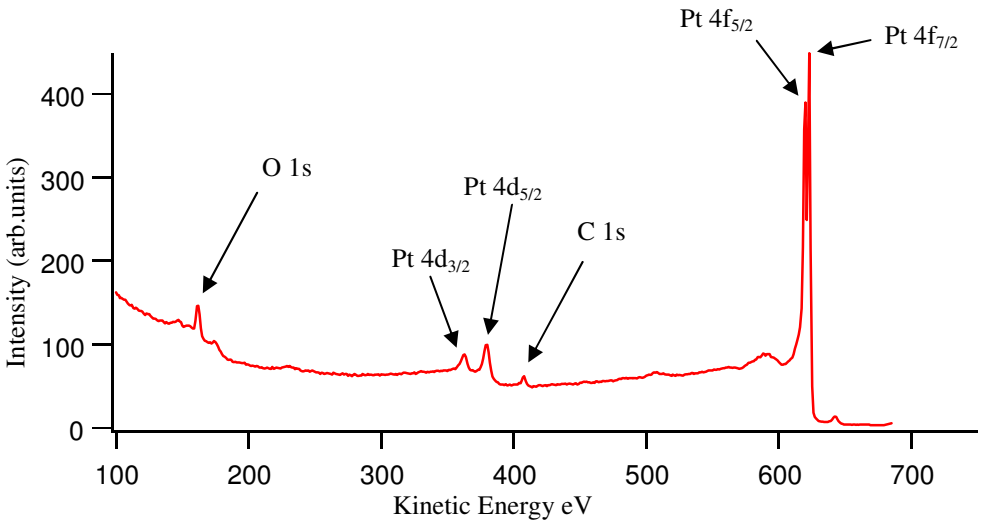

Fig.2.1 XPS for Pt (111) measured with a photon energy of 700 eV. The C 2s, O 2s and O 2p with binding energies of 7 eV, 18.2 eV and 23.1 eV respectively, are too weak to be visible at this magnification.

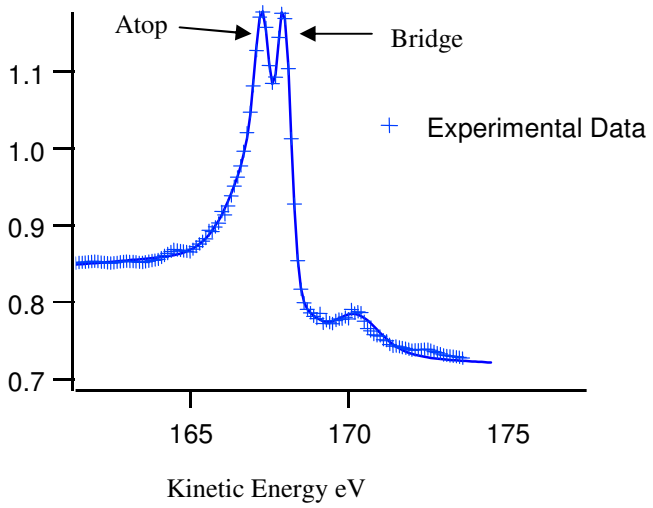

Fig.2.2 C 1s XPS spectrum showing the chemical shift for CO adsorbed in two different sites on Pt(111), namely atop and bridge. The spectrum represents the kinetic energy of the photo-emitted C 1s electrons for each species measured with a photon energy of 450eV.

2.2 X-Ray Photoelectron Diffraction

When the directly emitted component and the scattered component of a photoelectron interact, they add together, by way of superposition resulting in constructive and destructive interference. A diffraction pattern is produced which is characteristic of the photoelectron energy, the emission angle, and the local geometry of the emitting atom. While XPS is

sensitive to these parameters, when they are varied or scanned, XPS becomes X-ray photoelectron diffraction.

X-ray photoelectron diffraction can be divided into two sub-techniques namely, angle scanned photoelectron diffraction referred to as XPD, and scanned energy photoelectron diffraction referred to as PhD.

2.2.1 XPD

XPD is based on the use of a specific energy, optimised for the target material. The sample is rotated during the measurement (see fig.2.3) producing an angle dependent signature from which certain structural information can be inferred.

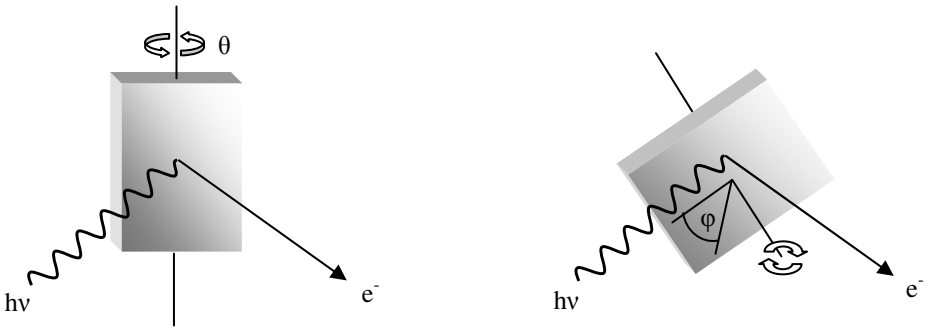

Fig.2.3 The sample can be rotated about an angle θ (polar angle), changing the angle of incidence and emission, or about an angle φ (azimuth angle), changing the alignment of the crystal atoms and adsorbates with respect to the analyser.

Fig.2.4 shows that the square modulus of the cross section, which determines the scattering intensity in the absence of wave interference, is always at a maximum at 0^o (the scattering atom is between the emitting atom and the analyser (see fig.2.5).

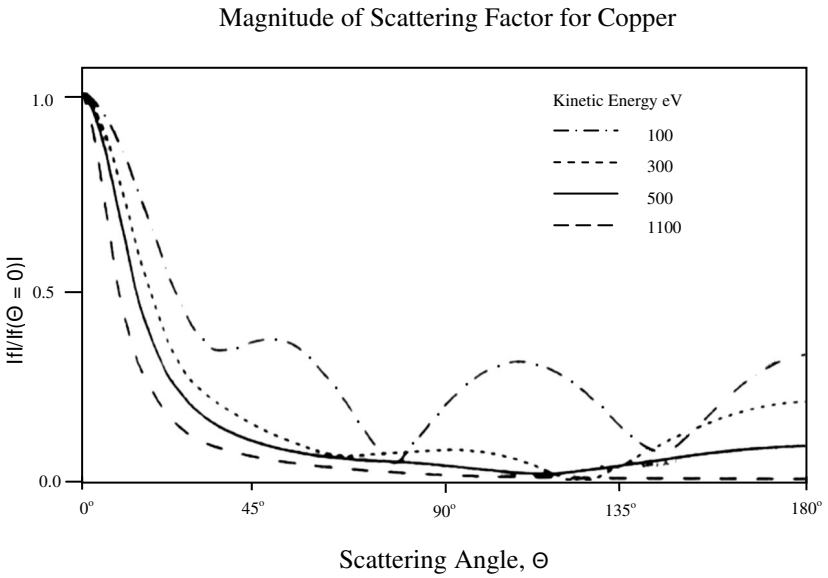

Fig.2.4 Modulus of the electron scattering factor of a Cu atom as a function of scattering angle for several different electron energies [13].

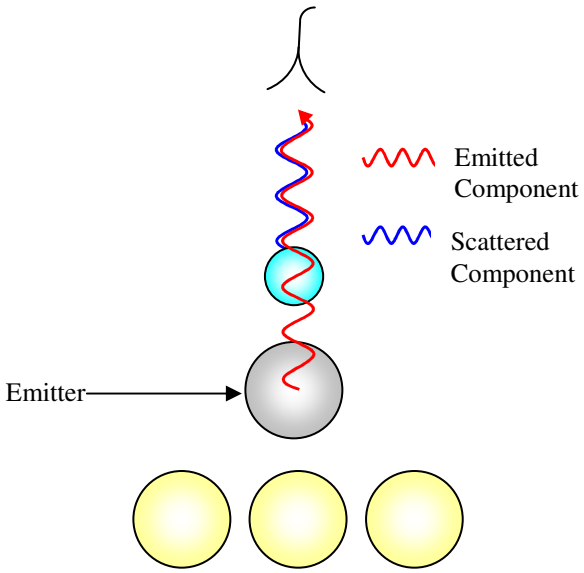

Fig.2.5. Forward scattering (scattering at 0^{o}) at normal emission. There is no pathlength difference between the directly emitted component and the scattered component of the photoelectron.

This is because the pathlengths for the directly emitted and scattered components of the photoelectron are the same, which always leads to constructive interference. Although, strictly speaking, the phase shift of the scattered component, which is energy dependant, influences the

degree of constructive interference. The scattering cross section peak becomes more dominant at 0^o for higher energies as well as becoming sharper and thereby, more sensitive to the angle of emission. This makes XPD an effective tool in the determination of molecular orientation, and the relative displacement of the substrate and overlayer atoms in ultra thin film growth [14]. XPD however only works in a two-atom situation were the emitter is distinguishable from substrate bulk such as the example depicted in fig.2.4. Overlayers composed of single atom adsorbates can be analysed through a chemical shift in the substrate atoms involved in adsorption. Although it is often the case, especially with physisorption, that no measurable chemical shift is observed. This problem is circumvented in PhD.

2.2.2 PhD

While XPD relies on forward scattering or zero order diffraction i.e. zero pathlength difference (see fig.2.4), PhD relies on back scattering and non-zero order diffraction, exploiting real pathlength differences. At 180^o, the backscattering direction (the emitting atom is between the scattering atom and the analyser), the scattering intensity is virtually non existent in the higher energy region. However at energies lower than 100 eV, the scattering intensity increases to around one third of that at 0^o (fig.2.5).

A 2D representation of the single electron model used to describe the diffraction in PhD is depicted in fig.2.6.

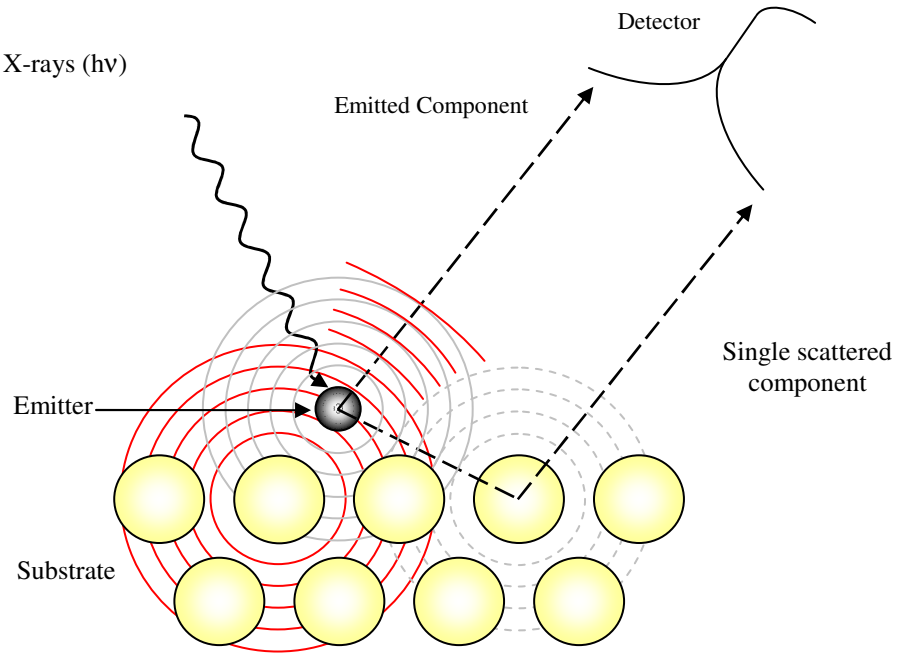

Fig.2.6 2D representation of the single electron model for photoelectron diffraction. The overlap of the radial lines represents constructive interference.

When a photoelectron is liberated, it can be emitted in any direction, the probability of which can be represented two dimensionally by concentric circles about the emitting atom. The circles represent a given phase in the wave cycle of the photoelectron. The scattered component of the photoelectron can be represented in the same way with concentric circles about the scattering atoms. However, due to a difference in the pathlength and a phase shift resulting from the photoelectron's interaction with the scattering atom, the scattered component will emerge out of phase with the directly emitted component. When the energy dependence of the constructive and destructive interference arising from this phase difference is analysed for several emission angles using synchrotron radiation, very precise structural information about the emitter and its local environment can be deduced. Such information includes nearest neighbour bond lengths, molecular orientation, relaxation and reconstruction.

2.3 PhD Measurements

A PhD spectrum consists of a succession of energy distribution curves (EDCs) (fig.2.7).

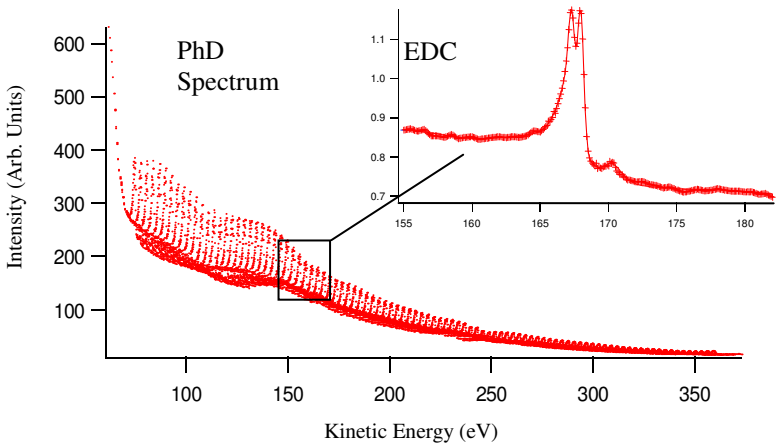

Fig.2.7 A PhD spectrum with an expanded EDC for the C 1s photoelectrons of different species of CO on Pt(111) taken at a temperature of 130K.

An EDC is a measurement of photoelectron intensity as a function of energy for a specific photon energy. Each EDC is measured around the core level peak with a suitable window allowing for the necessary background levels to be included. When the background is extrapolated to remove low amplitude noise, individual peaks in each EDC can be fitted and integrated to give the peak intensity. This is done using a Gaussian function modified with a step to compensate for the differences in background height either side of the peak.

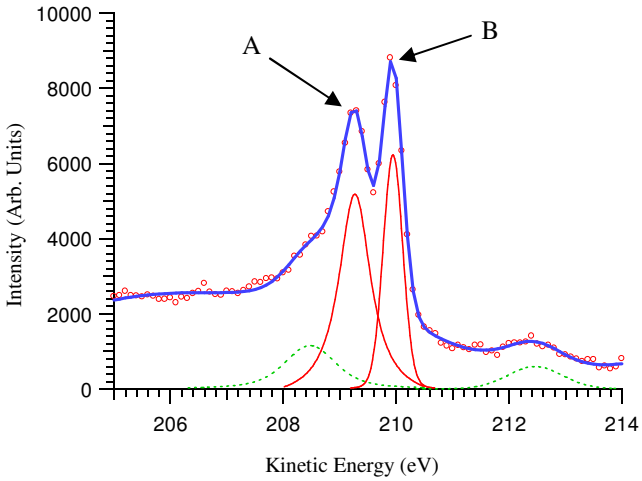

Fig. 2.8 High resolution XPS spectrum for C 1s measured with a photon energy of 500eV. The peaks labelled A and B correspond to the C 1s peaks for the atop and bridge species respectively. The features of this spectrum will be discussed in section 4.3.1.

It is often the case, as mentioned earlier, that the chemical shift is not sufficiently large to prevent some overlap in the peaks for different species of the same element. This is the case for the example represented in fig.2.8, however, when enough of the peak profile can be resolved, it is possible to obtain an acceptable integration of the peaks. Once this is done the integrals of individual peaks for each EDC can be separated out and their intensities ($I(E_{kin})$) can be plotted against the kinetic energy for the entire PhD spectrum (fig.2.9).

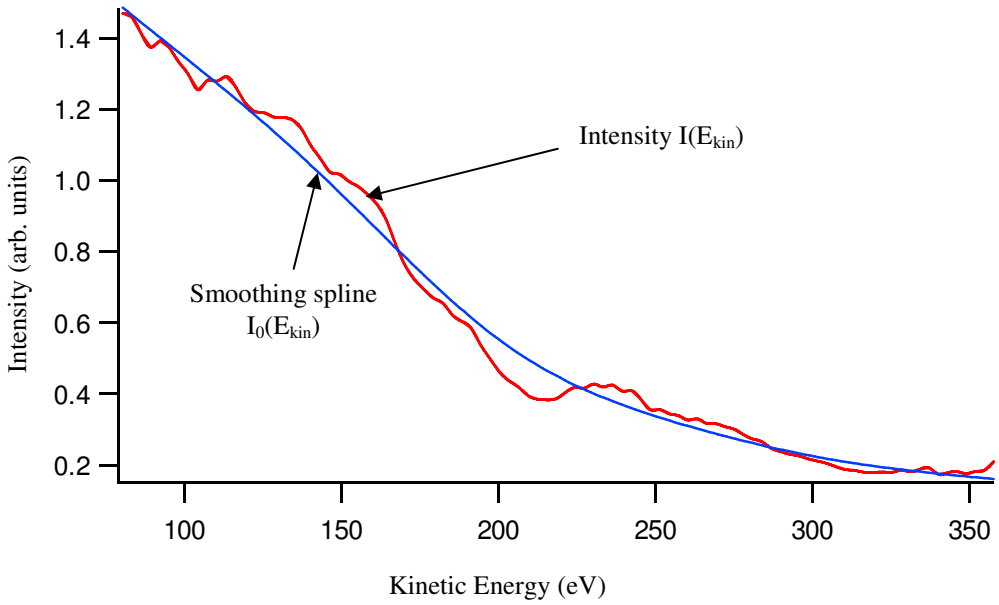

Fig.2.9 Example of an intensity versus kinetic energy curve for a C 1s PhD scan for an atop CO species in the Pt(111)c(5x√3)rect.-CO system.

There are some intrinsic influences on the experiment which must be accounted for. As previously mentioned, PhD requires the use of synchrotron radiation. The electron current produced by the synchrotron has a half life of a few hours which significantly reduces the X-ray flux density over the duration of the PhD scan which takes about two hours. In addition to this, the reflective properties of the monochromator must be accounted for. The monochromator is effectively a plane mirror with a diffraction grating (either 400 or 1200 lines per mm). The mirror exhibits different degrees of reflectivity depending on the energy of the incident radiation thereby directly affecting the flux density of the beam. A third influencing factor is the variation of the photoionisation cross section as a function of photon energy.

Compensation for these influences can be made by using an appropriate software package such as Igor (also used to integrate the peaks) to fit a smoothing spline function to the data (fig.2.9). The data is then normalised to the spline function by the equation:

$$\chi = \frac{I(E_{kin}) - I_0(E_{kin})}{I_0(E_{kin})} \qquad 2.5$$

Where $I(E_{kin})$ is the data intensity at the kinetic energy E_{kin}, and $I_0(E_{kin})$ is the intensity of the spline function at the kinetic energy E_{kin}. The result is a modulation function (fig. 2.10), also known as a chi (χ) curve.

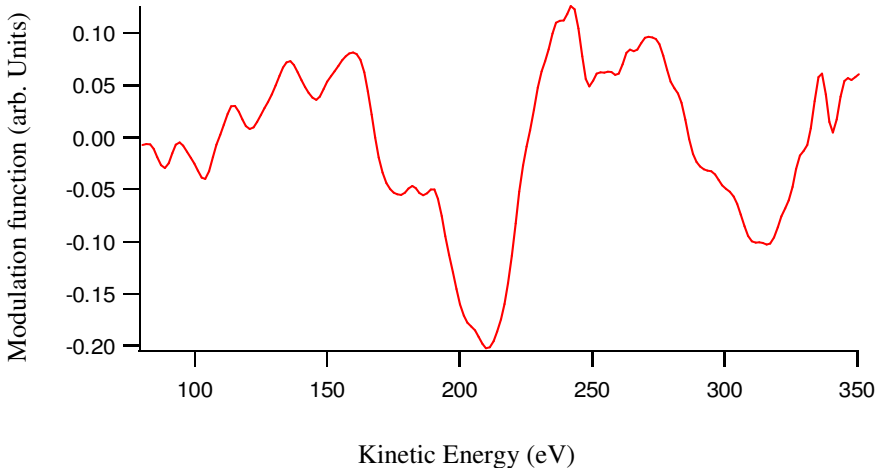

Fig. 2.10 Modulation function χ derived from the intensity versus kinetic energy curve depicted in fig .2.9.

2.4 Analysis of PhD Data

A quantitative structural analysis is achieved through trial-and-error modelling, simulating the experimental data with multiple scattering calculations for various trial structures. These calculations are performed with codes developed by Fritzsche [15-17], which are based on the expansion of the final state wave-function into a sum over all scattering pathways which the electron can take from the emitter atom to the detector outside the sample. A magnetic quantum number expansion of the free electron propagator is used to calculate the scattering contribution of an individual scattering path. Double and higher order scattering events are treated by means of the Reduced Angular Momentum Expansion (RAME) [18]. The finite energy resolution and angular acceptance of the electron energy analyser are accounted for analytically. Anisotropic

vibrations for the emitter atom and isotropic vibrations for the scattering atoms are also taken into account.

First, the crystal structure of the substrate is defined by giving the position of one atom and defining 3 translation vectors. Thus a 3D network is generated, creating a hemispherical cluster with a radius of 30 Å. The adsorbate molecules are then defined with respect to the substrate in positions roughly deduced from a direct analysis of the experimental modulation functions (see chapter 4). The periodicity of the adsorbate overlayer is often known from LEED experiments and can be reproduced in the simulation program using 2D translation vectors. Once the general cluster has been defined, the theoretical model is compared with the experimental one using an objective reliability factor or R-factor. Equation 2.6 produces an R-factor comparing the experimental modulation function with the simulated modulation function for a single spectrum.

$$R = \frac{\sum_{i=1}^{m}\left(\chi_{exp}^{Kj}(E_i) - \chi_{th}^{Kj}(E_i)\right)^2}{\sum_{i=1}^{m}\left(\chi_{exp}^{Kj}(E_i)^2 + \chi_{th}^{Kj}(E_i)^2\right)} \qquad 2.6$$

Where $\chi_{exp}^{Kj}(E_i)$ is the intensity of the experimental modulation function at the point i, and m is the number of points in the modulation function.

The global R-factor, R_{global}, is of the same form but includes all of the spectra.

$$R_{global} = \frac{\sum_{j=1}^{n}\sum_{i=1}^{m}\left(\chi_{exp}^{Kj}(E_i) - \chi_{th}^{Kj}(E_i)\right)^2}{\sum_{j=1}^{n}\sum_{i=1}^{m}\left(\chi_{exp}^{Kj}(E_i)^2 + \chi_{th}^{K_j}(E_i)^2\right)} \qquad 2.7$$

Where K_j is the direction of the emitted electrons for a given spectrum, j, and n is the total number of spectra. The global R-factor provides a weighted average of the individual R-factors. That is, spectra taken in directions which are experimentally more favourable, resulting in

stronger modulations, have more of an influence over the global R-factor. An R-factor of 0 represents perfect correlation between the experimental and theoretical modulation function, a value of 1 implies no correlation and a value of 2 means there is anti-correlation. Usually the starting model shows little or no correlation, and so the parameters must be optimised. This is done in two ways. Firstly, a series of line scans are carried out. These involve scanning a variable (sometimes 2 or 3 when the variables are coupled) over a selected range with an appropriate step size until a minimum R-factor is reached. This is repeated for all the defining parameters which include, bond lengths, bond angles, interlayer separation, surface relaxation and reconstruction parameters, and vibrational amplitudes. Secondly, the fitting procedure is carried out. This is directed by the program itself, which searches for the minimum R-factor by improving the value of selected parameters. The fitting procedure is only carried out after the line scans to prevent the program optimising about a false local minimum. The evolution of the R-factor could be represented as a succession of peaks and troughs. A local minimum R-factor would be the bottom of a trough but not the deepest trough.

PhD, like any surface science technique, is more sensitive to certain parameters than others. An indication of the precision to which these parameters can be determined, can be obtained via a calculation of the variance [19] in the minimum R-factor (R_{min}).

$$\mathrm{var}(R_{min}) = R_{min}\sqrt{\frac{2}{N}} \qquad 2.8$$

Where N is the number of independent pieces of structural information contained in the data and is given by:

$$N = n \times \frac{\delta E}{4\sqrt{V_{Oi}^2 + E_b^2}} \qquad 2.9$$

δE is the energy range of the spectra, n is the number of spectra used, V_{Oi} is the imaginary part of the inner potential, taken to be 5 eV, and E_b is the energy broadening factor, also taken to be 5 eV.

The variance can be applied to individual parameters to give a range of acceptable errors for those parameters. This is done by plotting the R-factors against the corresponding parameter

values and taking the interval containing the parameter values with an R-factor below R_{min}+var(R_{min}) (see fig. 2.11).

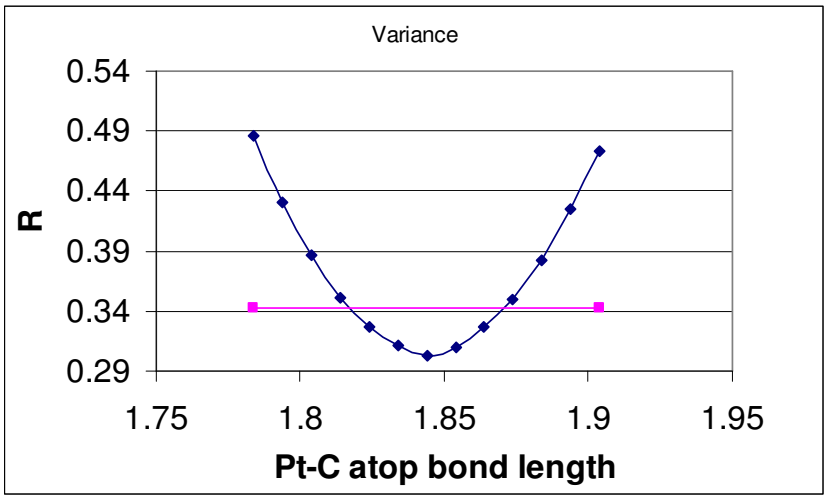

Fig. 2.11 Variance graph for Pt-C bondlength. In this case R_{min}+var(R_{min}) was calculated to be 0.3445. The R_{min}+var(R_{min}) line intersects the Pt-C curve at 1.816 Å and 1.872 Å any value between these points is within the error limits for this parameter.

2.5 LEED

LEED (low energy electron diffraction) is a well established technique which can involve, like PhD, the use of complex simulations and even more extensive data sets. However, in its simplest form it can give a visible diffraction pattern of the corresponding periodicity of the reciprocal mesh of the surface. This can be viewed on a fluorescent screen directly without the need of any data analysis. As well as providing an elegant method of determining the periodicity of the surface, the diffraction pattern can be used to determine the azimuthal orientation of the crystal.

LEED experiments are performed by directing a beam of electrons of a well-defined low energy (typically in the range 20 - 200 eV) at normal incidence to the sample. The sample itself must be a single crystal with a well-ordered surface structure in order to generate a back-scattered electron diffraction pattern. A typical experimental set-up is schematized in fig. 2.12.

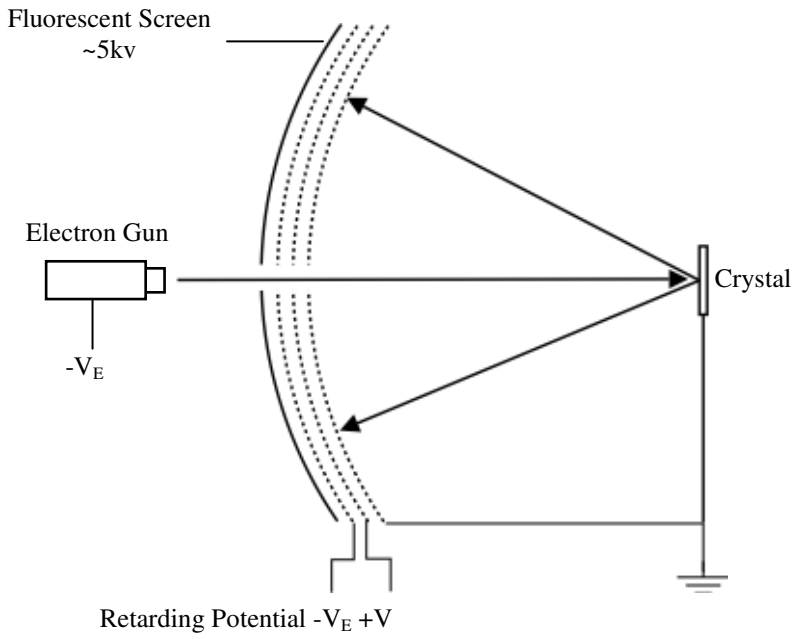

Fig.2.12 Typical setup of electron gun, filtering grids, and fluorescent screen used in LEED experiments,

The electrons are scattered both elastically and inelastically. The latter emerge from the sample with a reduced energy and are removed by the energy-filtering grids. Consequently, only the elastically-scattered electrons contribute to the diffraction pattern.

The positions of the diffraction spots are determined by the space lattice (i.e. by the size and shape of the unit cell) and are independent of the penetration depth of the electrons. The intensities are determined by the diffraction function (i.e. by the exact atomic coordinates within the unit cell) and are a function of the electron penetration depth. The basis vectors a_1 and a_2 describe the unit cell in real space and define the smallest parallelogram from which the surface can be reconstructed by simple translation. A reciprocal space representation of the real space lattice is defined by the basis vectors a_1^* and a_2^*. Introducing γ and γ^* as the angles between (a_1 and a_2) and (a_1^* and a_2^*) respectively (see fig.2.13), the relationship between the real space and reciprocal space vectors can be expressed as follows.

$$a_1^* = \frac{1}{a_1 \sin\gamma} \qquad 2.10$$

$$a_2^* = \frac{1}{a_2 \sin\gamma} \qquad 2.11$$

$$\sin\gamma = \sin\gamma^* = \sin(180-\gamma) \qquad 2.12$$

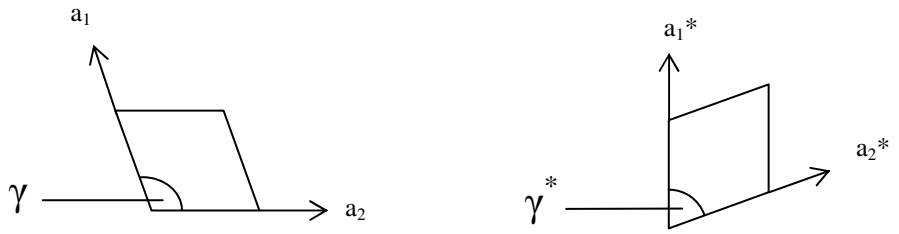

Fig.2.13. A diagram showing the relationship between γ and γ*.

The inverse relationship expressed here means that a short vector in real space corresponds to a long vector in reciprocal space. The diffraction pattern corresponds to reciprocal space and can easily be transposed using equations 2.10 and 2.11, to describe the real space lattice.

2.5.1 Overlayer Notation

There are two conventions for naming overlayer structures. The first of these, Wood's notation, relates the overlayer mesh to the substrate mesh and can be describe by the form:

$$\mathrm{M}(hkl)(\mathrm{c\ or\ p})\left(\frac{|a_o|}{|a_s|}\times\frac{|b_o|}{|b_s|}\right)-\mathrm{R}\alpha^{\circ}-\mathrm{A}$$

Where M = the chemical symbol for the substrate; (*hkl*) = the miller indices of the surface plane; c or p = centred or primitive unit cell (if primitive, the p is usually dropped); $|a_s|$ and $|b_s|$ = the magnitude of the substrate vectors; $|a_o|$ and $|b_o|$ = the magnitude of the overlayer vectors; α = angle between the overlayer and substrate meshes; and A = the chemical symbol for the overlayer species.

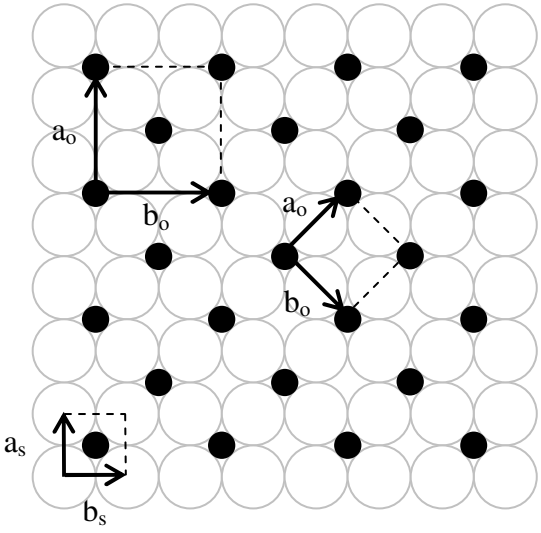

Fig.2.14 Example of a Cu (100) - c(2 x 2) – CO or Cu (100) - ($\sqrt{2}$ x $\sqrt{2}$)R45^o - CO as described by Wood's notation. Note that a_1 and b_1 can be measured in terms of either a centred or primitive unit cell in this example.

The second convention for naming overlayer structures is to use the matrix notation. Taking the example depicted in fig.2.14, the primitive mesh vectors of the substrate (a_s and b_s) can be used by way of a linear combination to define the overlayer mesh vectors (a_1 and b_1).

$$a_o = 1a_s + 1b_s \qquad 2.13$$

$$b_o = -1a_s + 1b_s \qquad 2.14$$

$$\begin{pmatrix} a_o \\ b_o \end{pmatrix} = \begin{pmatrix} 1 & 1 \\ -1 & 1 \end{pmatrix} \begin{pmatrix} a_s \\ a_s \end{pmatrix} \qquad 2.15$$

Where the matrix; $\begin{pmatrix} 1 & 1 \\ -1 & 1 \end{pmatrix}$ defines the overlayer mesh in terms of the substrate. The full matrix notation in this example is then, Cu (100) - $\begin{pmatrix} 1 & 1 \\ -1 & 1 \end{pmatrix}$– CO. Wood's will be used throughout this thesis.

3 Hardware

3.1 Synchrotron Radiation Source

As its name suggests, scanned energy photoelectron diffraction requires a source of tuneable X-rays of a suitable intensity. Currently, the most effective way of achieving this is by the use of synchrotron radiation. BESSY II, a third generation synchrotron radiation source located in Berlin was used for this work.

When electrons are accelerated to relativistic velocities (velocities close to the velocity of light, c) and deflected by a magnetic field, electromagnetic radiation is produced tangentially to the arc of deflection. This is synchrotron radiation. Second generation synchrotron radiation sources consisted mainly of a microtron, a synchrotron, a storage ring and tangential beam lines. In the case of BESSY I, the electrons were produced from a hot cathode under ultra high vacuum (UHV) and accelerated towards the anode with a voltage of about 10^5 V. The electrons were further accelerated in a circular trajectory by a high frequency magnetic field in the microtron. Having achieved an energy of 22 MeV, the electrons entered the synchrotron and were further accelerated to an energy of 800 MeV which corresponds to an average velocity of 2.9979240×10^8 ms^{-1} ($c = 2.99792458 \times 10^8$ ms^{-1}). Finally the electrons were transferred to the storage ring where their trajectory was maintained by magnetic fields (see fig.3.1).

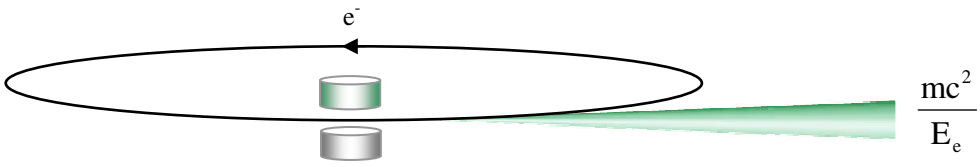

Fig.3.1. A schematic diagram of the bending magnets such as those used in BESSY and BESSYII.

When the orbiting electrons pass through a magnetic field they are deflected in a direction which is perpendicular to the magnetic field. The resulting synchrotron radiation is propagated tangentially to the electron trajectory in a narrow radiation cone with an opening angle ($\Delta\phi$) given by equation 3.1.

$$\Delta\phi \cong \frac{mc^2}{E_e} \qquad 3.1$$

where $$\Delta\phi \cong \gamma^{-1} \qquad 3.2$$

and $$\gamma = \frac{1}{\sqrt{1-\frac{v^2}{c^2}}} \qquad 3.3$$

At BESSY II electrons are accelerated to an energy of 1.6 GeV corresponding to a velocity of 2.9979244×10^8 ms^{-1} which, incidentally, due to a relativistic effect which can be explained in terms of γ, is only 40 ms^{-1} faster than the electrons at BESSY I. Insertion devices, such as wigglers and undulators used in third generation synchrotrons, provide a way of exploiting the intrinsic brightness of the synchrotron-radiation source.

Both wigglers and undulators consist of a periodic array of magnets with alternating polarity. When the relativistic electron passes through these devices, its trajectory is changed at every magnet resulting in an oscillatory motion. Radiation is emitted tangentially to each curved trajectory and is added together in the forward direction as it proceeds along the device. This results in a beam intensity significantly greater than that achieved using bending magnets alone. The magnetic arrays used in wigglers (see fig.3.2) consist of fewer yet stronger magnets than those used in undulators causing deflections through an angle which is large when compared with the radiation cone normally associated with synchrotron radiation. The radiation produced covers a wide energy range exceeding even that produced by the bending magnets; however the brilliance is less due to the enlarged radiation cone.

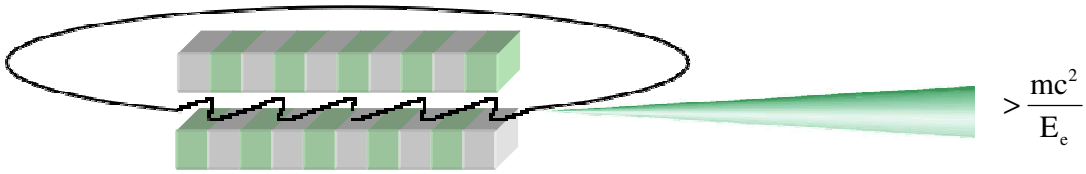

Fig.3.2**.** A schematic diagram of a wiggler array such as that used in BESSY II and other third generation synchrotron radiation sources.

In contrast to wigglers, undulators use weak magnetic fields. As the electron beam passes longitudinally through the array, its trajectory oscillates in the horizontal plane. The relatively weak field of the undulator means the radiation cones emitted at each bend in the trajectory overlap, giving rise to a constructive interference effect. The result is a high intensity beam with one or a few spectrally narrow peaks of quasi-monochromatic radiation which can be tuned by altering the gap between pole tips (fig.3.3).

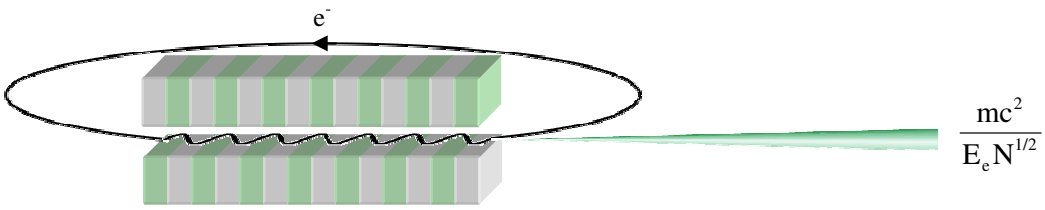

Fig.3.3 A schematic diagram of an undulator array such as that used in BESSYII and other third generation synchrotron radiation sources.

Electrons producing synchrotron radiation lose energy in the process. In addition, particles lose energy due to their interaction with the surrounding vacuum chamber walls. This energy needs to be restored to the electrons so that they can maintain a steady orbit. This is achieved when the electrons pass through the RF (radio frequency) cavity. Electrons entering the cavity in phase with the sinusoidal RF field are accelerated whilst those entering out of phase are subsequently scattered and lost. The inclusion of RF cavities allows the beam to be maintained at a useful intensity for several hours.

3.2 Monochromator

The monochromator facilitates the separation of the broad spectrum of synchrotron radiation into distinct wavelengths, and therefore energies, required for energy scanned experiments. When the electromagnetic radiation enters the beam line, it is collimated by a toroidal mirror and projected on to a plane mirror. The plane mirror is movable and works in tandem with the plane grating ensuring that it receives radiation at a well defined angle of incidence (see fig.3.4).

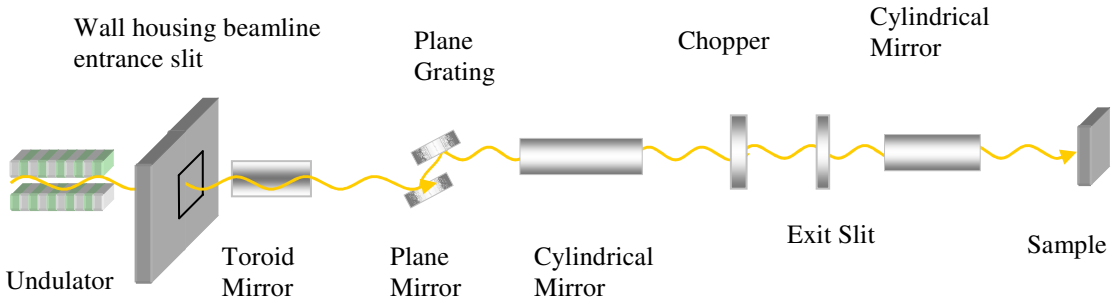

Fig.3.4 Diagram showing the radiation pathway through the UE56/2-PGM 1 beam line at BESSY II.

The plane grating divides the incoming beam into its constituent components (fig.3.5). The plane grating can be positioned so that only the desired 'colour' or energy continues through the beam line.

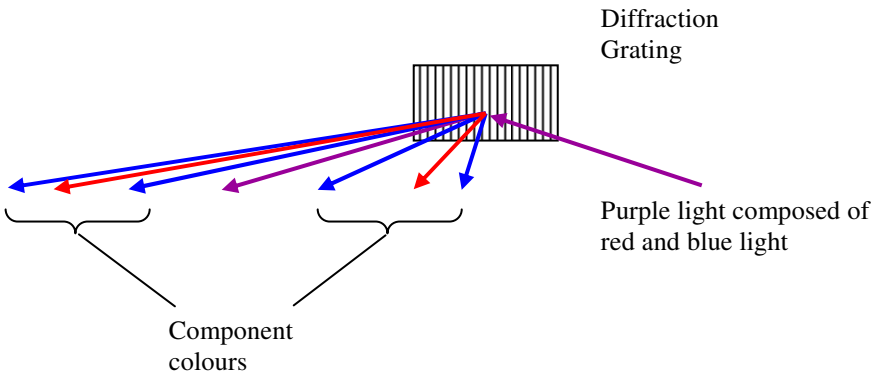

Fig.3.5 An example of how a beam of light can be separated into its constituent components using a diffraction grating. The plane gratings used in this work were 400 or 1200 lines per mm.

The monochromatic light is focused on the exit slit by a cylindrical mirror. A final cylindrical mirror is used after the exit slit, to focus the beam onto the sample creating a spot size of 20-200 μm (vertical) by 900 μm (horizontal). At this point the beam intensity is very high and can unduly influence the system to be analysed by causing desorption or molecular cracking. For this reason a 1.2 m extension tube was placed between the beam line and the chamber to displace the sample from the focal point. The change in spot size is only a few percent because the beam exhibits a high degree of parallelism.

3.3 The Chamber

The UHV (ultra high vacuum) apparatus consists of two chambers vertically arranged and separated by a gate valve (figs. 3.6 and 3.7).

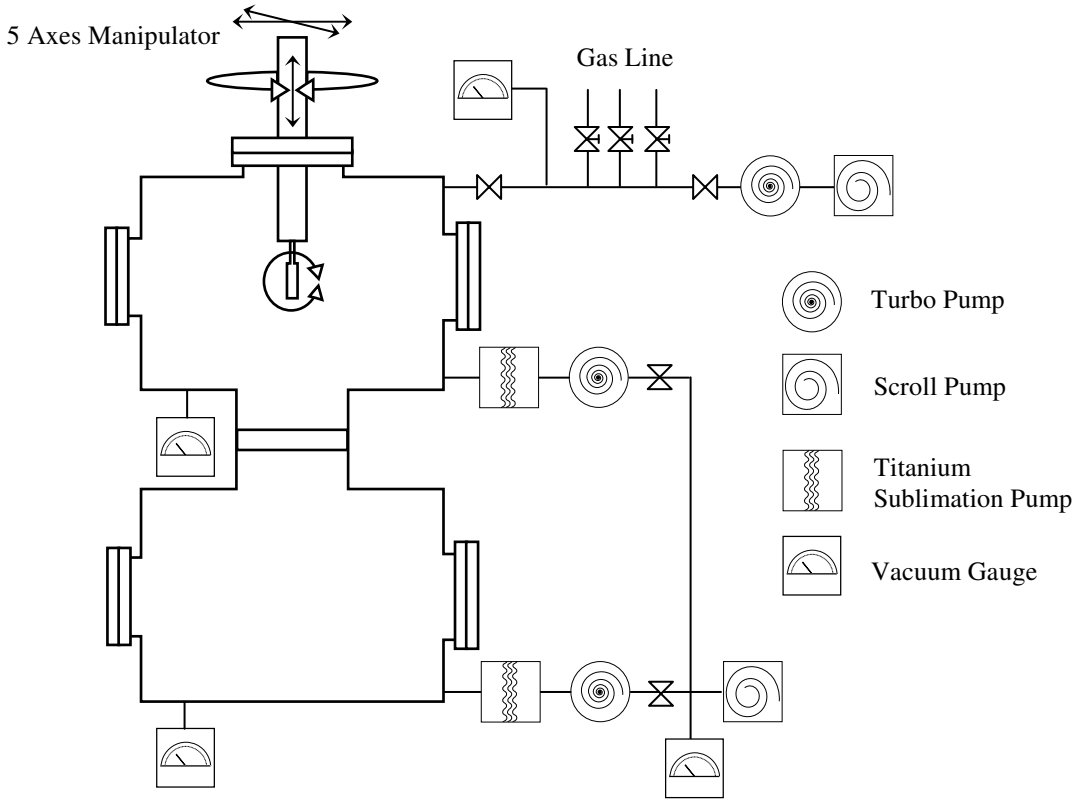

Fig. 3.6 Functional diagram of the UHV apparatus [20].

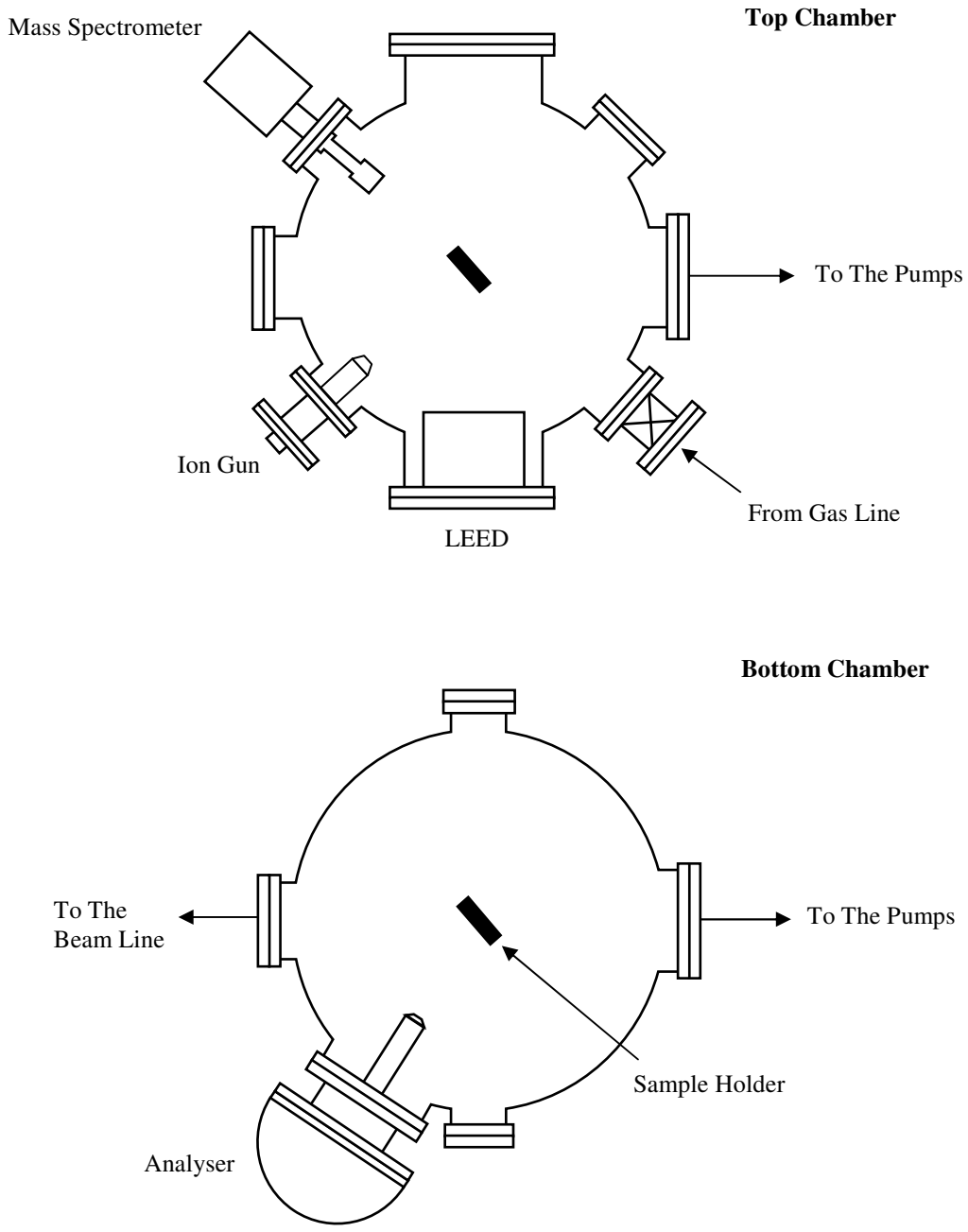

Fig. 3.7 Cross sectional view of top and bottom chambers showing the positions of the mass spectrometer, ion gun, analyser and LEED apparatus.

Both chambers operate with a base pressure of 10^{-10} mbar which is achieved using a combination of scroll, turbo and titanium sublimation pumps. The top chamber is used for preparation and is equipped with an ion gun, dosing facilities, a quadrupole mass spectrometer and a qualitative LEED system. The bottom chamber terminates the beam line and is fitted with an Omicron EA 125 HR electron energy analyser which is described in more detail below. A multidirectional manipulator is used to position the sample. The manipulator is capable of rotating the sample about the polar and azimuthal axis as well as moving in the x, y and z directions. It also provides an earth connection to the sample, replenishing the photo-emitted electrons, and a thermal connection allowing the sample to be cooled to about 140K using liquid nitrogen (LN_2) or about 60K using liquid helium (LHe). The sample can also be heated using a tungsten filament positioned directly behind the sample which is set to a high voltage of around -500 V. Passing a current of about 5 A through the filament produces an emission current of around 30 mA.

3.4 Electron Energy Analyser

The Omicron EA 125 HR is a concentric hemispherical analyser (fig.3.8) and is comprised of an electrostatic lens, two negatively-charged concentric hemispheres, and a channeltron detection system.

The lens is used to collect, retard and focus the electrons. The electrons enter the hemispherical dispersing unit through the entrance slit. The electrons are exposed to an electric field resulting from the negatively charged hemispheres (where $U_1 > U_2$) and are consequently deflected. The extent of this deflection depends on the strength of the electric field and the energy of the electrons. Only electrons in a narrow energy region ($E \pm \delta E$) succeed in reaching the exit slit. The width of this energy region ($2\delta E$) is known as the pass energy. Electrons with an energy less than $E - \delta E$ will be forced into the inner hemisphere by the greater potential of the outer hemisphere. While those with an energy greater than $E + \delta E$ are able to overcome the potential of the outer hemisphere and are consequently terminated.

The analyser setup allows two basic modes of operation, namely the *constant retarding ratio* mode, and the *constant transmission* mode. In the former the electrons are retarded by a fixed energy before entering the hemispheres and the energy range is selected by varying the

potentials U_1 and U_2. In the latter mode, the mode used for this work, the potentials U_1 and U_2 are kept constant and the energy range is selected by varying the degree of retardation.

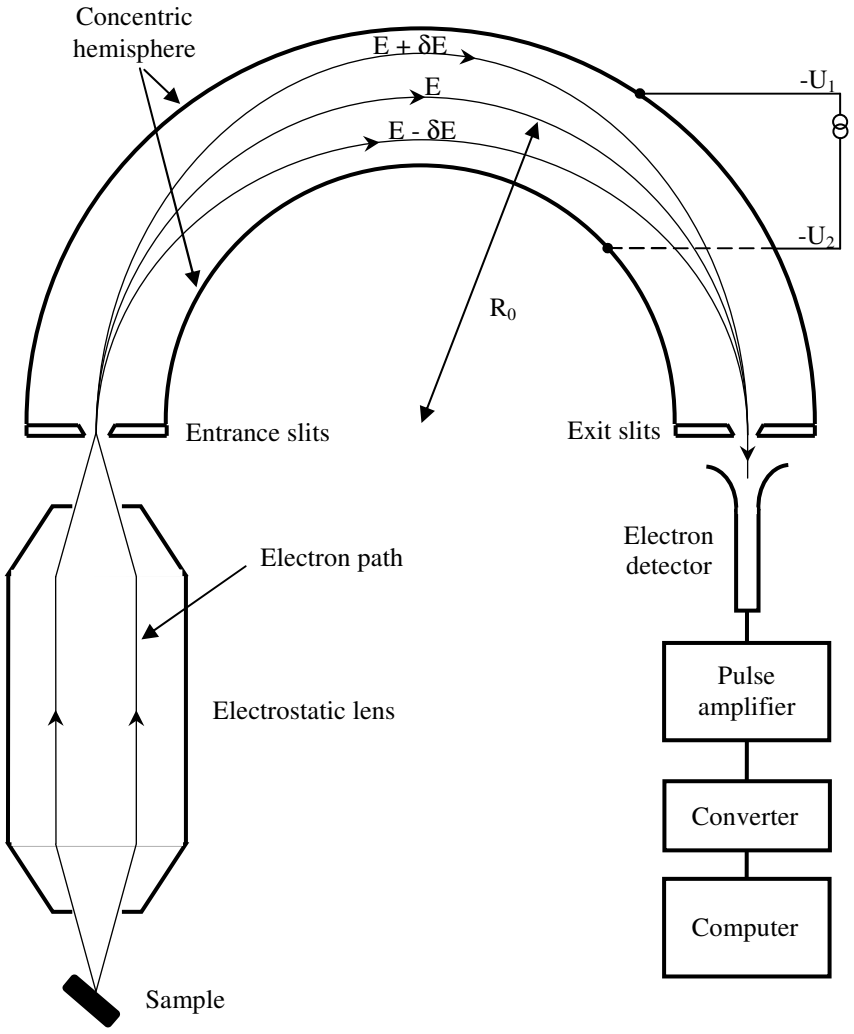

Fig.3.8 Schematic representation of the Omicron EA 125 HR electron energy analyser [21].

The electrons leaving through the exit slit are detected by an array of 7 channeltrons. A typical example of a channeltron is depicted in fig. 3.9. It consists of a specially formulated lead silicate glass, shaped like a cornucopia, and exhibits the properties of electrical conductivity and secondary electron emission. The input end (the cup) is at ground or some positive potential while the output end (the tail) is at high positive voltage. An electron striking the

input face of the cup produces 2-3 secondary electrons which in turn do the same. These electrons are accelerated down the channel by the positive bias causing a cascade generating a pulse of 10^7 to 10^8 electrons.

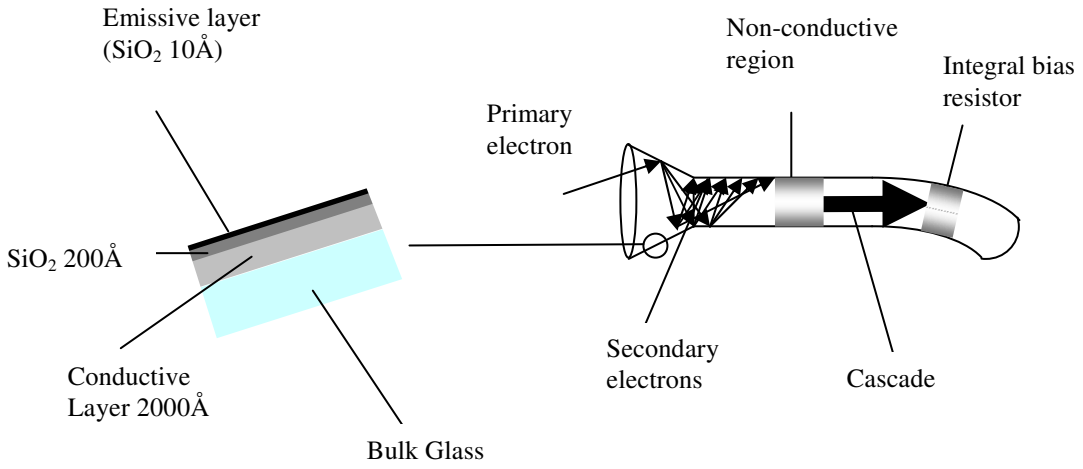

Fig.3.9 The basic operation of a typical channeltron.

The use of more than one channeltron enables parallel detection, reducing the signal to noise ratio.

The analyser is mounted at 60^o with respect to the incident radiation and lies in the plane of the radiation polarization vector. This is done to maximise the signal, detecting both directly emitted and scattered photoelectrons. The consequences of positioning the analyser out of the polarization vector will be discussed in chapter 6.

4 Surface Structure of Pt(111)c(5x√3)rect.3CO at 0.6 ML Coverage

4.1 Introduction

There have been numerous studies pertaining to the structural determination of CO adsorbed on Pt(111). This system is accredited with such importance because of its application as a catalyst promoting the oxidation of CO to CO_2 in car exhaust systems. Moreover, due to the simplicity of the CO molecule, it is often used as a probe molecule in surface science. A better understanding of the catalytic properties of the CO/Pt(111) system depends on quantitative analysis of the system's adsorption behaviour. Relevant aspects of this behaviour include parameters such as adsorption sites, periodicity, bond lengths, bond axis and substrate reconstruction and relaxation. These parameters have been analysed in this project for the Pt(111)c(5x√3)rect.-3CO configuration resulting from a coverage of 0.6 ML.

4.1.1 Adsorption Sites and Periodicity

When analysing the structure of adsorbate/substrate systems, the first structural parameter to be considered is where the adsorbate will locate itself and, subsequently, with what periodicity. In the case of Pt(111), adsorption can occur at four possible adsorption sites, namely atop, bridge, and two inequivalent hollow sites (fig.4.1). The inequivalence of the hollow sites owes to the fact that Pt(111) exhibits an ABC periodicity in its layers meaning that one hollow site is situated directly above a Pt atom in the second layer while the other is situated directly above a Pt atom in the third layer, these are known as hcp and fcc hollow sites, respectively.

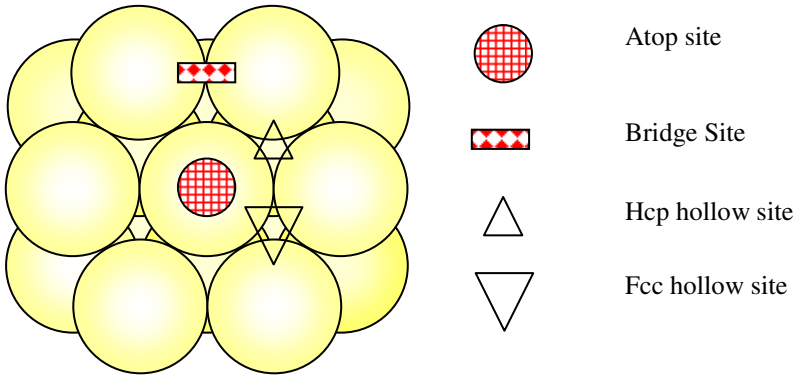

Fig.4.1. Types of adsorption sites on a Pt(111) surface.

Blackman et al. [22], using diffuse LEED, studied a disordered $^1/_3$ monolayer at 160 K, and concluded that 88% ± 5% of the molecules occupy atop sites while 12% ± 5% occupy bridge sites. They also indicated that a c(4x2)-2CO arrangement is formed at a coverage range of 0.35 - 0.5 ML at just below room temperature.

According to the electron energy loss spectroscopy (EELS) studies of Steininger et al. [23], CO adsorbs preferentially on Pt(111) at atop sites forming a $(\sqrt{3}\times\sqrt{3})$-R30^o structure (fig.4.2) at 170 K which then evolves to a c(4x2) structure at higher coverage, corresponding to half a monolayer consisting of adsorbates occupying both atop and bridge sites (fig.4.3).

In their dynamical LEED intensity analysis of the CO/Pt(111) system at 150 K with a coverage of 0.5 ML, Ogletree, Van Hove, and Somorjai [24] also found that CO adsorbed preferentially at atop and bridge sites.

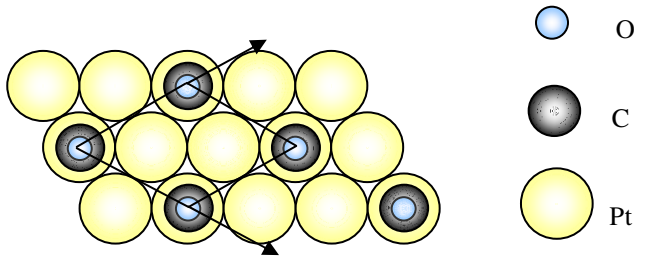

Fig.4.2. The Pt(111) $(\sqrt{3}\times\sqrt{3})$-R30^o arrangement. The same colour scheme will be used throughout,

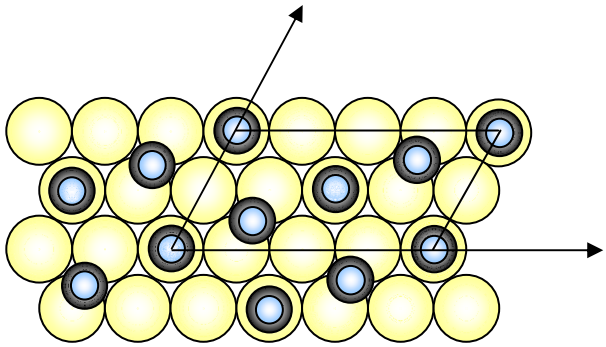

Fig.4.3. The Pt(111) c(4x2)-2CO arrangement.

These assignments were later confirmed by a dynamical LEED study [22] and further substantiated by C.A Lucas et al. [25] using X-ray diffraction. M.Ø. Pedersen et al. [26] using scanning tunnelling microscopy (STM), also showed that two sites are occupied by CO at low

coverage (0.5 ML), which, when compared with simulated STM images were accepted to be atop and bridge sites in a c(4x2)-2CO configuration which is observed at both 150 K and 300 K.

Petrova et al. [27] proposed a c(4x2)-2CO structure using the alternative notation (2x√3)rect.-2CO assigning a 1:1 ratio of atop and bridge species at 170 K. However, in contrast to the findings of the preceding studies, they argued that the LEED pattern they obtained (Fig.4.4) was indicative of a configuration in which the bridge species occupy bridge sites which are not equidistant from the neighbouring occupied atop sites (see fig.4.5).

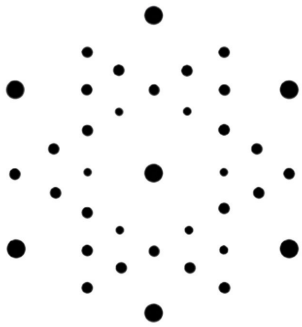

Fig.4.4 LEED pattern corresponding to 0.5 ML [27]

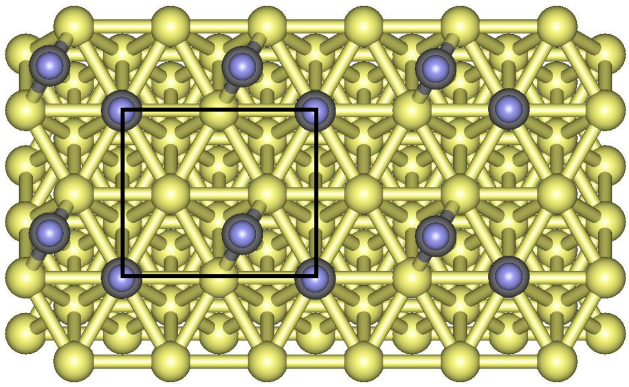

Fig.4.5. The Pt(111) c(4x2)-2CO arrangement Petrova et al. [27].

Petrova et al. [27] also investigated higher coverages and proposed a c(√3 x 5)rect.-3CO structure, comprised of atop and bridge species in a 1:2 ratio (see fig. 4.6), at a coverage of 0.6 ML. This corresponds to the LEED pattern shown in fig 4.7.

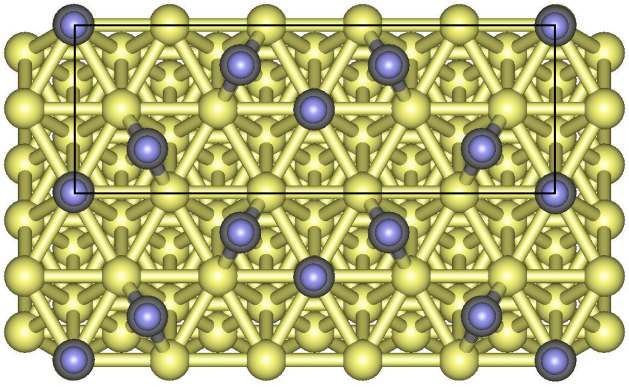

Fig. 4.6. The c(√3 x 5)rect.3CO arrangement as proposed by Petrova et al [27] (based on a diagram presented in their paper).

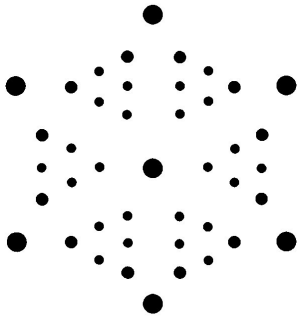

Fig. 4.7. LEED pattern resulting from CO adsorbed on Pt(111) at a coverage of 0.6 ML [27].

This assignment however, is contradictory to the findings of Persson et al. [28] who proposed that as θ increases beyond 0.5 ML, the relative bridge coverage decreases so that at the point when θ is equal to 1 ML, no bridge species remain. Their study undertaken at 50 K involved the comparison of Monte Carlo simulations with LEED and infrared spectra, and resulted in the proposal of a c(5x√3)rect.-3CO overlayer in a 2:1 atop/bridge configuration (Fig.4.8). Their model is described as consisting of vertical strips of the c(4x2) structure forming a phase/antiphase sequence. The strips are separated by fault lines or domain walls consisting of higher density terminal CO molecules. Persson also points out that these CO molecules are displaced from the high-symmetry atop sites by ~0.4 Å due to the unbalanced repulsive intermolecular interactions.

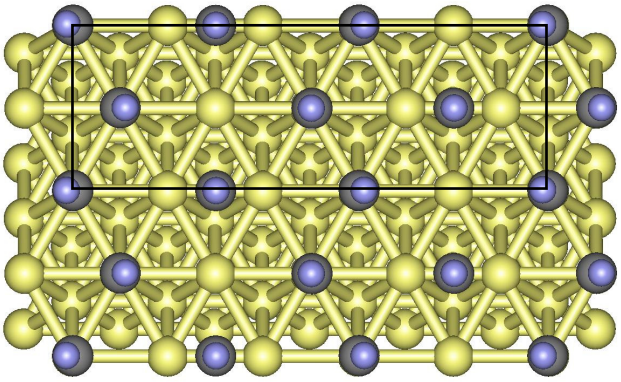

c(√3 x 5) rect.

Fig. 4.8. Schematic diagram of the c(√3 x 5)rect. phase for CO adsorption on Pt(111) at a nominal coverage of 0.6 proposed by Persson et al. [28].

Avery [29], in his EELS study of CO on Pt(111) at 140 K reports a decrease in bridge species beyond a coverage of 0.5 ML which is in agreement with the findings of Persson et al. [28] Avery also proposes a c(5x√3)rect.-3CO (see fig 4.9) overlayer which however, is neither in agreement with the findings of Persson nor Petrova. Avery describes this configuration as consisting of strips of half-monolayer c(4x2) structures which are antiphase with adjacent strips across coherently spaced boundaries or packing faults.

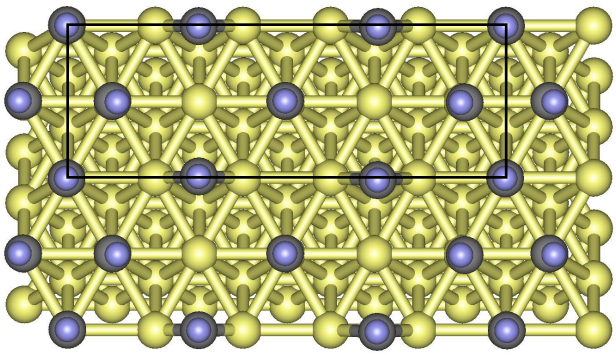

c(√3 x 5) rect.

Fig. 4.9. Image based on the c(5x√3) rect-3CO proposed by Avery [29].

The c(5x√3)rect.-3CO proposed by Persson et al. [28] is supported by the STM observations of Song et al. [30]. While their analysis does not deal with a complete 0.6ML surface, they do observe domains of 0.5 ML and 0.6 ML coverage, corresponding to the c(4x2)-2CO and c(5x√3)rect.-3CO configurations.

4.1.2 Bond Lengths

In addition to the determination of the preferential adsorption sites and the periodicity, a determination of the inter-atomic bond lengths is necessary as this is a direct result of the chemical behaviour of the system and therefore bears some relevance to the catalytic processes involved.

Numerous studies have been undertaken with the aim of properly determining the inter-atomic bond lengths of the c(4x2)-2CO system. Using the fhi96md plane-wave DFT code, Alavi et al. [31] calculated a Pt-C bond length of 1.86 Å for atop sites and 1.94 Å for bridge sites for the c(4x2)-2CO system (Fig.4.2). The respective C-O bond lengths were computed to be 1.13 Å and 1.16 Å. A more recent DFT study by M. Lynch and P. Hu [32], reports a Pt-C_{atop} bond length of 1.85 Å, a Pt-C_{bridge} bond length of 2.01 Å and respective C-O bond lengths of 1.15 Å and 1.18 Å. These values are in good agreement with the results of a LEED intensity study performed by Ogletree et al. [24]. Ogletree found the respective Pt-C_{atop} and Pt-C_{bridge} bond lengths to be 1.85 ± 0.05 Å and 2.01 ± 0.07 Å and the C-O bond lengths to be 1.15 ± 0.05 Å for both species. These values are presented again later in table 4.3.

Blackman et al. [22], in their diffuse LEED study, report Pt-C interlayer spacings of $d\perp_{top}$ = 1.85 Å and $d\perp_{bridge}$ = 1.55 Å which correspond to bond lengths of 1.85 Å and 2.08 Å, respectively. The C-O bond lengths were taken to be 1.15 Å and perpendicular to the surface as reported by Ogletree.

M.Ø. Pedersen et al. [26], in their scanning tunnelling microscopy study, report Pt-C_{atop} and Pt-C_{bridge} bond lengths of 1.80 Å and 2.05 Å respectively. The corresponding C-O bond lengths were both found to be 1.15 Å.

Few studies pertaining to the 0.6 ML system have been undertaken, and of those, none report any information regarding bond lengths. However, the relevance of the information detailed above arises from the inference based on the findings of both Petrova and Persson, that only atop and bridge sites are occupied even at the higher coverage. Therefore, if the bond orders are similar, the bond lengths should also be reasonably similar. This idea is supported by D.P.Woodruff et al. [33] in their DFT and PhD study on the relationship between bond lengths and bond strengths. They show that CO weakly chemisorbed in the c(2x2)-CO/H phase at the

atop site has a Ni-CO bond length marginally longer (0.06 Å) than that for the same atop site in the strongly chemisorbed c(2x2)-CO phase despite a change in chemisorption bond strength of more than a factor of 2.

4.1.3 Adsorbate Tilt

In their ESDIAD study of the high coverage CO/Pt(111) system, Kiskinova et al. [34] presents evidence of tilting in the terminal-CO species of 6 ± 1º in the [112] equivalent directions. This, it is argued, is associated with the close packing of the terminal-CO in the fault line regions. The model upon which this argument is based is that proposed by Avery et al. [29] (fig 4.9). While this model is in dispute, the alternative model proposed by Persson et al. [26] (fig 4.8) bears similar characteristics in that there are regions in which the terminal-CO species occupy adjacent Pt sites. Persson suggests that the resulting repulsive intermolecular interactions causes a shifting of the CO molecules off the high symmetry atop positions by ~0.4 Å, which assuming the C-O bond axis points to the centre of the Pt_{atop} atom, corresponds to a tilt of 10º.

4.1.4 Relaxation

While the aforementioned structural parameters can be interpreted as the effects of the substrate on the CO molecules, the effects of CO on substrate relaxation and reconstruction must also be considered. The surface of a substrate differs considerably from the bulk due to the fact that the surface atoms do not have their full coordination complement. The atoms, therefore, find themselves in a higher energy situation. In response to this, the surface undergoes relaxation; that is, the top layers undergo subtle changes in their bonding geometries to accommodate an overall energy reduction. Further relaxation occurs during adsorption.

The adsorbate-induced distortion of the substrate is important in the study of catalytic mechanisms due to the effect it has on adsorbate-adsorbate interactions. According to R.Brako et al, this distortion manifests itself as an induced surface stress, which then leads to a repulsive force between adsorbates [35]. While their study is informative and provides a good qualitative description of surface stress and relaxation, they were unable to provide a quantitative description. I. Zasada [36] reports in his spin-dependent diffuse LEED (SPLEED) study of CO on Pt(111), that the Pt(111) surface exhibits vertical relaxation only. Van Hove [37] presents a description of the Pt(111)c(4x2)-2CO system and includes an overall relaxation value of 0.006

Å and a vertical contraction of 0.06 Å for the first layer Pt atoms not involved in the CO adsorption. Again, no quantitative analysis of the substrate relaxation has been carried out for the c(5x√3)rect.-3CO system.

4.2 Aim

Previous attempts to analyse CO adsorption on Pt(111) using PhD proved unsuccessful due to technical limitations at the time, such as the inadequacy of the beam intensity in second generation synchrotrons, and the relatively poor resolution of the monochromators employed. Third generation synchrotrons can achieve a brilliance one million times that of their predecessors meaning significantly more data points can be measured per EDC and higher resolution monochromators can be used. Such advances have facilitated the undertaking of new measurements. The aim in this portion of the project is to utilise these technological enhancements and exploit the capabilities of PhD in the structural determination of 0.6 ML CO adsorption on Pt(111).

4.3 Experimental

4.3.1 Sample Preparation

The Pt(111) crystal was cut by spark erosion from a single crystal bar. The surface was treated mechanically with abrasives and diamond paste and subsequently by electrolytic polishing. The crystallographic orientation was checked by Laue X-ray diffraction. The Pt(111) surface oxidises readily in air and must therefore be cleaned in situ. This is done when the pressure in the chamber is low enough ($< 5 \times 10^{-10}$ mbar) to minimise recontamination. The crystal was sputtered with Ar ions at an angle of 45^{o} - 60^{o} off normal, and annealed at 640 ^{o}C to reconstruct or 'heal' the surface. The integrity of the surface was checked by LEED and its cleanliness by XPS measured at a photon energy of 700 eV over a kinetic energy range of 150 eV to 700 eV. The pass energy was set to 50 eV and the magnification to medium.

The c(5x√3) rect.3CO surface was prepared by dosing 6 L (8×10^{-8} mbar for 100 s) of CO at 158 K. XPS was performed about the C 1s peak over a kinetic energy range of 204 eV – 213 eV with a photon energy of 500 eV. The magnification was set to medium as before but the pass

energy was set to 5 eV resulting in the measurement of very high resolution spectra which reveal a 2:1 A/B ratio, a shoulder labelled C on the on the lower kinetic energy side of A, likely to be the result of the vibrational modes of the atop CO and a final peak labelled D which is atomic C (fig.4.9).

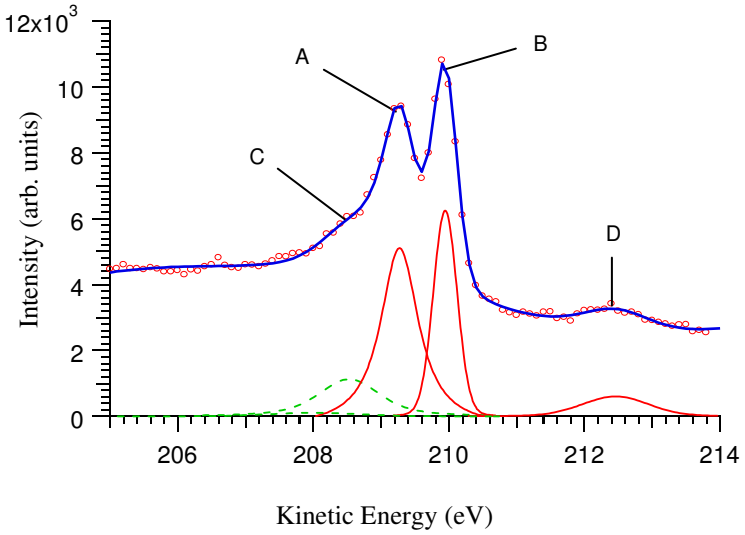

Fig.4.9 High resolution XPS spectrum for C 1s measured with a photon energy of 500eV. The peaks were fitted with Voigt functions and reveal an A/B ratio of 2:1. Peak C due to vibrational modes of the atop species and D is atomic C due CO dissociation.

LEED was then used to establish that a c(5x√3) overlayer had been achieved, producing the diffraction pattern shown in fig.4.9.

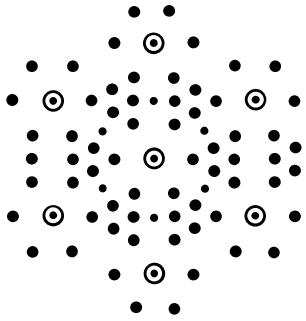

Fig.4.10. Image representing LEED pattern obtained during the experiment. The spot intensity is represented here as spot size; the larger spots corresponding to higher intensity. The ringed spots represent the diffraction from the substrate atoms.

With the exception of some very faint spots between the radial triangles (probably resulting from some remaining c(4x2)-2CO domains), this pattern is consistent with that produced by the

LEEDpat2 program [38] for a hexagonal p3m1 2D lattice with a c(√3x5)R60º overlayer and also for the (√7x√3)R30º overlayer (see Table 4.1). The p3m1 notation describes the FCC surface. The p stands for primitive meaning that the surface can be produced by the translation of a primitive cell. The number 3 refers to the highest order of rotation in other words there are 3 rotations of the primitive cell, each being one third of a revolution which is characteristic of an abc surface. The m stands for mirror meaning there is a reflection perpendicular to the x-axis and 1 means there is no symmetry axis perpendicular to the x-axis [39]. The c(√3x5)R60º unit cell can be defined in terms of a primitive unit cell as (√7x√3)R330º which is equivalent to (√7x√3)R30º about a 60º rotation.

Overlayer Designation	**Overlayer Diagram**	**LEED Pattern [38]**	**LEED Pattern including domains**
c(√3x5)R60º **(√7x√3)R330º**	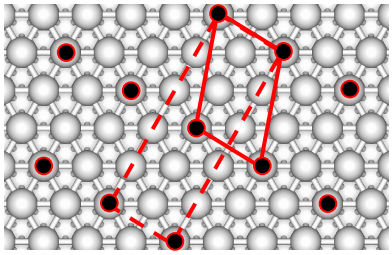	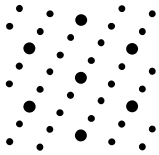	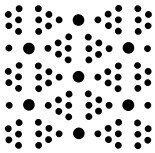
(√7x√3)R30º **c(5x√3)R30º**	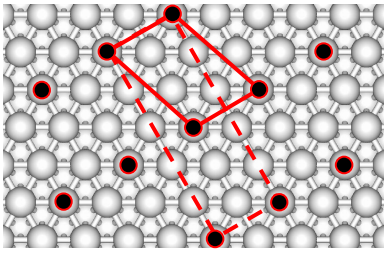	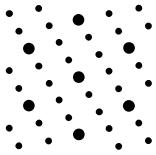	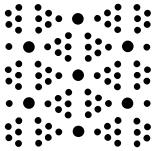
c(5x√3)rect.3CO (Persson et al. [28])	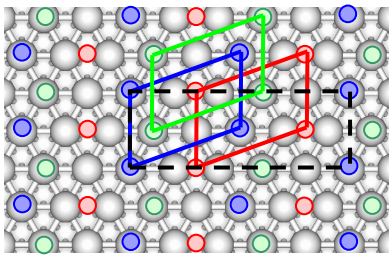	**LEED Pattern Obtained by Experiment** 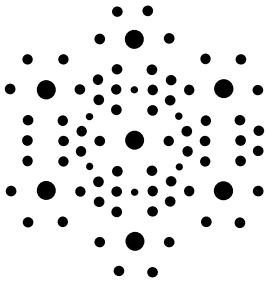	

Table 4.1. LEED patterns produced by the LEEDpat2 program for a hexagonal p3m1 2D lattice [38] consistent with that found experimentally for the 0.6 ML CO/Pt(111) adsorption system.

4.3.2 PhD Measurements on CO Adsorbed on Pt(111)

Using the chemical shift in the C 1s photoemission peaks (see fig.4.11) from two inequivalent C atoms for two different species of CO adsorbed on Pt(111), scanned-energy mode PhD was performed at the angles tabulated in Table 4.2 (see fig.4.12). The magnification was set to medium and the pass energy to 10 eV. The PhD scans were measured over a kinetic energy range of 68 eV – 372 eV and consisted of 93 EDC's, each 28 eV wide and 3 eV apart.

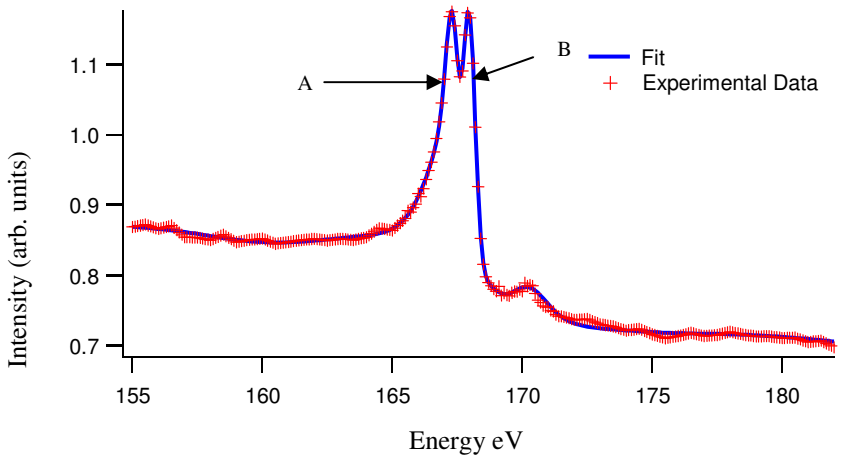

Fig.4.11 C 1s photoemission peaks for two species of CO on Pt(111), atop and bridge labelled A and B respectively.

θ / φ	0° Normal Emission	10°	20°	30°	40°	50°
[12$\bar{1}$]	✓	✓ ✓	✓	✓	✓	
[110]		✓	✓	✓ ✓	✓	✓
[21$\bar{1}$]		✓	✓	✓	✓	

Table.4.2**.** The polar (θ) and azimuthal (φ) angles at which the PhD scans were measured are indicated by the ticks. The spectra indicated by the red and blue ticks where selected for analysis on the basis of modulation strength. The red ticks indicate the spectra used for the atop species; the blue ticks indicate the spectra used for the bridge species.

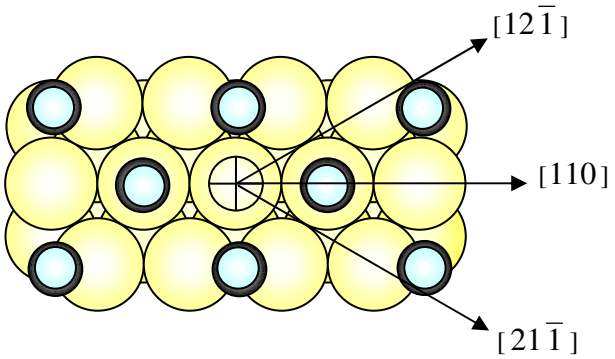

Fig.4.12. The azimuthal directions used in table 4.2; the 0^{o} polar angle is perpendicular to the page.

When fitting the data, care had to be taken to ensure that chemically equivalent sites were included in the theoretical models. For example, the bridge sites on the Pt(111) surface are chemically equivalent due to the symmetry of the crystal (see fig.4.13). Therefore, if a domain exists in which the CO molecules occupy certain bridge sites, other domains will exist in which the CO molecules occupy the other bridge sites. If there are six equivalent adsorption sites, six domains must be defined and therefore six symmetries must be included. If the number of symmetries included is too few, a false R-factor minimum may be obtained which may in turn suggest a false adsorbate position. Six symmetries were included in the analysis under discussion.

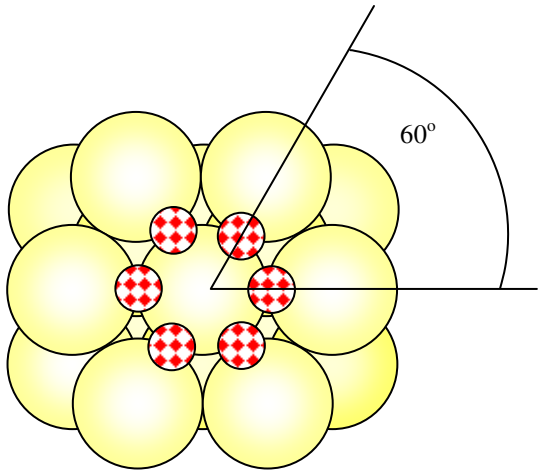

Fig.4.13. Equivalent bridge sites.

4.4 Results and Discussion

The results were integrated as detailed in chapter 2, to produce a modulation function for each direction in which the PhD scans were taken. The modulation functions (figs. 4.14 and 4.15) were used directly to obtain a general idea of the orientation of the adsorbate with respect to the substrate. Fig.4.14 shows that the modulation function for (A) shows stronger oscillations when compared with that for (B) when measured at normal emission. This is indicative of a high degree of backscattering suggesting that the Pt-C bond, represented by (A) is orientated in the direction of the analyser and therefore likely to be an atop species.

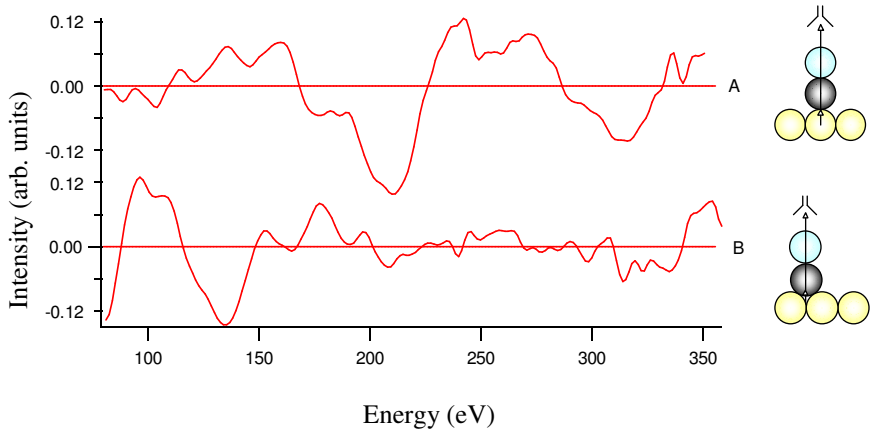

Fig.4.14 A corresponds to the modulation function produced from lower KE peak and B, from the higher KE peak. The chi curves are given relative to one another and represent intensity against energy. They have been offset on the y- axis for comparison.

However, when measured at 40° off normal emission in the [$\bar{1}$10] direction (see fig.4.15), the intensity of the modulation function for (A) decreases and that for (B) becomes dominant suggesting that the higher kinetic energy peak represented by (B) corresponds to the bridge species.

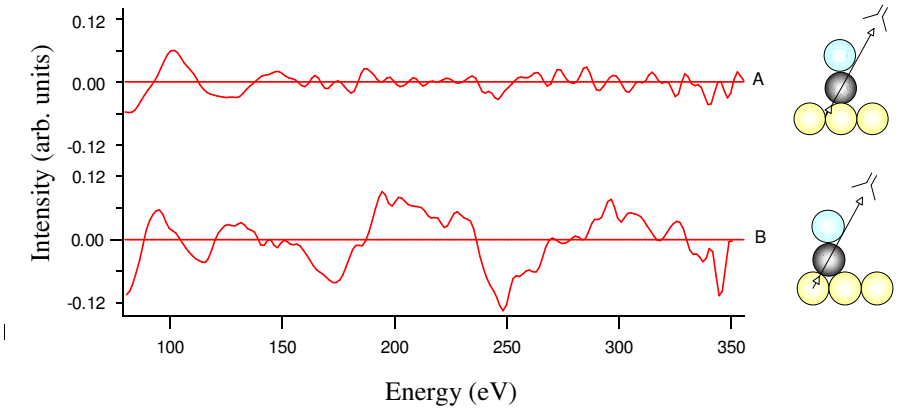

Fig.4.15 A is the chi curve for the lower KE peak at 40° off normal when analyzed in the [$\bar{1}$10] direction. B is that for the higher KE peak measured in the same direction.

This method is only qualitative but nevertheless, provides an initial indication of the probable adsorption sites and is consistent with the findings of F. Bondino et al. [40].

Even though all the previous publications point to preferential adsorption of CO at atop and bridge sites, hollow site adsorption was also considered. This was done by placing a single adsorbate on the surface in turn at the ideal atop, bridge, HCP and FCC adsorption positions and comparing the pre optimized R-factors for the low and high kinetic energy spectra (A and B). Table 4.3 shows that when using the low kinetic energy spectra, the atop site is clearly favoured giving an R-factor of 0.3512 with a var(R_{min}) value of 0.0656 which means that any site giving an R-factor greater than 0.4168 can be excluded. On the other hand, when the high kinetic energy spectra, are used the bridge site is clearly favoured giving an R-factor of 0.3441. This gives a var(R_{min}) value of 0.0704 meaning any site giving an R-factor greater than 0.4143 can be excluded.

Spectra	Atop	Bridge	HCP	FCC
A	0.3512	0.8527	0.9344	0.9071
B	0.9080	0.3441	0.9292	0.8945

Table 4.3 Comparison of R-factors for each adsorption site using the low and high kinetic energy spectra (A and B, respectively).

Once it was established that the PhD data was in agreement with previous studies in terms of preferential adsorption sites and the assignment of the C 1s XPS peaks [40], more comprehensive structural models were introduced.

While it has been generally accepted that at a coverage of 0.6 ML, a c(5x√3)rect. overlayer is formed, as highlighted in section 4.1.1, some controversy regarding the actual configuration of this overlayer has persisted. In an effort to settle this controversy, several configurations were analysed with particular attention being given to the following three models. Firstly, the c(5x√3)rect.-2CO proposed by Petrova et al. [27] (fig.4.16:A) consisting of an atop/bridge ratio of 1:2; that proposed by Avery [29] with a 2:1 ratio (fig.4.16:B) and finally, the 2:1 atop/bridge configuration proposed by Persson et al. [28] (fig.4.16:C).

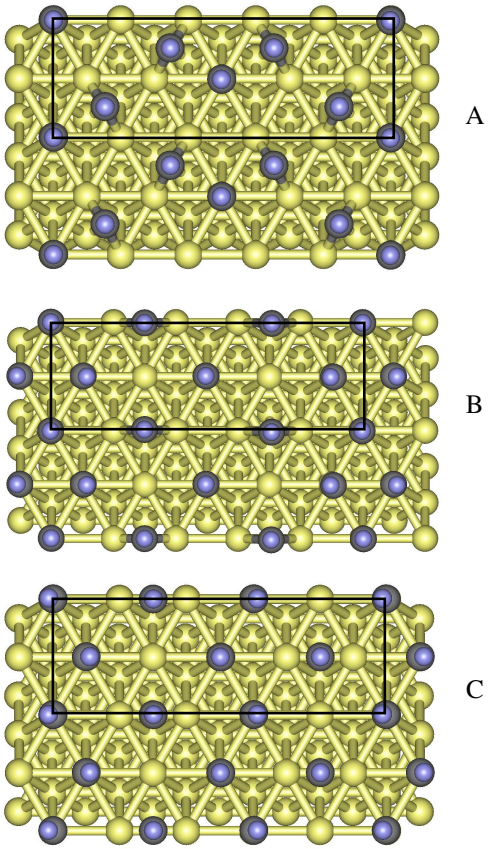

Fig.4.16 CO/Pt(111) Overlayer configurations proposed in the literature. A consisting of an atop/bridge ratio of 1:2 proposed by Petrova et al. [27]. B and C consisting of atop/bridge ratios of 2:1 proposed by Avery et al. [29] and Persson at al. [28] respectively.

The c(5x√3)rect.-3CO proposed by Petrova et al. [27] consisting of a 1:2 atop/bridge ratio finds little or no support in the literature. However the studies presenting evidence for a 2:1 ratio are not in agreement as to what form this 2:1 overlayer configuration takes. In order for Petrova's model to be properly eliminated a comprehensive PhD analysis had to be performed. The best achievable R-factors for this configuration were found to be 0.2246 using the atop spectra, 0.3221 using the bridge spectra and 0.2633 using the combined spectra. These R-factors resulted from the structural model shown in fig.4.17.

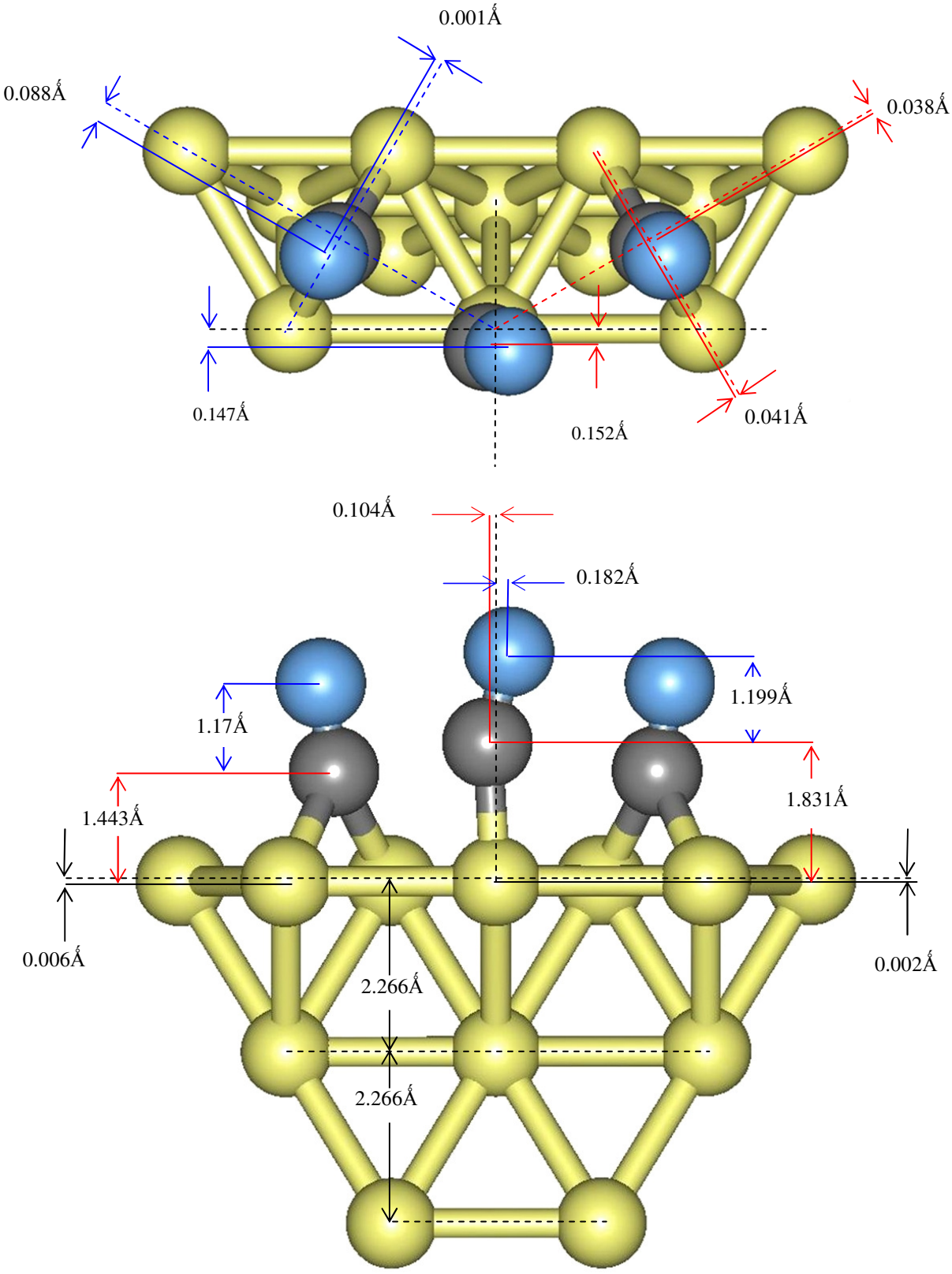

Fig. 4.17 Atomic displacement in the xyz directions for the theoretical model deduced from analysing atop and bridge spectra separately for the overlayer proposed by Petrova [27]. The reference lines are black and dashed, the solid red lines represent the carbon displacements, the solid blue lines represent the oxygen displacements and the solid black lines represent the substrate displacements.

While this model produces a reasonably good R-factor especially when the weak scattering ability of Pt is considered, a questionable result of this configuration is evident in the C-O bond lengths. The C-O bond length for the atop species is longer than that for the bridge species; 1.233 +0.087/-0.065 Å and 1.181 +0.36/-0.16 Å respectively. Admittedly, the discrepancy is somewhat lost in the variance but such a discrepancy can be an indication that other parameters are incorrect. A hint as to what this might be can be found in the XPS data. The high resolution spectrum shown in fig.4.9 reveals that the intensity of the atop peak appears to be approximately twice that of the bridge peak. Assuming the cross sections are equivalent, the XPS suggests that a 2:1 atop/bridge is more likely and this could be the cause of the anomalous bridge C-O bond length. However, the peak intensities are subject to modulations as a photoelectron energy is changed meaning that a peak comparison must be carried out over a wide range of energies. To this end, a comparison of the peak intensities was carried out for each of the 93 EDC's over a kinetic energy range of 68 eV – 372 eV. This resulted in an average ratio of 1.31:1 for the Atop/Bridge intensities. Including the shoulder of the Atop peak which is possibly the result of some vibrational modes, this ratio is increased to 1.70.

PhD does not depend on absolute peak intensities but on the intensity modulations. This means that, while an excellent tool for the determination of the local structure about an emitting atom, PhD is not sensitive to the quantity of adsorbates present or the long range order of the overlayer. However the various overlayers proposed in the literature are composed of differing local structures which are translated across the surface. This is where the strength of PhD becomes apparent.

As mentioned in section 4.1.1, support for the increased atop/bridge ratio at 0.6 ML is provided by Avery et al. [29] and Persson et al. [28] and is arguably supported by the current XPS analysis. It should be noted that Avery's model has strictly a (√3 x 5)rect. periodicity, and not c(√3 x 5)rect. which should lead to additional LEED beams not reported in the experiments; admittedly these additional beams may be weak.

The best achievable R-factors for Avery's model were found to be 0.221, 0.3119 and 0.2606 using the atop, bridge and combined spectra, respectively. The structural model from which these R-factors are derived is depicted in fig. 4.18.

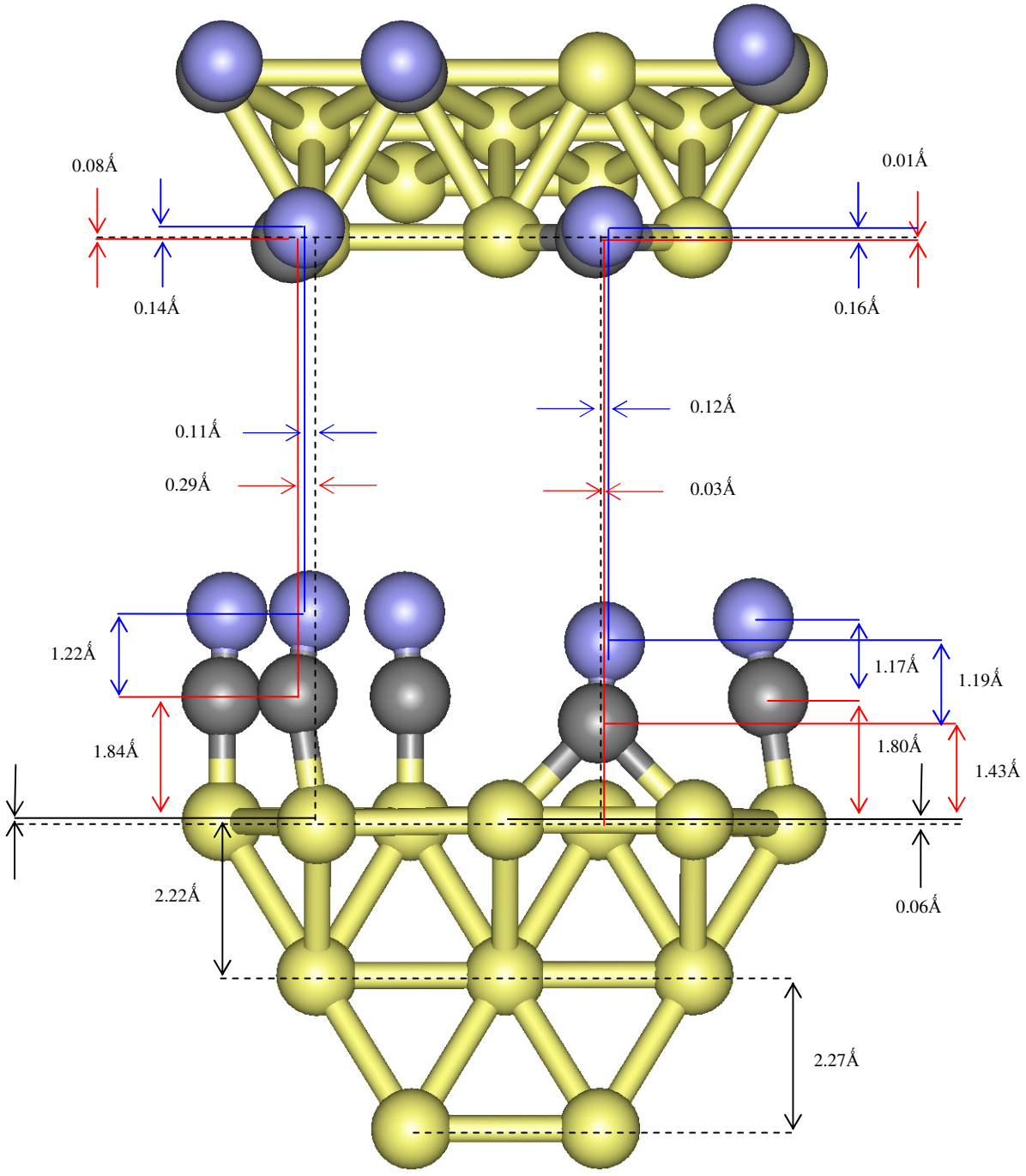

Fig. 4.18 Atomic displacement in the xyz directions for the overlayer proposed by Avery [29]. The reference lines are black and dashed, the solid red lines represent the carbon displacements, the solid blue lines represent the oxygen displacements and the solid black lines represent the substrate displacements.

The c(5x√3) rect.3CO proposed by Persson et al. [28] consisting of 4 atop and 2 bridge species per unit cell (fig.4.17, A), relies on the verification of a simulation model by the experimental data from two different techniques, namely LEED and IRAS (infrared absorption spectroscopy). Despite the breadth of this methodology, the data presented is by no means conclusive; the LEED findings are contested by the more recent LEED study by Petrova et al. The IRAS results presented, seem resistant to the proposal that the bridge coverage decreases as θ approaches 1 ML, showing no consistent trend, forcing Persson et al. to speculate on other contributing factors in order to explain the anomalous results.

Support for Persson's model can be found in the STM study carried out by Song et al. [30]. They present an STM image consisting of the c(4x2) and the c(5x√3) structures. The c(5x√3) region exhibited strips in the [11$\bar{2}$] direction, with a spacing of 2 and 3 Pt atoms apart. If Avery's model were correct, a strip spacing of 4 and 5 Pt atoms would be expected (see fig. 4.19).

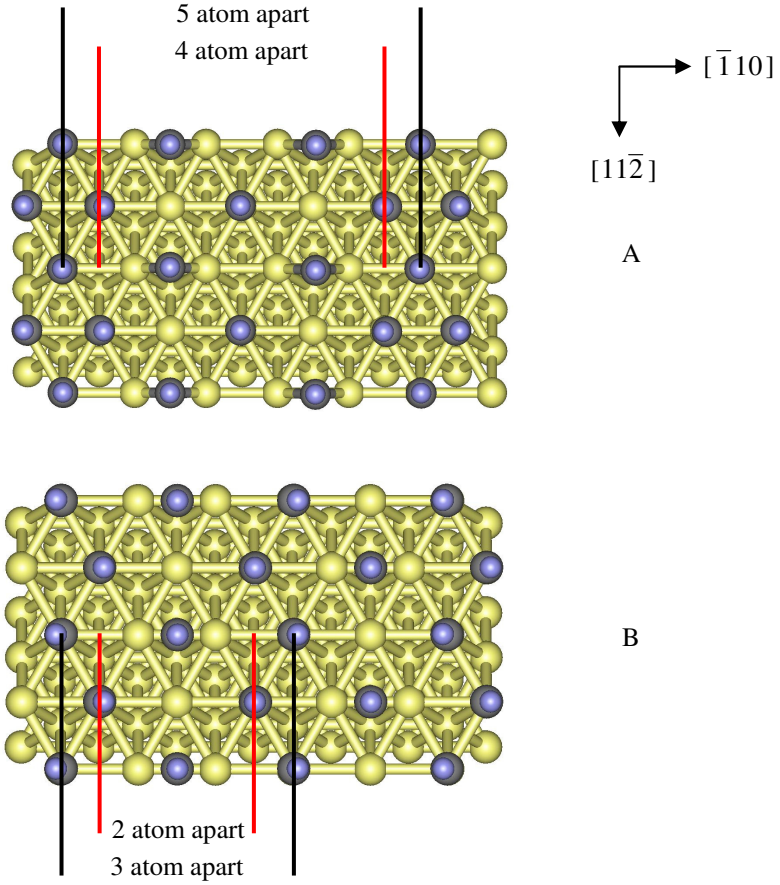

Fig. 4.19 Comparison of strip spacing for the overlayers proposed by Avery [29] and Persson et al. [28]. A shows a spacing of 4 and 5 atoms for Avery's model and B shows a spacing of 2 and 3 atoms for Persson's model.

Further support is given by the PhD analysis in this thesis. Of the three models analysed Persson's model yields the most convincing results. The best achievable R-factors for the c(5x√3)rect.-3CO proposed by Persson et al. for the atop and bridge species were found to be 0.1897 and 0.2523 respectively. The best combined R-factor was found to be 0.2403. As shown in fig.4.20, the analysis using the combined atop and bridge spectra is unable to exclude Avery's and Petrova's models in terms of the variance. However, Petrova's model can be excluded when using the atop spectra alone, and both Avery's and Petrova's models can be excluded when using the bridge spectra alone. This sensitivity arises from the fact that the configuration of the atop species is symmetrical about the bridging emitter in Persson's model but not in Avery's.

Note that Persson's analysis was carried out at 50 K yet is consistent with the current analysis undertaken at 150 K. According to Blackmann et al. [22] and Pedersen et al. [26], the c(4x2) structure at 0.5 ML remains stable at RT which is consistent with the findings of Beutler et al. [41], who in their core level photoemission study observe a CO desorption temperature of 365 K at a coverage of 0.5 ML, Beutler also observes a desorption temperature of 335 K at a coverage of 0.6 ML meaning that the c(5x√3)rect.-3CO structure is likely to be stable at room temperature.

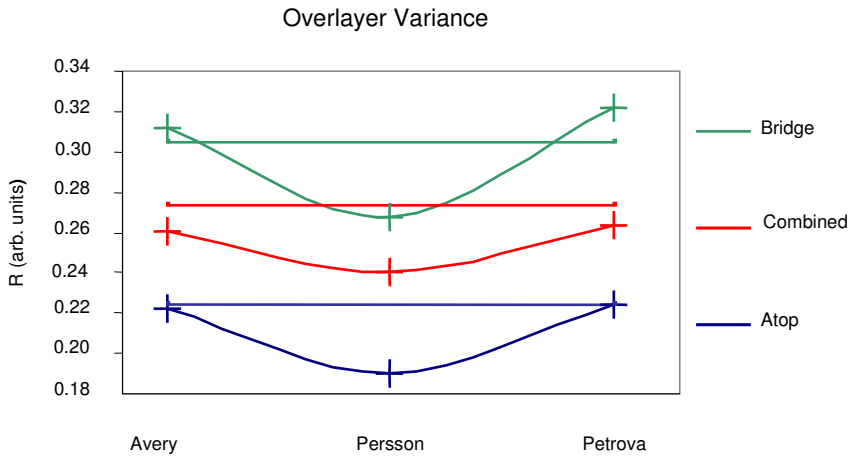

Fig.4.20. Graph showing the variance for the three overlayer configurations under discussion.

In addition to determining the adsorption site configuration, other parameters such as adsorbate bond lengths and tilt angles were analysed. Until now no bond lengths for the 0.6 ML system have been reported, however the relevance of such information detailed for the c(4x2) overlayer has already been elucidated. Both the 0.5 ML and 0.6 ML systems consist of atop and

bridge species which means the bond orders are equivalent. Based on the DFT and PhD work undertaken by D.P.Woodruff et al. [33] bond lengths are more influenced by bond order than bond strength. Therefore bond lengths similar to those obtained for the c(4x2) system can be expected for the c(5x√3)rect. system.

PhD is particularly sensitive to adsorbate bond lengths especially when measured at an angle which maximises the backscattering signal. The graphs in fig. 4.21 reveal the high precision with which the C-Pt bond lengths can be measured, particularly when the atop species is measured. In all of these plots the variance is represented by the horizontal pink line. Values of 1.86 ± 0.02 Å and 2.01 ± 0.05 Å were achieved for the Pt-C_{atop} and Pt-C_{bridge} bond lengths, respectively.

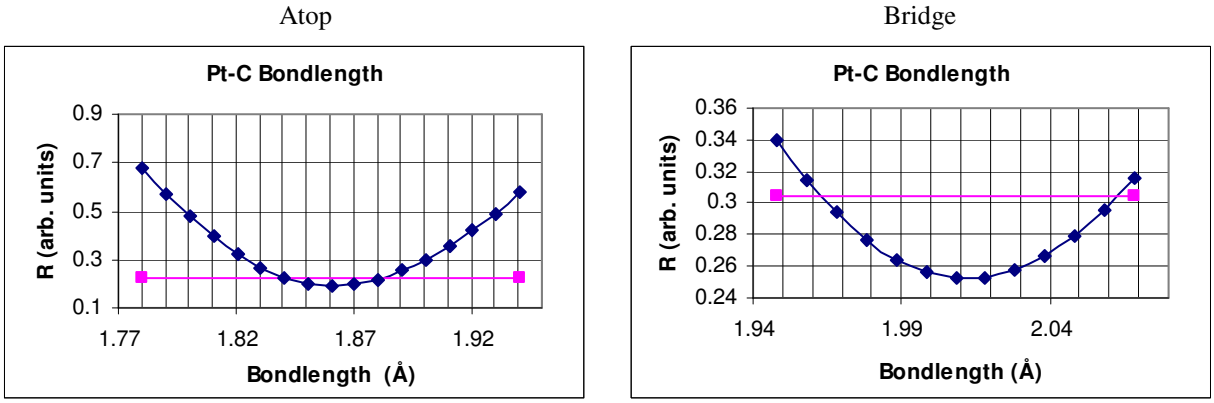

Fig. 4.21**.** The C positions are defined with respect to the associated Pt atoms by the C-Pt bondlengths and the corresponding azimuthal (φ) and polar angles (θ), taking the centre of the Pt atoms as the origin. The atop and bridge C-Pt bondlengths were found to be 1.86 ± 0.02 Å and 2.01 ± 0.05 Å, respectively.

Sensitivity to the C-O bond lengths is less pronounced (fig. 4.22); here the values were found to be 1.24 +0.05/-0.04 Å and 1.25 +0.16/ -0.14 Å for the atop and bridge species, respectively. Nevertheless, the findings of D.P.Woodruff et al. [33] are substantiated by the results. The most agreed upon Pt-C_{atop} and Pt-C_{bridge} bond lengths for the 0.5 ML system are reported to be 1.85 Å and 2.01 Å [22, 24, 32], respectively compared with 1.86 Å and 2.02 Å for the 0.6 ML system reported here showing excellent agreement.

Atop

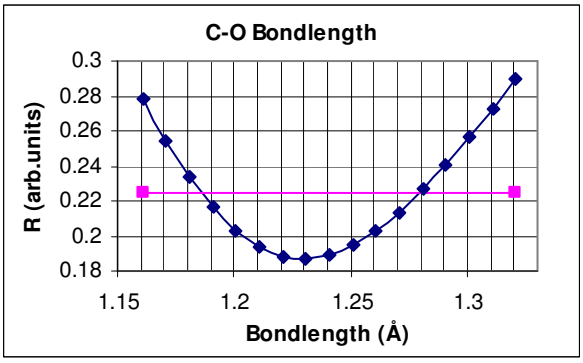

Bridge

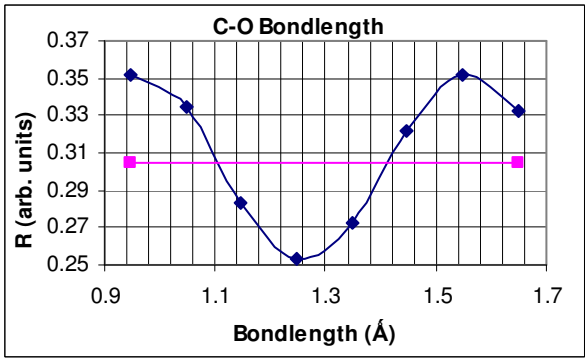

Fig. 4.22. The O position with respect to the associated C atoms and are defined by the O-C bondlengths and the corresponding azimuthal (φ) and polar angles (θ) taking the centre of the C atom as the origin. The values of these parameters are plotted respectively giving values of 1.24 +0.05/-0.04 Å and 1.25 +0.16/-0.14 Å for the atop and bridge species.

The sensitivity of the modelling procedure to molecular bond lengths and other parameters such as the polar and azimuthal bond angles, is influenced by their interdependence on one another. For example, the longer the theoretical Pt-C_{atop} bond length the greater the atomic displacement when the polar angle is varied and similarly; the greater the polar angle, the greater the displacement when the azimuthal angle is varied. However, this has to be weighed against the fact that PhD is less sensitive to lateral displacements than it is to nearest neighbour interatomic distances. This is evident in the values for the Pt-C_{atop} and Pt-C_{bridge} polar bond angles which were found to be 10.7^{o} + 1.5°/-3.1° and 43.6^{o} ± 1.5° respectively (fig. 4.23). This translates to lateral displacements of 0.34 +0.05/-0.10 Å and 1.39 ± 0.04 Å relative to the associated Pt atom. While a reduction in sensitivity is evident, a high degree of precision is still reflected in these results.

The tilt in the C-O_{atop} species occurs as the system accommodates the O-O repulsion. If it is assumed that the O-O repulsion is the same for both the atop and bridge species and that the C-O bond axis points to the centre of the metal atom, a tilt of ~8.4° would result in the O atoms being equidistant from one another. However the O_{atop}-O_{atop} repulsive force is greater than the O_{atop}-O_{bridge} force due to the greater negativity of the O_{atop} arising from the C≡O triple bond, meaning that a tilt greater than ~8.4° can be expected. This is consistent with the Pt-C_{atop} angle of 10.7° + 1.5°/-3.1° obtained from PhD. The values for the tilt of the C-O bond axis of 15.4° + 6.1°/-6.7° (see fig.4.24) are too great to discriminate between a linear or kinked Pt-C-O structure. These results are consistent with the 10° tilt proposed by Persson et al. [28].

Kiskinova et al. [34] in their ESDIAD investigation propose a tilt of 6º ± 1º which is only slightly lower than the minimum allowed by the PhD results. However, the model they propose does not provide a good explanation of their results. For example, their model includes three inequivalent atop sites yet all of the CO species showed the same tilt of 6º ± 1º. They suggest that the CO^+ originating from the second site in the fault line is strongly quenched due to the proximity of the neighbouring terminal-CO species, but give no explanation for the observation of the atop species equivalent to that in the measurements on the c(4 x 2) phase. A second possible explanation they give for their anomalous results which is in agreement with the PhD results is that the fault-line structure they present is incorrect.

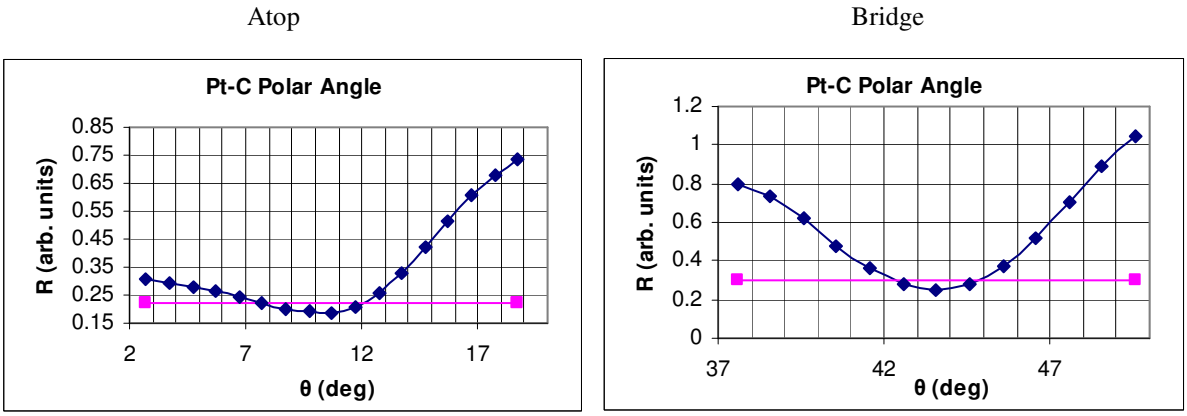

Fig. 4.22. Variance plot for the Pt-C_{atop} and Pt-C_{bridge} polar bond angles; 10.7º + 1.5º/-3.1º and 43.6º ± 1.5º respectively.

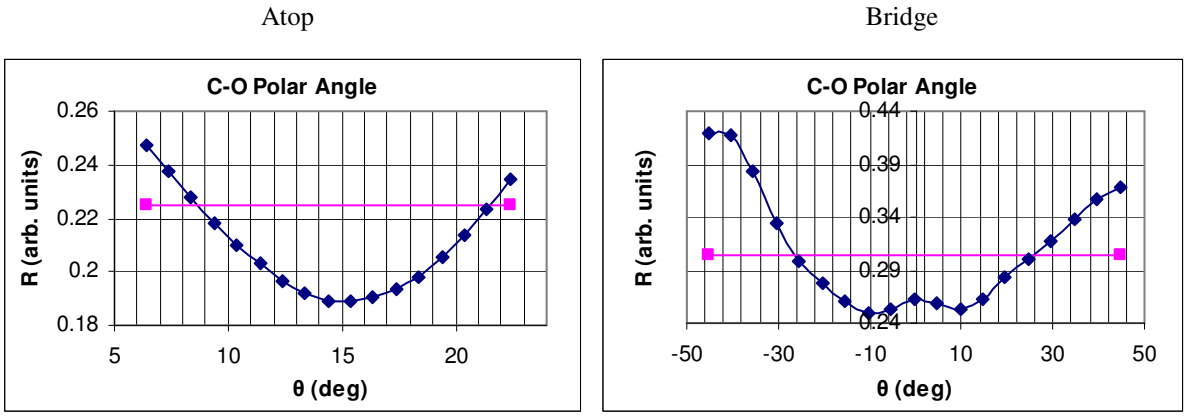

Fig. 4.24. Variance plot for the C-O_{atop} and C-O_{bridge} polar bond angles; 15.4º + 6.1/-6.7 and 8.3º +36/-20 respectively.

The variance plots for the azimuthal angle of the Pt-C_{atop} and Pt-C_{bridge} bonds show little resemblance to one another (fig. 4.25). This however, is more to do with the physical

constraints on the adsorbate species rather than the imprecision of the experiment. The seemingly poor variance of 30.4° +33/-24 for the Pt-C_{atop} as compared with that of the Pt-C_{bridge} species (-0.24° +5°/-6°) is likely a result of the shallow potential energy surface curve governing atop adsorption [25] and the contrastingly deep potential energy surface curve governing bridge adsorption [42]. Additionally, the small tilt in the atop species means that changing the azimuthal angle results in very little displacement.

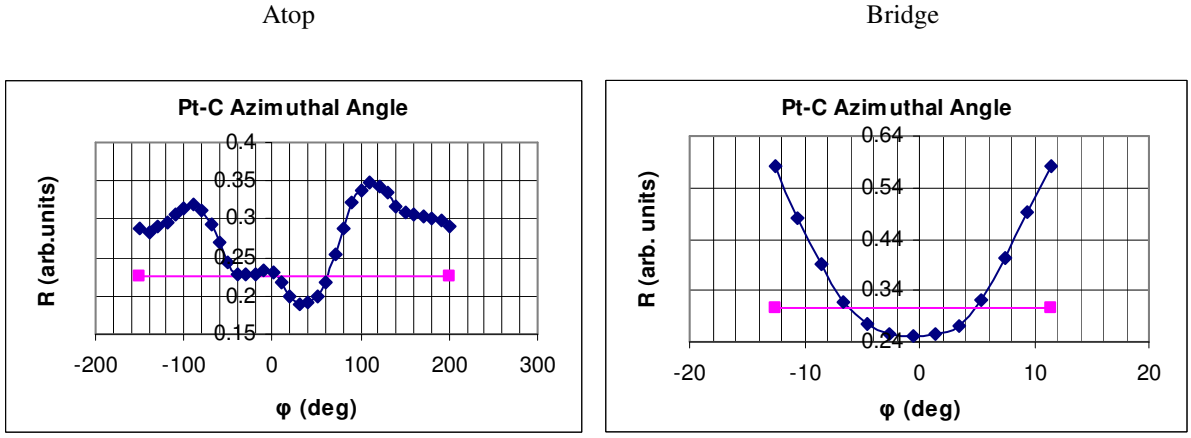

Fig. 4.25. Variance plot for the Pt-C_{atop} and Pt-C_{bridge} azimuthal bond angles; 30.4° +33/-24 and -0.24° +5/ -6 respectively.

As for the azimuthal bond angle of the C-O_{atop} and C-O_{bridge}, neither can be expressed with any significant precision (fig.4.26); 107° +33°/-222° and -31.6° ± ∞° respectively. This is in part, because PhD is more sensitive to the position of the nearest neighbouring atoms in the backscattering direction than those in the forward scattering direction. Additionally, the influence of the potential energy surface curve may also be significant factor.

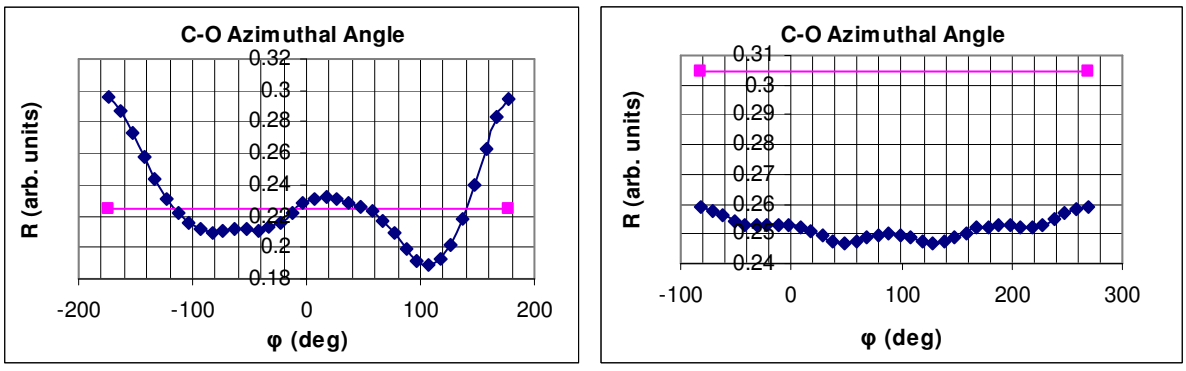

Fig. 4.26. Variance plot for the C-O_{atop} and C-O_{bridge} azimuthal bond angles; 107° +33°/-222° and -31.6° ± ∞° respectively.

A direct comparison of the theoretical and experimental modulation functions for these parameters is shown in figs. 4.27 and 4.28. Eleven spectra were used, six for the atop species and five for the bridge species. Graphs A to F represent the experimental and current theoretical modulation functions for the CO_{atop} species. Graphs G to K represent those for the bridge species.

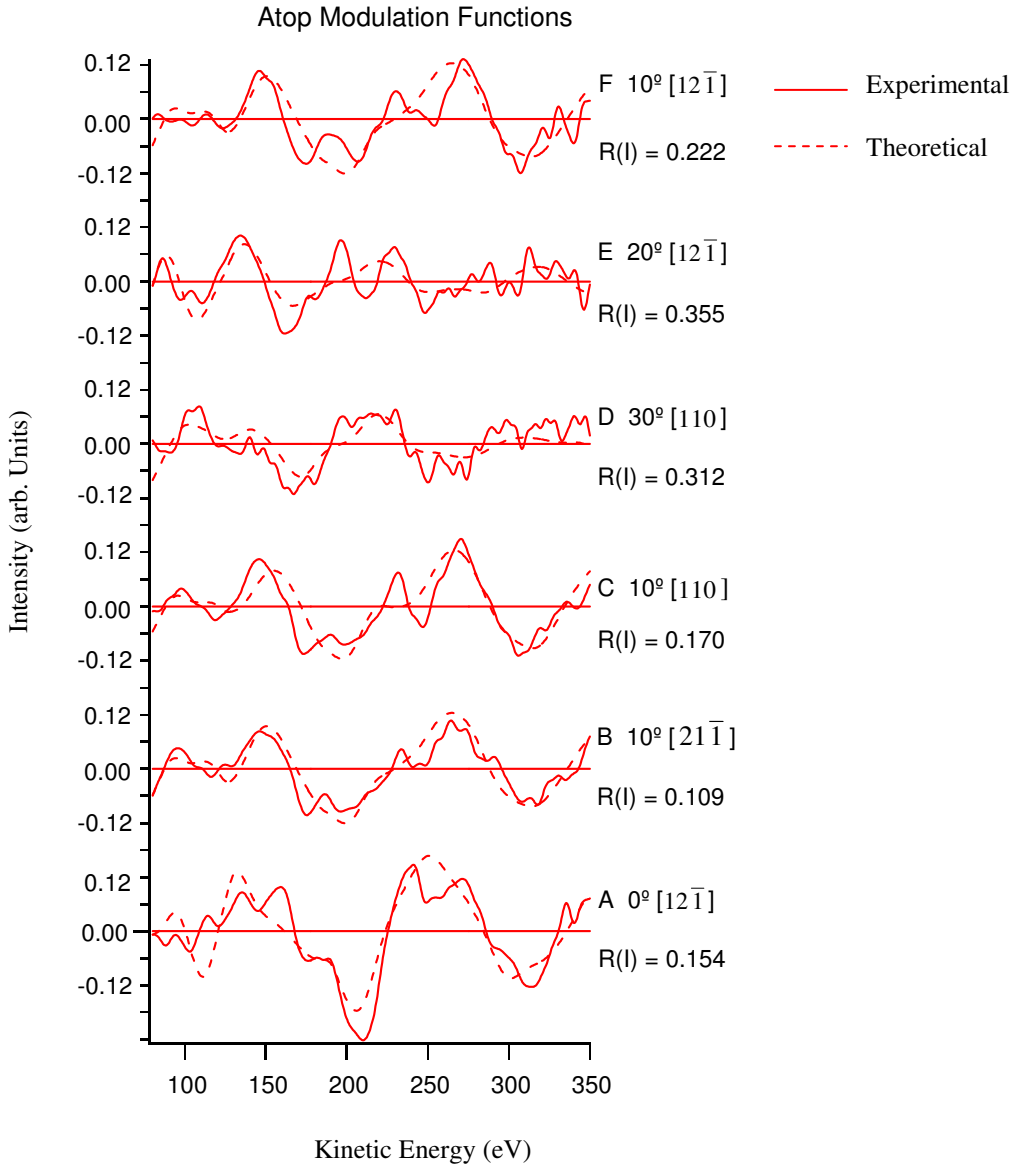

Fig.4.27 Comparison of experimental (red) and simulated (red dotted) modulation functions for atop species for the overlayer proposed by Persson et al. [28].

All of the graphs in fig. 4.27 show good agreement between the experimental and theoretical modulation functions. This is particularly true of graphs A - C where the polar emission angle is comparable to the atop adsorbate tilt angle. Similarly, on consideration of the bridge spectra, the best agreement between the experimental and theoretical modulation functions is achieved

when measurements in the Pt-C bond direction (see graphs H and J). This owes to the fact, as previously mentioned, that the signal to noise ratio is maximised in these circumstances.

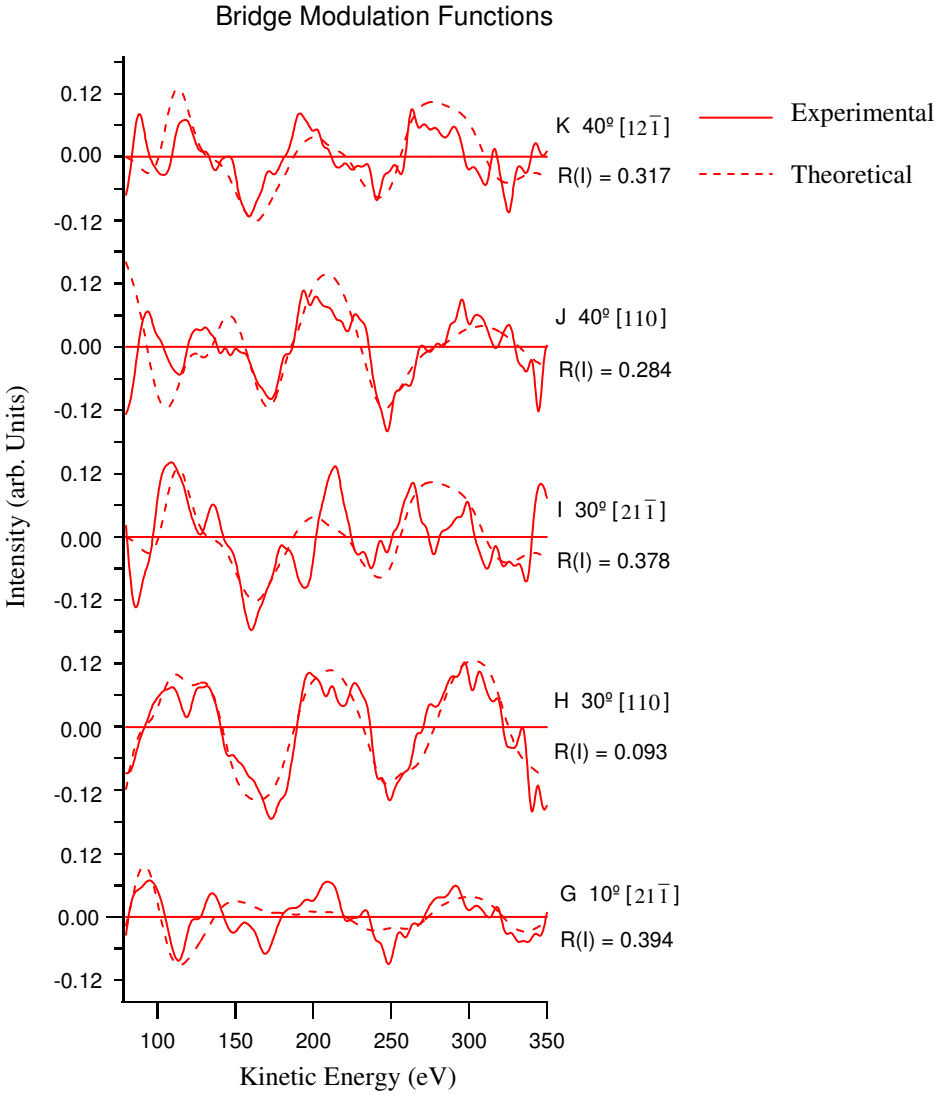

Fig.4.28 Comparison of experimental (red) and simulated (red dotted) modulation functions for bridge species for the overlayer proposed by Persson et al. [28].

The theoretical parameters, from which the above modulation functions were produced, are included in table 4.4 and diagrammatically represented in fig.4.29.

<table>
<tr><th>Parameter</th><th colspan="3">PhD results for the
c(5x√3) rect.3CO

R-factor$_{Atop}$ = 0.1897
R-factor$_{Bridge}$ = 0.2523</th><th colspan="4">Literature values for the
c(4x2)-2CO</th></tr>
<tr><td></td><td colspan="3">Bond lengths (Å)</td><td>[31]
DFT</td><td>[32]
DFT</td><td>[24]
LEED</td><td>[26]
STM</td></tr>
<tr><td>Pt-C$_{atop}$</td><td colspan="3">1.86 ± 0.02</td><td>1.86</td><td>1.85</td><td>1.85±0.1</td><td>1.80</td></tr>
<tr><td>Pt-C$_{bridge}$</td><td colspan="3">2.02 ± 0.04</td><td>1.94</td><td>2.01</td><td>2.01±0.07</td><td>1.51</td></tr>
<tr><td>C-O$_{atop}$</td><td colspan="3">1.24+0.05/ -0.04</td><td>1.13</td><td>1.15</td><td>1.15±0.05</td><td>1.15</td></tr>
<tr><td>C-O$_{bridge}$</td><td colspan="3">1.25 +1.15/ -1.48</td><td>1.16</td><td>1.18</td><td>1.15±0.05</td><td>1.15</td></tr>
<tr><td></td><td colspan="3">Bond Angle</td><td colspan="4"></td></tr>
<tr><td></td><td>θ</td><td>φ</td><td></td><td colspan="4" rowspan="4">N/A</td></tr>
<tr><td>Pt-C$_{atop}$</td><td>10.7° + 1.5°/-3.1°</td><td>30.4° +33°/-24°</td><td></td></tr>
<tr><td>Pt-C$_{bridge}$</td><td>44.1° +1.0°/-1.5°</td><td>-0.24° + 2.05°/-8.85°</td><td></td></tr>
<tr><td>C-O$_{atop}$</td><td>15.4° + 6.1°/-6.7°</td><td>107° +33°/-222°</td><td></td></tr>
<tr><td>C-O$_{bridge}$</td><td>8.3° +12.7°/-29.8°</td><td>-149.2° ± ∞°</td><td></td></tr>
<tr><td colspan="4">Relaxation (Å)
 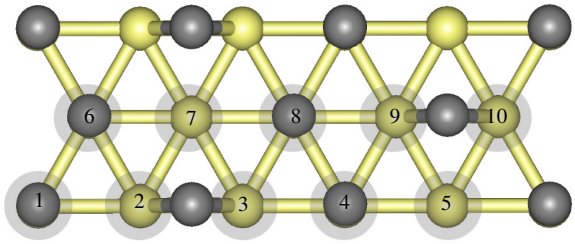
</td><td colspan="4">Relaxation (Å)
(c(4x2)-2CO)
 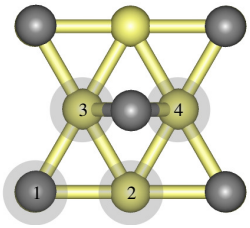

[37]</td></tr>
<tr><td colspan="2">Pt$_1$, Pt$_4$ Pt$_6$, Pt$_8$
Pt$_2$, Pt$_3$, Pt$_9$, Pt$_{10}$
Pt$_5$, Pt$_7$</td><td>0.016
0.010
-0.050</td><td>+2.6/-1.0</td><td>Pt$_1$</td><td colspan="3">0.006</td></tr>
<tr><td colspan="4"></td><td>Pt$_2$</td><td colspan="3">-0.06</td></tr>
<tr><td colspan="4"></td><td>Pt$_3$</td><td colspan="3">0.006</td></tr>
<tr><td colspan="4"></td><td>Pt$_4$</td><td colspan="3">0.006</td></tr>
<tr><td colspan="8"></td></tr>
<tr><td colspan="2">Vibrational Amplitudes</td><td colspan="2">(Å^2)</td><td colspan="4"></td></tr>
<tr><td colspan="2">Pt</td><td colspan="2">0.005</td><td colspan="4" rowspan="3">N/A</td></tr>
<tr><td colspan="2">C</td><td colspan="2">0.004</td></tr>
<tr><td colspan="2">O</td><td colspan="2">0.005</td></tr>
</table>

Table 4.4. Structural parameters for the c(5x√3) rect-3CO overlayer compared with the structural parameters for c(4x2)-2CO presented in the literature.

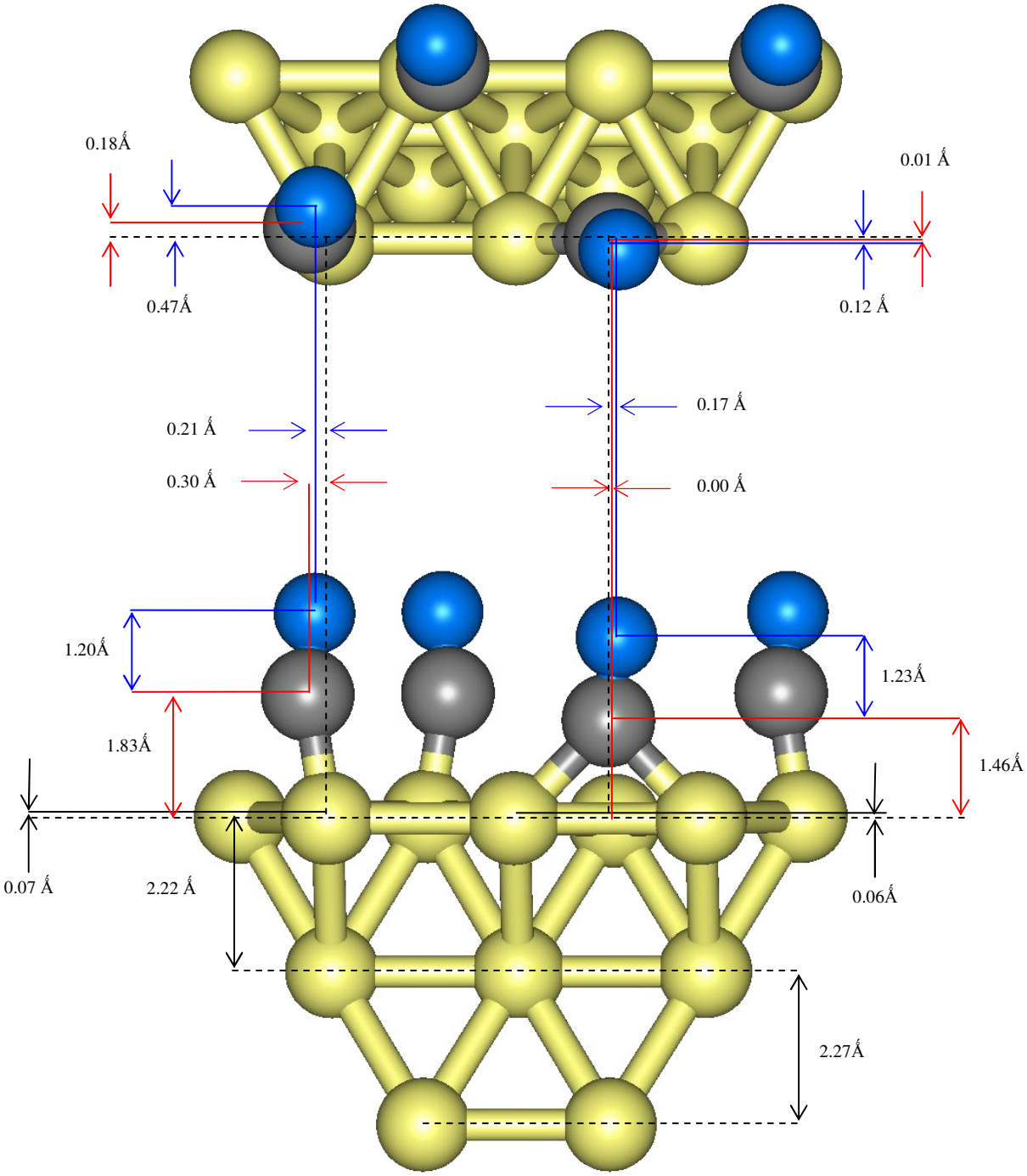

Fig. 4.29 Atomic displacement in the xyz directions for the overlayer proposed by Persson et al. [28]. The reference lines are black and dashed, the solid red lines represent the carbon displacements, the solid blue lines represent the oxygen displacements and the solid black lines represent the substrate displacements.

4.5 Conclusion

PhD, by itself, is not suited to the determination of overlayer composition but rather the local structure about an emitting atom. However, when used in conjunction with XPS and a long range technique such as LEED, the surface composition can be ascertained.

The LEED pattern obtained in this work for the 0.6 ML system is consistent with those presented by Persson et al. and Petrova et al and reveals that a long range ordered c(5x√3)rect.3CO overlayer was achieved. The XPS results support the 2:1 atop/bridge ratio proposed by Persson et al. and is further substantiated by the PhD results yielding R-factors of 0.1897, 0.2523 and 0.2403 using the atop, bridge and combined spectra respectively.

The Pt-C_{atop} bond length for the 0.6 ML system was determined to be 1.86 Å, just 0.01 Å longer than the corresponding atop species for the 0.5 ML system. The Pt-C_{bridge} bond length was found to be 2.01 Å which is identical to the corresponding bridge species in the 0.5 ML system. The difference in the atop bond lengths may be real but can not be stated with a certainty greater than that permitted by the variance which in this case ± 0.02 Å.

The C-O bond lengths are significantly longer than those reported for the c(4x2) system (1.24 +0.05/-0.04 Å compared with 1.15±0.05 Å), although the difference falls within the variance. The C-O bond length for the bridge species (1.25 +0.16/-0.14 Å) is sensibly longer than that for the terminal species but again the difference falls within the variance.

The tilt of the terminal Pt-C bond was found to be 10.7º +1.5/-3.1 which is in good agreement with that of 10° proposed by Persson et al. [28]. The C-O_{Atop} tilt was found to be 15.4º +6.1/-6.7 with an azimuthal angle of 107º +33º/-222º which, considering the variance, is consistent with a non-kinked configuration. The C-O_{Bridge} tilt was found to be 8.3° +12.7º/-29.8º, which, as allowed by the variance, is consistent with a vertical orientation.

5 Surface Structure of Si(001)(2x2)-C_6H_6

5.1 Introduction

There is considerable interest in studying the interaction between benzene and the technologically significant Si(001) surface. This interest arises due to the fact that the benzene/Si(001) system is considered to be a promising precursor for technologically relevant processes, such as the growth of Si-C and chemical vapour deposition of diamond thin films on Si surfaces [9]. The technological relevance of this is that diamond is a wide band-gap semiconductor and as such might be an ideal material for high power, high frequency or high temperature applications [43]. While this interest has been the impetus for numerous studies, there still remains some controversy regarding the adsorbate/substrate structure. The aim of this portion of research is to provide a full analysis of the benzene/Si(001) adsorption system at a saturation coverage of 0.25 ML using PhD.

5.1.1 Clean Si(001)

The Si(001) surface has been well studied and characterised because this is typically the surface plane of interest in the microelectronics industry [44, 45]. Reconstruction of clean Si(001) occurs such that pairs of nearest-neighbour surface Si atoms dimerize to produce a characteristic (2x1) unit mesh defined with respect to the ideal truncation of the bulk structure [46] (see fig.5.1). In this way, a lower surface free energy configuration is accommodated.

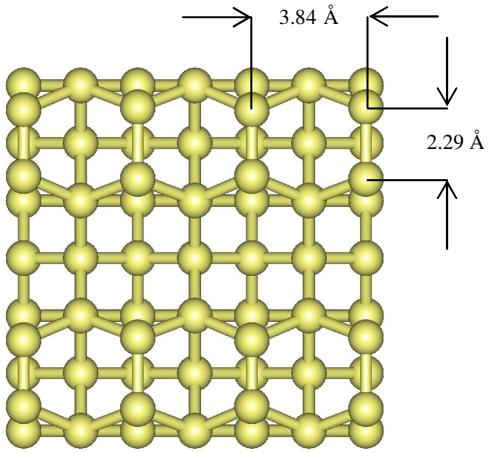

Fig. 5.1. Clean Si(001) exhibiting the (2x1) dimer configuration.

5.1.2 Benzene Adsorption

According to the thermal desorption studies of Taguchi et al., C_6H_6 (C_6D_6) is the only desorption product observed from the saturated benzene/Si(001) system [47, 48] indicating that benzene adsorption is molecular without any bond dissociation; a conclusion which finds little or no opposition. Furthermore, the Si-Si dimers also remain intact [44, 49, 50]. While benzene is the simplest molecule in the class of aromatic hydrocarbons, it can still theoretically adsorb in a myriad of different configurations. The number of possible adsorption configurations is significantly reduced by assuming the absence of any dissociated species. With this consideration, six different structural models of adsorbed benzene were investigated (fig.5.3), all of which have been proposed elsewhere for room temperature adsorption [9, 48, 52, 53, 57, 59, 61].

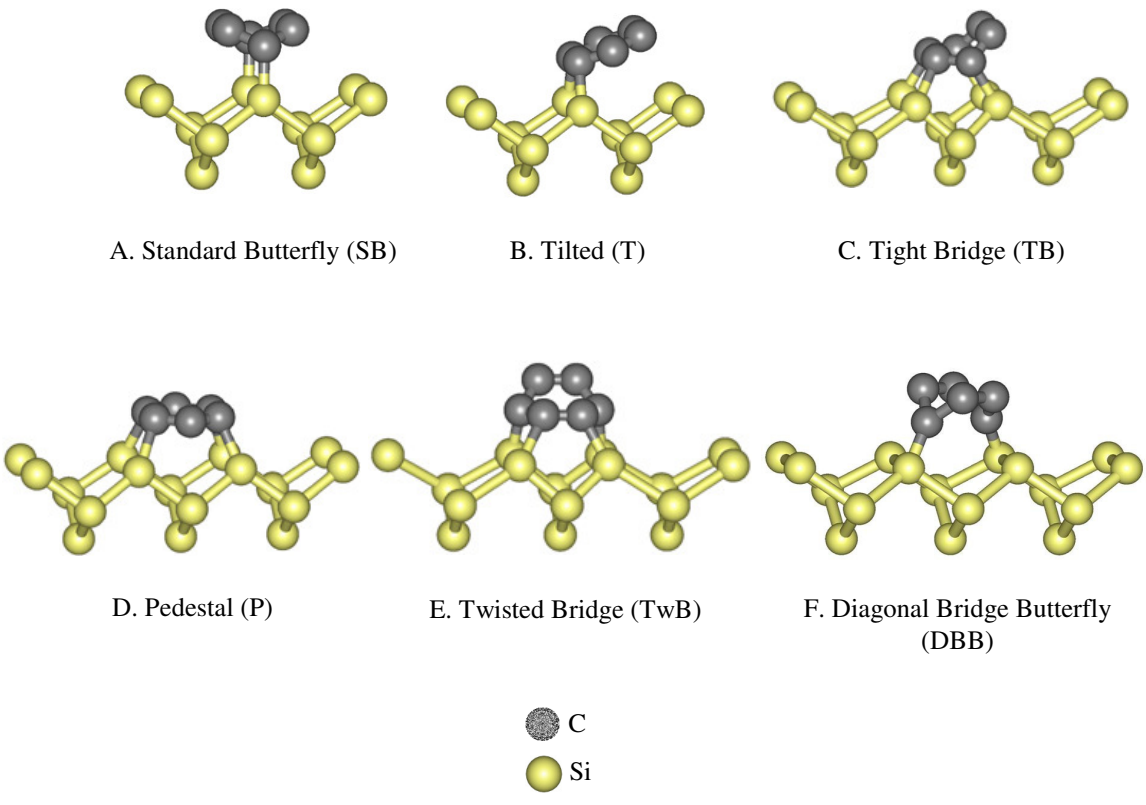

Fig.5.3. Diagram of the SB model [9, 48, 52, 53, 57, 59, 61], the T model [52], the TB model [9, 52, 53], the P model [52, 56], the TwB model [52] and the DBB model [9]. A and B are single dimer configurations, the rest are double dimer configurations. The colour scheme used here will be used throughout the chapter i.e. gray for the C atoms and yellow for the Si atoms.

5.1.3 Low Coverage

The majority of the studies pertaining to benzene adsorption on Si(001) measured at low coverage (< 0.5 L), agree that adsorption occurs initially in the single-dimer butterfly configuration. [51, 52, 9, 53, 55].

Borovsky et al. [51] using STM, observed two adsorption configurations; a metastable, symmetrical, configuration consistent with the single dimer butterfly species which then converts to a lower energy final state with a time constant of 19 min (the time required for the concentration of the SB species to drop by 36.7% (see equation 5.1). The configuration of this final state draws some controversy as Borovsky favours the tilted configuration as the most likely candidate. Wolko et al. [52] on the other hand, using STM with molecular orbital methods also proposed that benzene adsorption occurs initially in a metastable butterfly configuration but then conforms to the tight bridge configuration with a time constant of 25 ± 0.83 min.

$$A_t = A_0 e^{-t/a} \qquad 5.1$$

where A_0 = amount of substance at time 0

A_t = amount of substance at time t

a = time constant

Support for Wolko's conclusions is provided by the first principles study undertaken by Silvestrelli et al. [9]. They also concluded that the tight bridge configuration is favoured and occurs via the di-σ-bonded metastable butterfly structure. However, they propose three possible butterfly configurations; namely the standard butterfly, the diagonal bridge butterfly (DBB fig. 5.3.F) and the tilted diagonal bridge butterfly (TDBB) which is modelled in this work as a simple variation of the DBB model.

Hofer et al. [53] in their STM image analysis by *ab initio* methods of benzene adsorption on Si(001), consider the first five of the structural models shown in fig.5.3. The tilted and pedestal models are dismissed because of the instability suggested by their low adsorption energy. The twisted bridge, they argue is only associated with type-C defects (discussed in section 5.3.5) and is outside the concern of their paper. They conclude that the (1,4) single-dimer

configuration is the metastable chemisorbed state of benzene, while the binding state is the tight bridge across two dimers. An observation worth mentioning is that in another paper [54], their simulations for the TB model predict a lowering of the adsorption energy with increased benzene coverage. Further support for the butterfly and TB configurations is provided by Kruse et al. [55].

5.1.4 Saturation Coverage

Gokhale et al. [49] using a combination of TPD, ARUPS and DFT, discuss only three of the possibilities presented in fig.5.3; namely the SB, TB and P configurations. They conclude that the former is the most stable configuration and make no reference to it being of a metastable nature. It is worth noting at this point that this analysis was carried out for a saturated system in contrast to those mentioned above. Jeong et al. [56] however, in their semi-empirical study, suggest that the pedestal configuration is the most likely structure. A conclusion which proved only to be a minor interruption to the accretion of corroborating analyses.

Birkenheuer et al. [57] in their DFT analysis of benzene adsorption on Si(001), highlight three main characteristics of their proposed model, that is, the structure must exhibit: a local C_{2v} symmetry, di-σ bonding towards the Si Surface, and at least one C-C double bond. These characteristics of course, are only exhibited in the SB configuration.

Witkowski et al. [58], like Gokhale and Jeong, discuss only the tilted, pedestal and standard butterfly configurations. Using fully polarization-resolved NEXAFS, they observe that the benzene ring lies distorted on the surface. In particular, they argue that the molecule is tilted in a manner consistent with the butterfly and tilted models. On further analysis, they conclude that the molecule is symmetric with respect to the dimer axis, excluding an ordered asymmetric tilted configuration. Thus the adsorbed geometry is attributed to the butterfly configuration where the benzene is di-σ bound to the Si dimers with the coordinating carbon atoms showing sp3 rehybridization.

Shimomura et al [59] in their PED analysis observed strong forward scattering near 0º and 90º in the [110] direction indicating that the C-C bond pairs of the adsorbate species are parallel to the Si-dimer bonds eliminating the TwB configuration as the dominant species. The R-factors

they obtained for the TB model were higher than those for the SB model and showed no improvement as the parameters were changed within reasonable ranges (~ ± 20% of bond lengths and ~ ± 30% of bond angles). Thus, their conclusion was that the SB configuration dominates on the Si(001) surface at room temperature.

While the time dependence of the binding state has been considered before this point, coverage dependence has not yet been discussed. Kim et al. [60] present evidence of the coverage dependant nature of benzene adsorption using ultraviolet high-resolution photoemission and UPS. Comparing the results for several exposures between 0 and 5L, they claim to have reconciled the apparent discrepancy between the results of the low coverage STM experiments and the saturated coverage spectroscopy experiments. They argue that the C 1s photoelectron spectrum is composed of two peaks; C_π and C_σ corresponding to the C-C double bonds and the C-Si σ bonds respectively; which, when measured at low coverage (0.1 L exposure), appear as a 1:2 C_π/C_σ ratio indicating the presence of a tetra-σ structure. As the coverage is increased the ratio changes until a 2:1 C_π/C_σ ratio is reached at the quasi-saturation coverage of 0.5 L. This ratio is consistent with the presence of the di-σ structure. The interpretation given here precludes the possibility of more than one species at this coverage.

Taguchi et al. [47] using TDS, present evidence of a single species at low coverage (0.006 L) resulting in a desorption peak at 500 K. As the coverage is increased, a second desorption peak at 460 K indicating a second species is observed. This peak is then shifted to 455 K for coverages beyond 1 L and the 500 K peak is shifted in the opposite direction to 505 K. In contrast to the findings of Kim and Witkowski, the peaks at 455 K and 505 K remain at a coverage of 24 L indicating the presence of two species.

Kong et al. [61] using NEXAFS evidence to support the presence of two species at saturation, concluded that the butterfly configuration is dominant at saturation but the presence of a second, less stable species, becomes significant on a longer timescale. This species takes the form of a tetra-σ-bonded structure. Lee et al. [62], on the other hand, argue that the TB species is the more stable configuration by 0.07 eV but also suggest that as the coverage is increased the conversion of the SB species to the TB species is blocked if the butterfly configuration is formed at a single dimer site between two TB benzenes. Thus they conclude that at saturation, the SB and TB configurations coexist.

In summary, the preponderance of research to date for the benzene/Si(001) system favours adsorption via the SB configuration which is, at low coverage, metastable in nature. This in turn results in conversion to the TB species over time. However, the adsorption energy of the TB species decreases with increased coverage giving rise to the possibility of stable SB adsorption for higher coverage systems. Whether or not this is accompanied by a second species in the form of the TB model is still in dispute.

The analysis to follow was undertaken with the aim of determining if any of the models presented in fig 5.3 could be eliminated as well as determining whether or not the evidence proposing a two species system can be substantiated.

5.2 Experimental Details

The Si(001) 0.5 mm thick wafer (P doped, 10 Ω cm) cleaved to a rectangle of 12 mm x 7 mm was cleaned *ex situ* by rinsing in methanol and ultra-pure water and mounted on the UHV manipulator with the capability for direct current heating and liquid helium cooling. The Si(001) was cleaned in situ under UHV conditions (< $5x10^{-10}$ mbar) by flashing the sample to 1280 ºC to yield a surface showing a well-ordered two-domain (2 x 1) LEED pattern at room temperature. The cleanliness of the sample was checked after each flashing cycle using XPS. At this stage the XPS was performed over a kinetic energy range of 0-700 eV at low magnification with a pass-energy of 50 eV.

The benzene was purified by freeze-pump-thaw cycles and was dosed at room temperature at an exposure of 5 L at a pressure 2 x 10^{-9} mbar ensuring saturation coverage of the surface. The purity of the benzene was checked using a quadrupole mass spectrometer.

After each dosing, XPS measurements of the uptake were carried out about the C 1s and Si2p peaks over respective kinetic energy ranges of 58-65 eV and 245-248 eV with a photon energy of 350 eV. The magnification was set to medium and the pass energy was set to 5 eV resulting in high resolution measurements. Fig.5.4 shows the C 1s XPS spectra for the uptake over an exposure range of 0.2 L to 5.0 L. Note the shift to the higher binding energy with increasing dosage (0.15 eV between 0.2 L and 5.0 L).

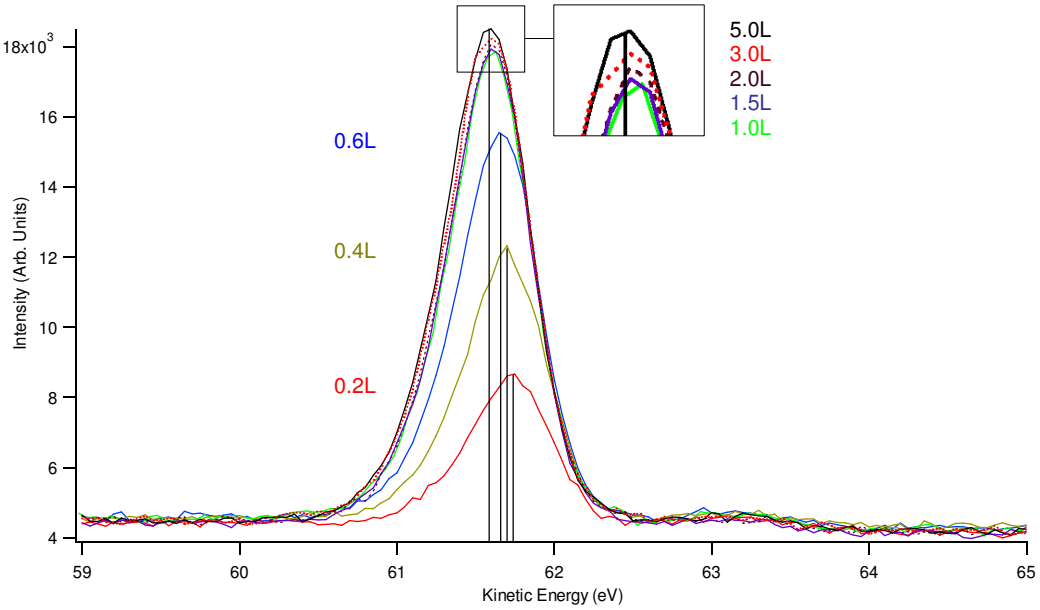

Fig. 5.4. XPS measured about the C 1s peak for different coverages (0.2 L to 5.0 L) with a photon energy of 350 eV.

Using the C 1s photoemission peak, scanned-energy mode PhD was performed at the angles tabulated in Table 5.1. The magnification was set to low and the pass energy to 20 eV. The PhD scans were measured over a kinetic energy range of 60-220.8 eV and consisted of 51 EDC's, each 10.8 eV wide and 3 eV apart at the emission angles shown in table 5.1. Although the measured C 1s peak is actually composed of two peaks, namely C_π and C_σ, it was not possible to unambiguously resolve them. Thus, the EDC's were integrated as single peaks yielding composite modulation functions containing the structural information for both species. Overlayers made up of configurations A through to F (fig.5.3) were modelled in the same way producing composite theoretical modulation functions.

θ φ	**0°** (normal emission)	**5°**	**10°**	**20°**	**30°**	**40°**	**50°**	**60°**
[$\bar{1}$00]	✓			✓		✓		✓
[$\bar{2}\bar{2}$50]			✓		✓		✓	
[$\bar{1}\bar{1}$0]		✓	✓					

Table.5.1. The polar (θ) and azimuthal (φ) angles at which the PhD scans were measured are indicated by the ticks. The spectra indicated by the red ticks where selected for analysis on the basis of modulation strength.

Si is a weak scatterer, the result of which is the observation of weak modulation functions. The emission angles indicated by the red ticks in table 5.1 represent those which produced modulations of sufficient strength for use in PhD. The azimuthal crystallographic directions listed in table 5.1 are shown in fig. 5.5. The polar angles are given with respect to the surface normal.

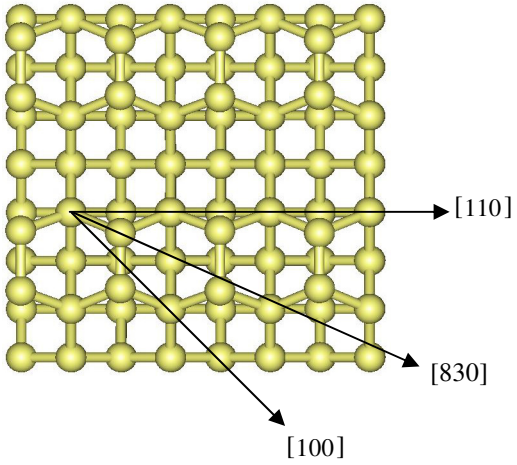

Fig. 5.5. Depiction of the azimuthal directions listed in table 5.1.

A 20º perspective view of the structure is presented in fig. 5.2 for clarity.

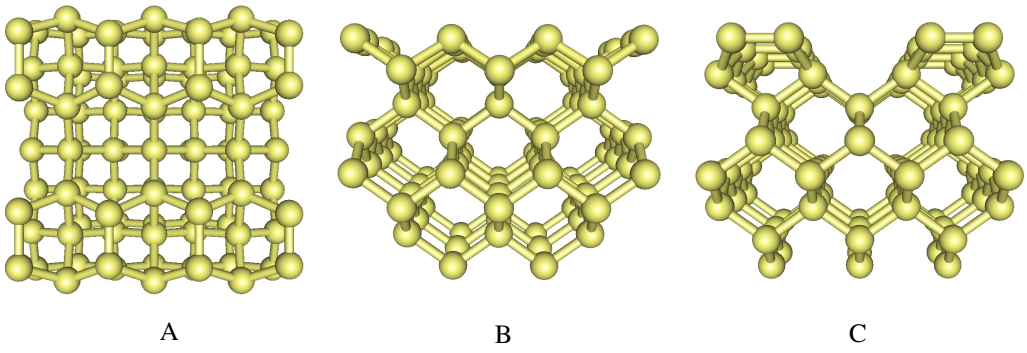

Fig. 5.6. 20º perspective views along the [001], [$1\,\bar{1}\,0$] and [110] directions corresponding to diagrams A, B and C, respectively.

5.3 Results and Discussion

Each of the models was first explored separately and will be discussed in turn beginning with the SB model. Subsequently a model including both the butterfly and TB structures will be discussed. All of the systems were modelled with a theoretical saturation coverage of 0.25 ML.

5.3.1 Standard Butterfly (SB)

The butterfly model is the most supported of all the models mentioned in this chapter. Consequently, there is a wealth of information detailing its structure including Si-C bond lengths, C-C bond lengths, and bond angles; the details of which are presented in table 5.2.

Ref.	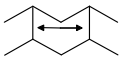 Si-Si Dimer Separation (Å)	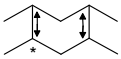 Si-Si Dimer (Å)	 (Å)	 (Å)	 (Å)		
STM [54]	3.36Å	2.39*	1.98	1.50	1.35		
STM [52]		2.38*	1.89	1.47-1.49	1.35		
TPD URUPS [49]				1.51	1.35	close to the ideal tetrahedron angle (109.5)	
Theoretical STM [9]				1.49-1.59	1.34-1.36	103° – 113°	119° – 122°
STM FTIR SQCC [48]		2.44*	1.89	1.49	1.35		
NEXAFS [61]							wing is tilted ~30º from surface plane.
PED [59]				1.3-1.6	1.3	85º– 115º	
DFT [57] MNDO/d LCGTO-DF		2.46* 2.35	1.97 1.94	1.51 1.53	1.35 1.36	109.9º 109.6º	119.2º 118.8º
Current Study	3.75	2.74* 2.30	1.93	1.47	1.38	83.1º	116.9º Wing tilted 42.0º from surface plane.

Table 5.2. Comparison of structural parameters for the butterfly structure presented in the literature and the current study. The * indicates the dimer involved in adsorption. The error limits of the current study will be discussed later.

The best achievable R-factor for the SB model, assuming the absence of any other species, was 0.2337 which, as will be seen later, is the lowest of all the models considered. This gives a var(R_{min}) value of 0.0695 meaning that any of the other models giving an R-factor greater than 0.3031 can be excluded. The structure of this model is presented graphically in fig.5.6.

While structural parameters such as the Si-C, C-C, and C=C bond lengths are in good agreement with those detailed in previous studies, structural details such as the bond angles and Si-Si displacements are less concurrent. This may in part be due to the fact that PhD is more sensitive to the distance between the emitting atom and the nearest neighbour scattering atom than it is to the direction of their connecting axis. The error limits for these parameters have been omitted because the single species SB model does not represent the final optimised structure rendering them irrelevant. However a more detailed discussion about this structure will be reserved until later (section 5.3.7).

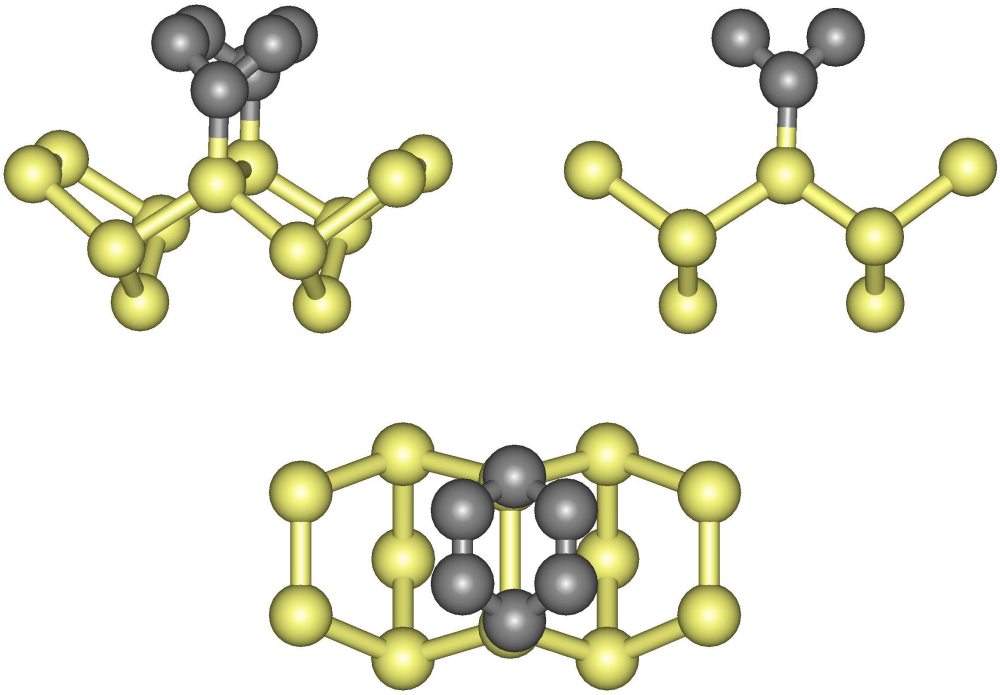

Fig. 5.6. A graphical representation of the butterfly model produced in the current study. Note that the results here differ significantly from those produced when the TB species is modelled along with the butterfly species.

5.3.2 Tilted (T)

The tilted configuration finds far less support in the literature than the butterfly model and is explored in this work for the sake of completeness.

Borovsky et al. [51], the main proponents of the tilted model, provide no structural detail other than that implied by the name. This is left to a later paper by Wolko et al. [52] who in fact rejected the tilted model as a likely candidate in favour of the TB model as the binding adsorption state.

Ref.	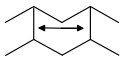 (Å)	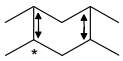 (Å)	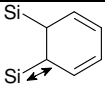 (Å)	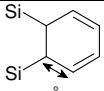 (Å)	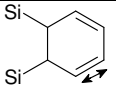 (Å)	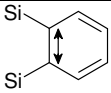 (Å)
STM [52]		*2.39	1.89	1.47-1.49	1.35	1.47-1.49
Current Study	3.84	2.96* 2.40	1.85	1.52	1.51	1.55 Tilted by 39.8° from the surface plane

Table 5.3. A comparison between the literature data [52] for the tilted species and that produced in the current study.

The best achievable R-factor for the tilted model (graphically represented in fig.5.7) was 0.6268 and consequently has been dismissed as a possible candidate.

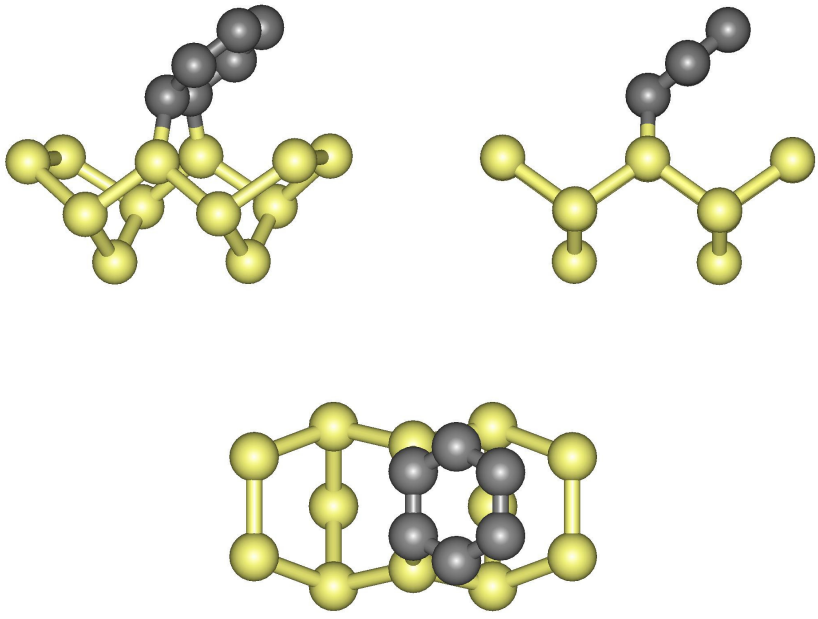

Fig. 5.7. A graphical representation of the tilted model produced in the current study.

5.3.3 Tight Bridge (TB)

The TB model on the other hand produced an R-factor of 0.2641, the details of which are tabulated in table 5.4 and represented graphically in fig. 5.8. This lies within the variance for the SB model and is significantly better than that for the tilted model and all of the other single species models considered in this work with the exception of the SB model.

Ref.	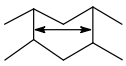 (Å)	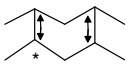 (Å)	 (Å)	 (Å)	 (Å)		
STM DFT [53]	3.36	2.35*	2.0	1.35	1.57		
STM DFT [52]			1.87-1.89	1.35	1.47-1.53		
Theoretical STM [9]				1.34-1.36	1.49-1.59	119° –122°	103° –113°
Current Study	2.80	2.24* 2.34	1.47 1.86	1.52	145 1.59	116.0º	107.6º Wing tilted 49.2º from the surface plane

Table 5.4. A comparison between the literature data for the TB species and that produced in the current study. The * indicates the dimer below the C-C bond.

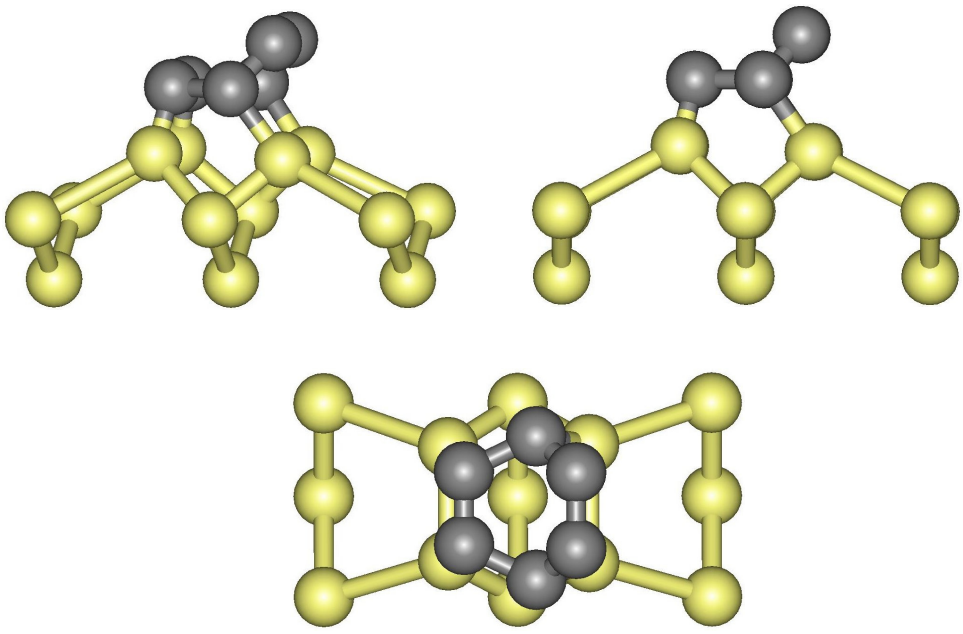

Fig.5.8. A graphical representation of the TB model produced in the current study.

The Si-Si dimer separation is significantly less than that proposed by Hofer et al. [53] and consequently results in two of the Si-C bonds being reduced to 1.47 Å. The C=C double bond is longer than that predicted by previous studies by about 13%. This is nearer to the standard C-C bond length of 1.54 Å than it is to the standard C=C double bond (1.34 Å) [63]. The C-C single bonds fall within the values proposed in the literature. The C-C-C bond angle also falls outside the range proposed by Silvestrelli et al. [9] but only by 2.5% while the C=C-C bond angle falls within the suggested range. The low R-factor suggests that the TB species is likely to be present. However as mentioned earlier, the C_π and C_σ peaks could not be definitively resolved for the purposes of this determination and the integrations are a composite of the C_π and C_σ signals. Furthermore, if more than one species is present the resulting integrations are a composite of the C_π and C_σ signals for all species which is further complicated by the possibility of different adsorbate ratios. If a model is analysed with the assumption that no other species are present when in reality two species exist, the finer structural details will become distorted. The TB structure analysed with the inclusion of the SB model will be discussed in section 5.3.7.

5.3.4 Pedestal (P)

The pedestal configuration, like the tilted model is relatively unsupported in the literature but again, has been considered for the sake of completeness. The structural details of the optimised pedestal model are detailed in table 5.5 and graphically represented in fig. 5.9.

Ref.	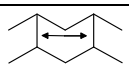 (Å)	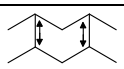 (Å)	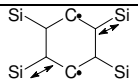 (Å)	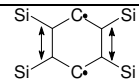 (Å)	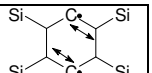 (Å)
semi-empirical PM3 [56]			1.98 – 2.12	1.51	1.45
STM [52]				1.56	1.43
Current Study	3.84	2.34	1.95 – 2.23	1.30	1.44

Table 5.5. Comparison of structural parameters for the P structure presented in the literature and the current study. The dot on C• indicates the presence of a radical centre [9, 48, 52], although this need not necessarily be a radical but rather represent electronic delocalization preserving some of the aromaticity of the benzene.

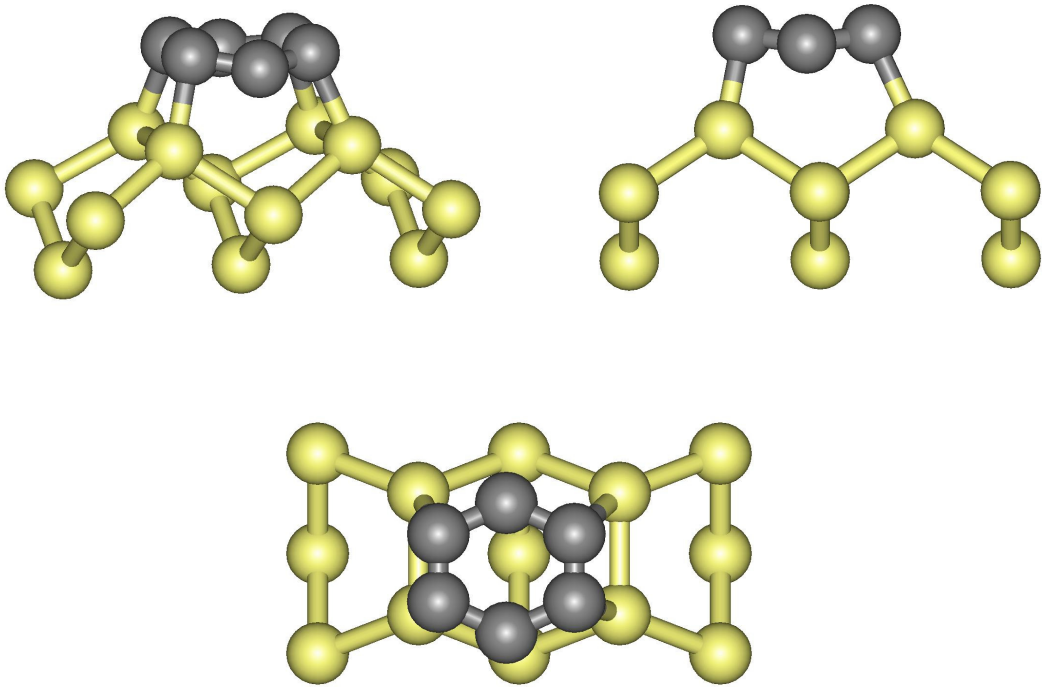

Fig. 5.9. A graphical representation of the pedestal model produced in the current study.

Optimisation revealed a structure asymmetrically located across the two Si dimers. The C-C bond lengths were found to be significantly shorter than expected. The C-C• bond lengths, on the other hand, lie between those suggested by Jeong [56] and Wolkow [52]. This model produced an R-factor 0.4722 and has consequently been dismissed as a possible candidate based on the R-factor and var(R_{min}) value obtained for the SB model of 0.3031.

5.3.5 Twisted Bridge (TwB)

While it has been proposed that TwB species occur only at type-C defects [52][53], there is some controversy regarding the structure of these defects. The type-C defect as defined by Hamers and Köhler [64] appears as a pair of missing Si atoms that are neighbouring along a dimer row. According to Wolko on the other hand, the type-C defect can be described as two otherwise normal Si dimers that have a parallel buckled geometry as a result of a subsurface structural anomaly, typically occurring at the ~1% level [52]. This interpretation is consistent with the possibility of TwB adsorption and so the model analysed here is based on that

proposed by Wolko et al. The optimised structural parameters are again, detailed in table 5.6 and graphically represented in fig. 5.10.

Ref.	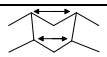 Si-Si Dimer Separation	 Si-Si	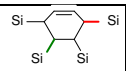 (Å)	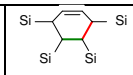 (Å)	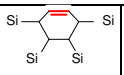 (Å)	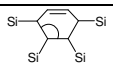	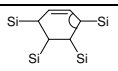	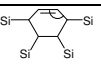
STM [52]			1.87 – 1.89	1.47 – 1.53	1.35			
Current study	3.43 3.12	2.24	1.55 2.08	1.48 1.58	1.44	113.6°	116.1°	115.3° Wing tilted 41.1° from surface plane

Table 5.6. Comparison of structural parameters for the TwB structure presented in the literature and the current study.

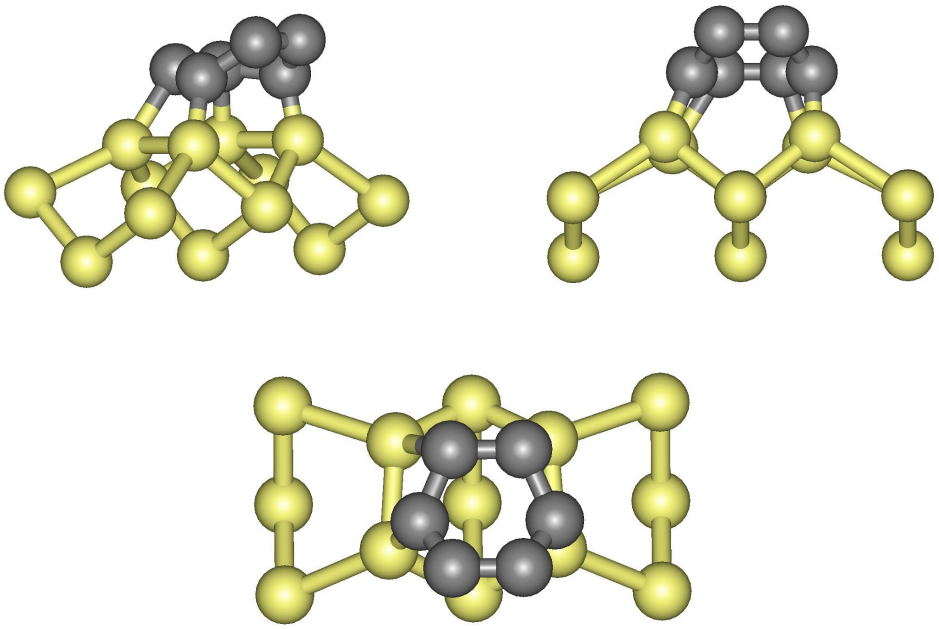

Fig. 5.10. A graphical representation of the TwB model produced in the current study.

A high final R-factor of 0.4506 was obtained making the TwB model an unlikely candidate as the dominant species. This however does not necessarily mean that no TwB species occur; merely that the occurrence of type C defects is low and the contributing signal from any possible TwB adsorbates is swamped by that from the dominant species.

5.3.6 Diagonal Bridge Butterfly (DBB)

The optimised DDB model produced an R-factor of 0.3504. The structural details of which are included in table 5.7 and graphically represented in fig.5.11.

Ref.	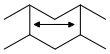 Si-Si Dimer Separation (Å)	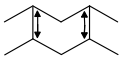 Si-Si Dimer BL (Å)	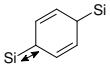 (Å)	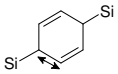 (Å)	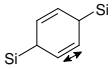 (Å)	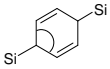 (Å)	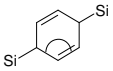 (Å)
MD [9]				1.49 – 1.59	1.34 – 1.36	103° - 113°	119° - 122°
Current Study	2.20	2.20	1.77	1.53	1.45	83.8°	114.6° Wings tilted 51.0° from the surface plane

Table 5.7. Comparison of structural parameters for the DBB structure presented in the literature and the current study.

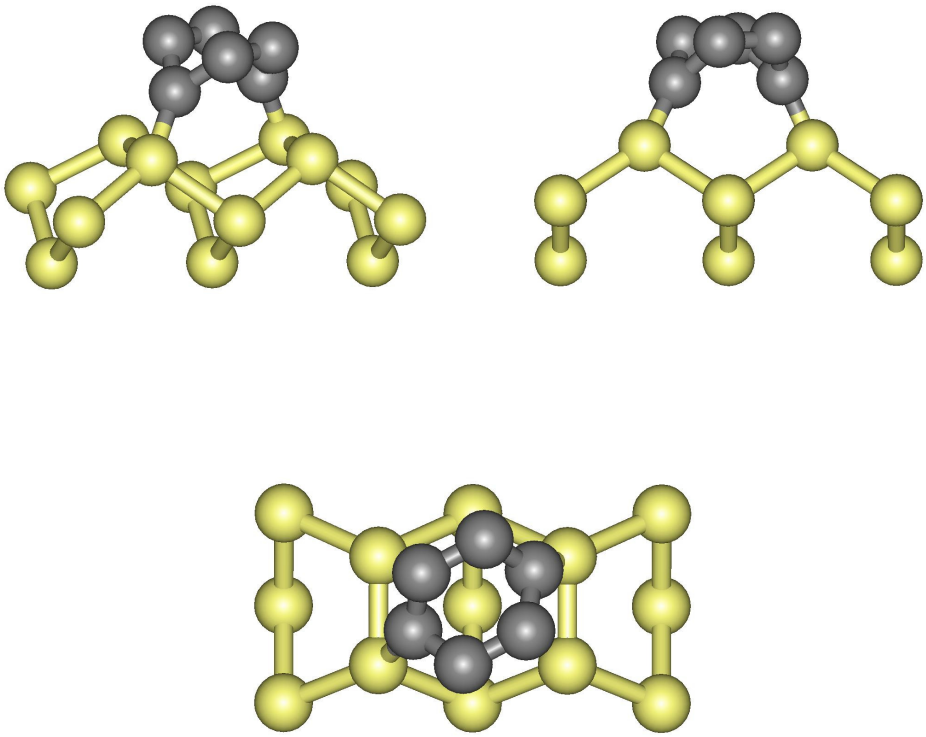

Fig. 5.11. A graphical representation of the DDB model produced in the current study.

The R-factor is above the variance calculated for the SB model and consequently this model has been abandoned as a likely candidate. The TDDB model was considered by including a

tilting parameter in the optimisation procedure for the DDB model allowing the wings to be tilted up and down independently. This however yielded no improvement in the R-factor.

5.3.7 Combined SB and TB

As mentioned in section 5.1.4, Kim et al. [60] propose an evolution of the C_π/C_σ ratio from 1:2 to 2:1 over a coverage range of 0.1 L – 5 L indicating the decrease of a tetra-σ and the increase of the di-σ species. However, the XPS analysis of 1,3-cyclohexadiene and 1,4-cyclohexadiene adsorbed on Si(111) undertaken by Tao et al. [65] casts doubt on the validity of these results. According to Tao, the C bonded to Si has a C_σ binding energy of 283.8 eV which is consistent with Kim's data (283.9 eV), however, the C_π has a binding energy of 285.0 eV which is significantly different from that proposed by Kim (284.2 eV). If the system consisted solely of the SB species a maximum at 285.0 eV would be expected; therefore a maximum at 284.2 represents a mixture of SB and TB species which is consistent with the findings of Taguchi et al. [47] and Kong et al. [61].

Using the structural parameters from the separately optimised SB and TB models a combined model was analysed using PhD. This model consisted of separate SB and TB domains. The percentage composition of the SB and TB domains was then allowed to vary. Fig. 5.12 shows the variance graph for the percentage of SB in an SB/TB overlayer at a coverage of 0.25 ML. A minimum is observed at a composition of 58% with a variance of ± 35% which leaves considerable room for interpretation. However, the presence of more than one species is strongly favoured. A possible reason for this uncertainty is that the duration of the PhD experiment (two hours) is large compared with time constant associated with the SB to TB conversion (19 - 25 min).

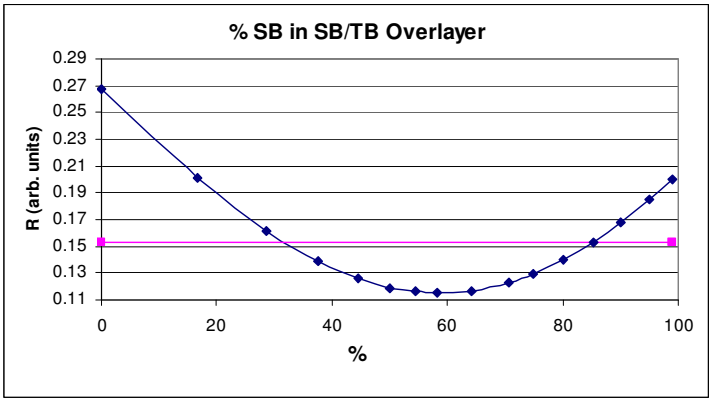

Fig. 5.12. % SB in SB/TB adsorption layer as determined by PhD at a coverage of 0.25 ML giving a minimum value of 58% ± 27%.

The structural parameters were then re-optimized at this composition giving an R-factor of 0.1183 and a var(R_{min}) value of 0.0351. Since the R-factors for the single SB and TB models are above 0.1534, they can be excluded leading to the conclusion that both SB and TB species are present in the monolayer at saturation coverage. With the notable exceptions of the SB wing tilt and the TB C=C bond length which will be discussed later, most of the structural parameters showed little change.

In running the above simulations for the mixed layer, the surface was taken to consist of separate SB and TB domains in different proportions. Since the optimum relative composition was found to be close to 1:1 it was decided to investigate domains containing both SB and TB species in equal proportions.

Three other overlayer configurations were considered in which a 1:1 SB/TB ratio was assumed. These are shown in fig. 5.13.

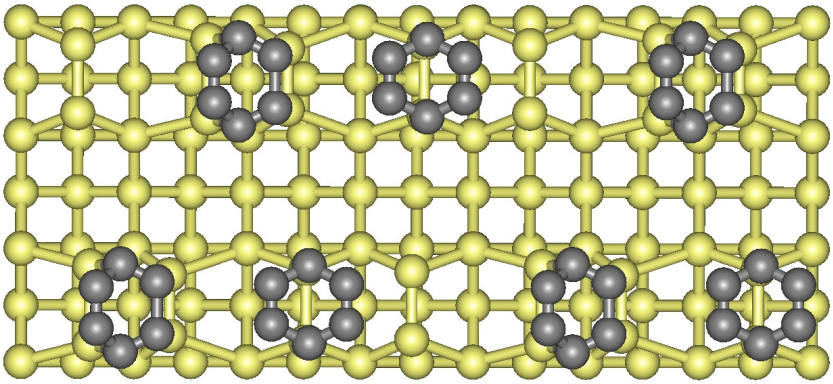

A

R-factor 0.1179

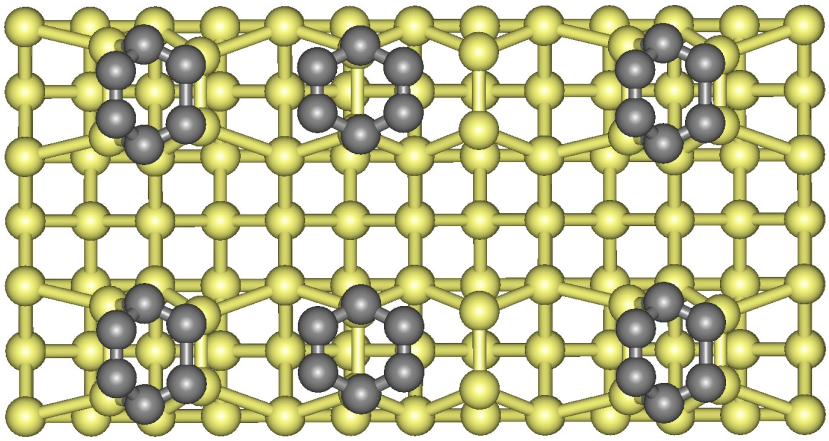

B

R-factor 0.1183

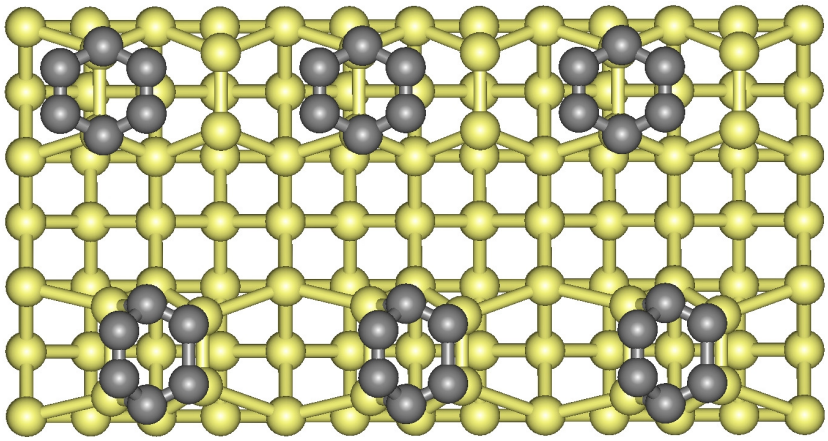

C

R-factor 0.1231

Fig. 5.13 Alternative overlayer configurations. A consists of SB and TB strips in the $[\bar{1}30]$ direction alternating in the $[110]$ direction, B consists of SB and TB strips in the $[\bar{1}10]$ direction alternating in the $[110]$ direction and C consists of SB and TB strips in the $[110]$ direction alternating in the $[\bar{1}10]$ direction.

These all result in virtually identical R-factors and re-optimization yielded no improvement meaning that, while PhD is clearly sensitive to the presence of two species, it is not sensitive to which species neighbours which.

Lee et al. [62] in their DFT study of benzene adsorption on Si(001) propose that the TB species is more stable than the SB species by 0.07 eV which is in good agreement with the findings of Silvestrelli et al. [9] who propose a stability difference of 0.06 eV in favour of the TB species. In the absence of any steric hindrance these relative stabilities should correspond to TB/SB overlayers consisting of 93% and 90% TB adsorbates, both of these values lie marginally out side the variance of the current PhD analysis. However, there is a real steric factor which must be considered. As Lee points out, when two TB species have formed as a result of falling over towards a central SB species, the central SB species is no longer able to fall over (see fig. 5.14).

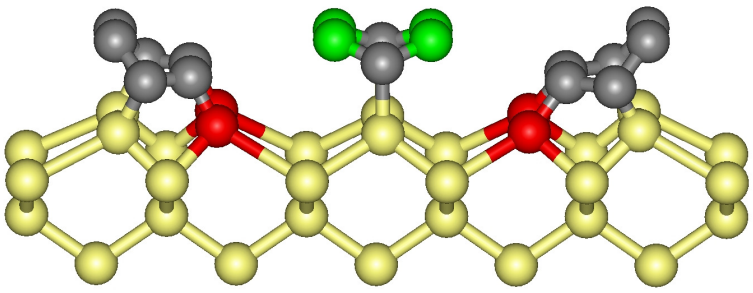

Fig. 5.14 Diagram of a sterically hindered SB species. The SB species can no longer fall over because the Si atoms coloured red are no longer available to react with the C atoms coloured green.

Using a basic Monte Carlo type simulation, on a cluster of 13 x 13 SB adsorbates, in which the adsorbates were allowed to fall left or right in a random fashion, a situation arose in which about a third of the SB adsorbates remained due the above mentioned steric constraint. While this is a very simplistic model because no resulting intermolecular forces are considered, it does provide a plausible argument for a higher concentration of the SB species than that suggested by the relative stabilities alone.

The modulation functions for the combined model (separate domains) are presented in fig. 5.15.

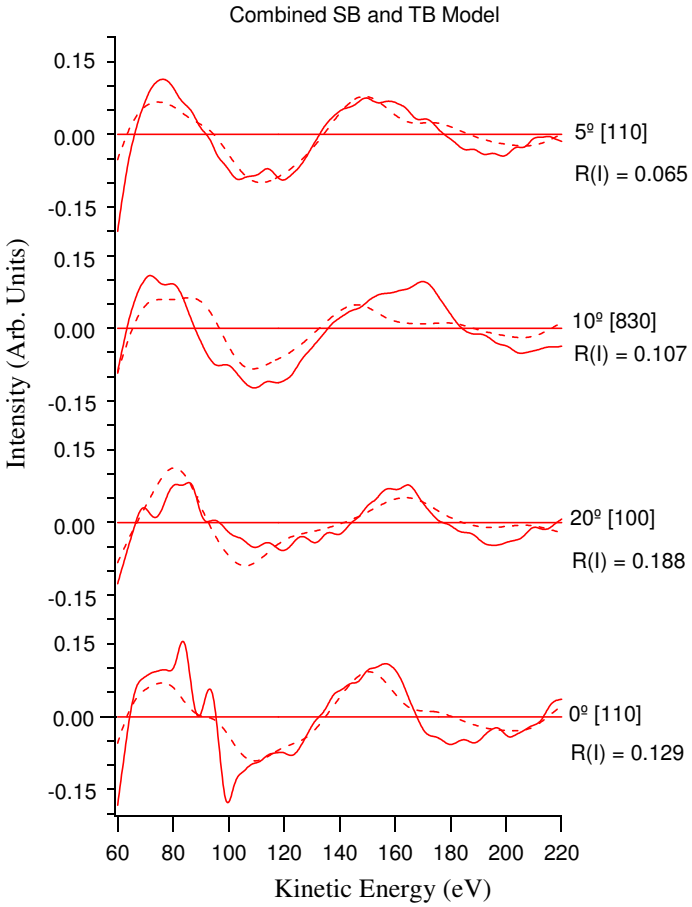

Fig. 5.15. Modulation functions for the combined SB and TB model with a composition of 58% SB and 43% TB.

The final structural details as determined from the combined model are compared with their counterpart single species models in table 5.8 and graphically represented in figs. 5.16 and 5.17.

SB	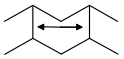 Si-Si Dimer Separation (Å)	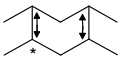 Si-Si Dimer (Å)	 (Å)	 (Å)	 (Å)			Wing Tilt
Combined Model	**3.59**	**2.45*** 2.30	1.93	1.47	1.35	120.5°	115.9°	**15.3°**
Modelled Separately	**3.75**	**2.74*** 2.30	1.93	1.47	1.38	83.1°	116.9°	**42°**
TB	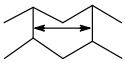 (Å)	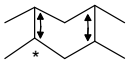 (Å)	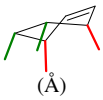 (Å)	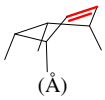 (Å)	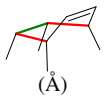 (Å)		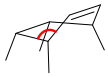	
Combined Model	2.71	**2.06* 2.65**	1.47 1.88	**1.40**	**1.76** 1.38	116.0°	105.5°	47.1°
Modelled Separately	2.80	**2.24* 2.34**	1.47 1.86	**1.52**	**1.45** 1.59	116.0°	107.6°	49.2°

Table 5.8. Comparison of separate and combined model parameters. Parameters which have changed significantly are emboldened. The error bars for each species will be given in table 5.10.

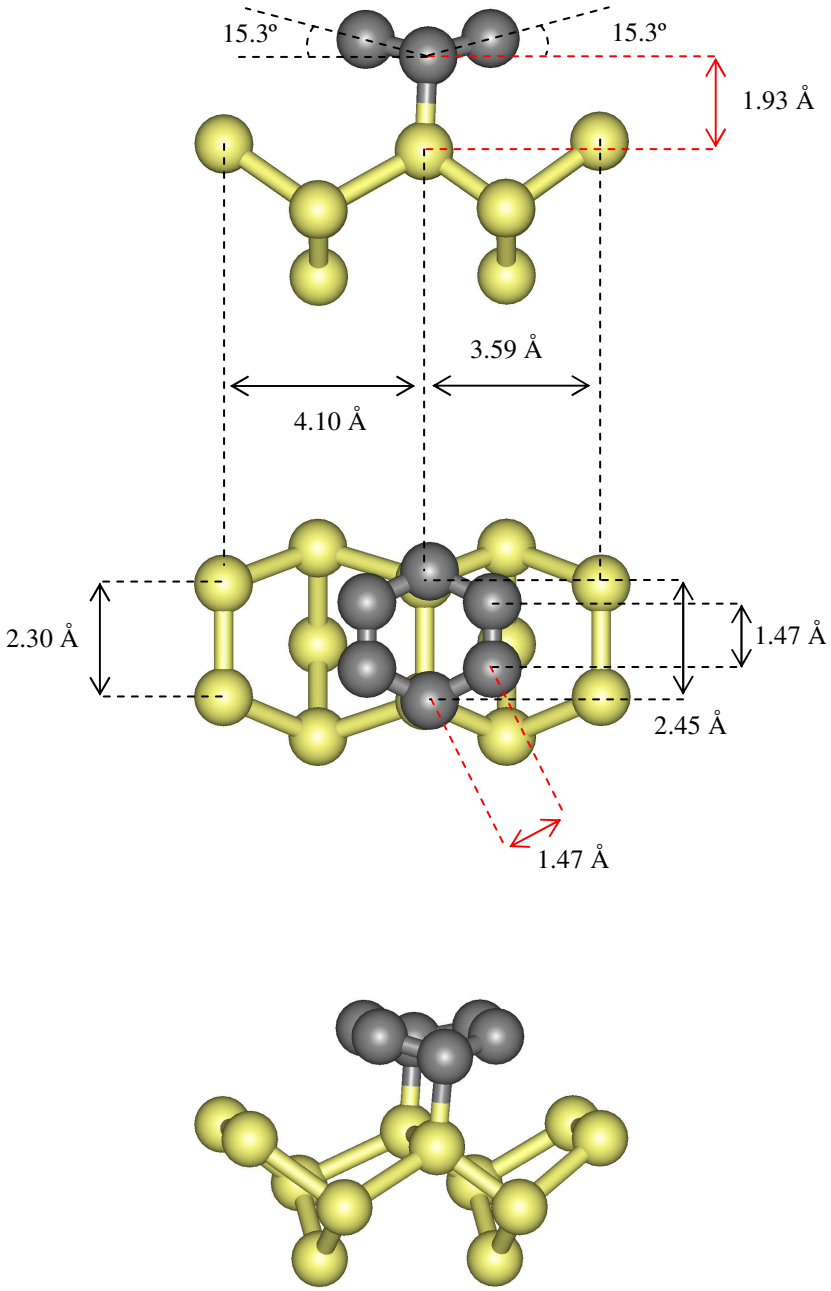

Fig 5.16. A graphical representation of the SB model produced from the combined SB/TB model. The black arrows represent distances in the plane of the page; those distances which are not in the plane of the page are represented by red arrows.

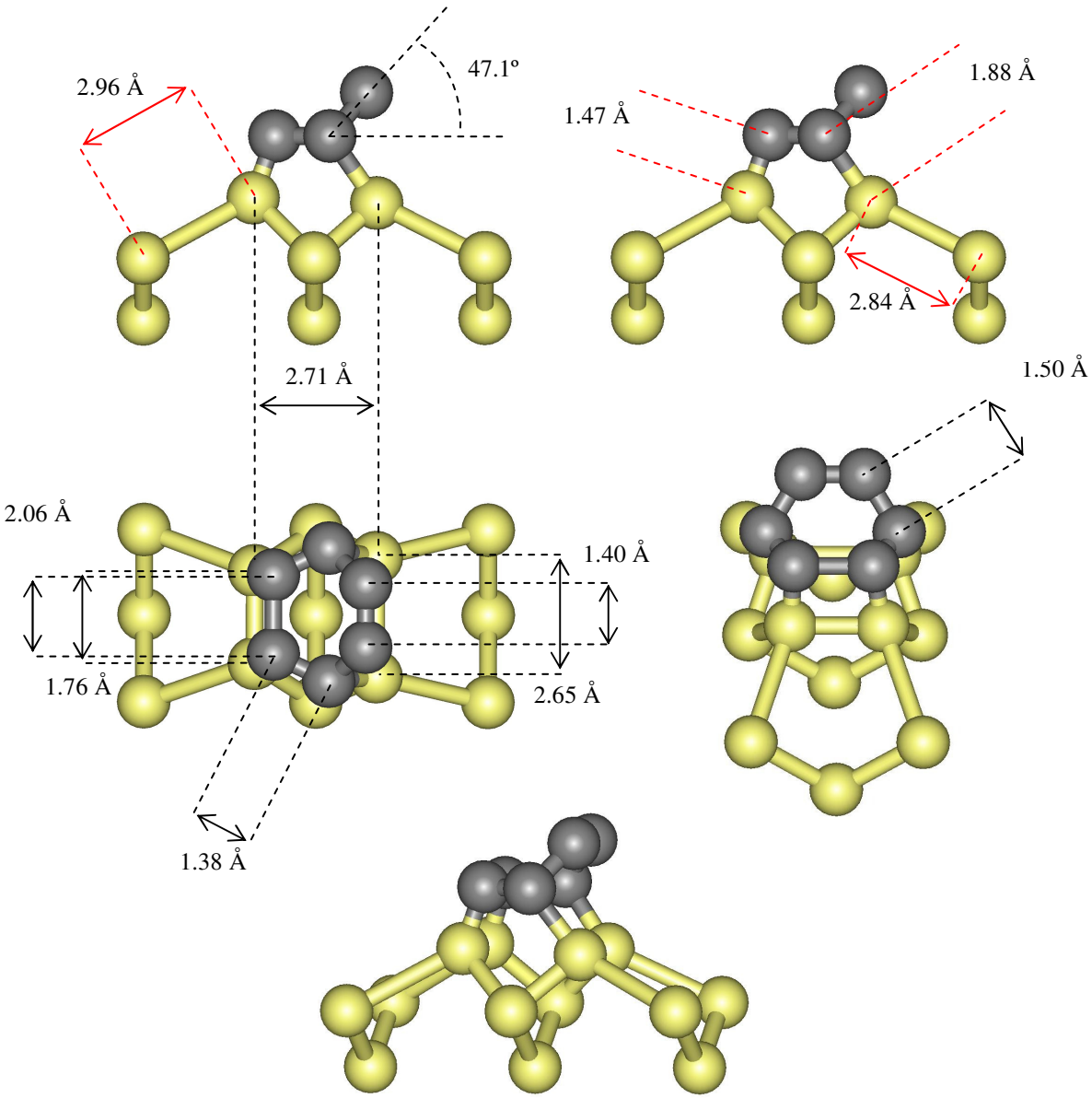

Fig 5.17. A graphical representation of the TB model produced from the combined SB/TB model. Again the black arrows represent distances in the plane of the page; those distances which are not in the plane of the page are represented by red arrows.

The optimised SB structure produced in the combined model differs from that produced in the single species model mainly in the tilt of the butterfly wings (compare figs. 5.6 and 5.15). The structure was defined in such a way as to allow the tilt of the wings to be altered without changing the C-C or C=C bond lengths and allowing the C-C or C=C bond lengths to vary without changing the wing tilt. Fig. 5.18 shows how the wing tilt varies in relation to θ for both the combined and separate models. A clear minimum for the combined model is found at a value of θ = 79.2° + 3.0/– 2.7 corresponding to a tilt of 15.3° +4.1/-4.2 from the surface plane. This indicates a much flatter configuration than that suggested by the separate model which resulted in a tilt angle of 42° from the surface plane. One explanation which could naively be given for this is that if a second species is present but not accounted for the optimised structural model would be, to some extent, a superposition of the structural data for both, meaning that in this case, the tilt in the SB wing is borrowed from the tilted wing of the unaccounted for TB species. A value somewhere between 15.3° and the tilt of the TB wing of 49.7° could be expected, which is what is observed. However, if this reasoning were correct the same would apply to the TB model but the separately optimised TB model suggests a tilt of 49.9°. While it is clear that discounting the presence of a second species influences the optimization process, or for that matter, assuming a second one is present when it is not, the extent of this influence is complex.

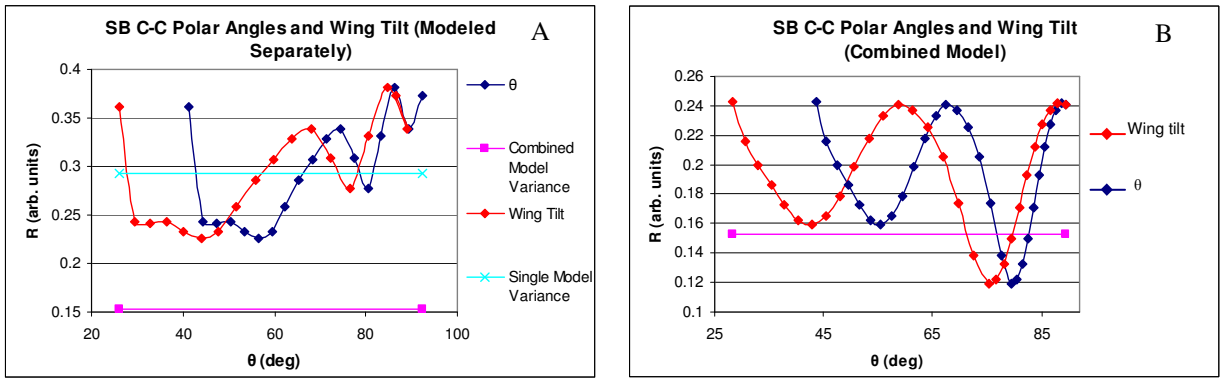

Fig. 5.18. Relationship between θ and wing tilt for the SB configuration. Graph A represents θ and wing tilt when modelled separately. Graph B represents θ and wing tilt in the combined model.

A more simplistic explanation is that the variance of the separately optimised SB model is too high to distinguish between the minimum found at 43.9 (46.1° from the surface plane) and a separate minimum found at 76.5° (13.5° from the surface plane) which is much closer to that obtained in the combined model. Furthermore, the tilt of 15.3° falls within the range suggested by Silvestrelli et al. [9] of 10.4 – 26.5 derived from the internal angles presented in table 5.2.

Although, it must be noted that these values are for a low coverage system. While the tilt suggested by Kong et al. [61] of ~30º appears to fall outside the error limits of the current study, this cannot be stated with certainty because no indication of the error limits of their results is given.

Another difference in the SB models is evident in the C=C bond lengths of 1.35 +0.15/-0.45 Å and 1.38 Å for the combined and separately optimised models respectively. However, this is a small difference and is well within the error limits of the final optimisation which, for this parameter, is in good agreement with previous studies.

The combined and separate SB models show marked differences in the dimer bond lengths involved in adsorption, but before this is discussed further, an explanation of the various optimised parameters will be given.

The optimised SB and TB structural parameters and their variance limits are presented in table 5.10.

SB		Corresponding Graph Fig. 5.17	TB		Corresponding Graph Fig. 5.18
Si-C Bond Length	1.93 ± 0.03 Å	A	Si-C Bond Length	1.85 + 0.10/– 0.15 Å	A
Si–C θ	13° + 13°/–38°	B	Si-C θ	49.2° + 1.9°/– 3.7°	B
Si–C φ	–1.5° + 9.4°/– 6.9°	C	Si-C φ	– 7.5° + 10.0°/–7.4°	C
C–C Bond Length	1.47 + 0.36/– 0.11 Å	D	C–C Bond Length (horizontal)	1.37 + 0.47/– 0.29 Å	G
C–C θ	79.5° + 3.0°/– 2.7°	E	C–C θ (horizontal)	90.0° ± 2.14°	H
C–C φ	25.9° + 5.3°/– 6.2°	F	C–C φ (horizontal)	26.0° + 26.8°/– 22.3°	I
C=C	1.35 + 0.15/– 0.45 Å	I	C–C Bond Length (tilted)	1.50 + 0.16/– 0.12 Å	D
Si-Si* displacement	0.76 ± 0.21 Å (θ = 102.8 φ = 70.13)	G	C–C θ (tilted)	55.5° + 5.2°/– 12.9°	E
Si-Si displacement	0.77 + 0.57 /– 2.05 Å (θ = 90 φ = 90) Insensitive to physically reasonable displacements.	H	C–C φ (tilted)	31.5° + 8.1°/– 11.5°	G
			C=C	1.40 Å (Indirect – depends on tilted C-$C_{(\text{bond length}, \theta, \varphi)}$)	
			Si–Si* displacement (θ = 99.3 φ = 45.9)	0.83 + 0.25/– 0.24 Å	J
			Si–Si displacement (θ = 90.0 φ = 58.0)	1.05 + 0.40/– 0.26 Å	K

Table 5.10. Optimised structural parameters for the SB and TB combined model.

With the exception of the bond lengths, these parameters do not correspond directly to those detailed in table 5.9 but they are the parameters which were varied in the simulation program from which the tabulated parameters are calculated. For example the bond angles C-C(Si)-C and C(Si)-C-C in the SB and TB models are compositions of the $\theta_{C\text{-}C}$ and $\varphi_{C\text{-}C}$. Similarly, the Si-Si* and Si-Si displacements are a composition of the respective $x_{Si_{(ideal)}-Si}$, $\theta_{Si_{(ideal)}-Si}$ and $\varphi_{Si_{(ideal)}-Si}$ parameters where x is the distance between the position of the dangling Si atom if the bulk structure were ideally truncated, and the experimentally determined Si position.

The variance graphs for the SB parameters detailed in table 5.10 are presented in fig. 5.19, A – I. Note that the dramatic increase in the R-factors in graph H is due to excessive displacements resulting in the superposition of the dimer Si atoms. In essence, PhD is insensitive to this parameter within a physically reasonable range. Which is to be expected due to the distance of the spectator dimer from the emitting C atoms.

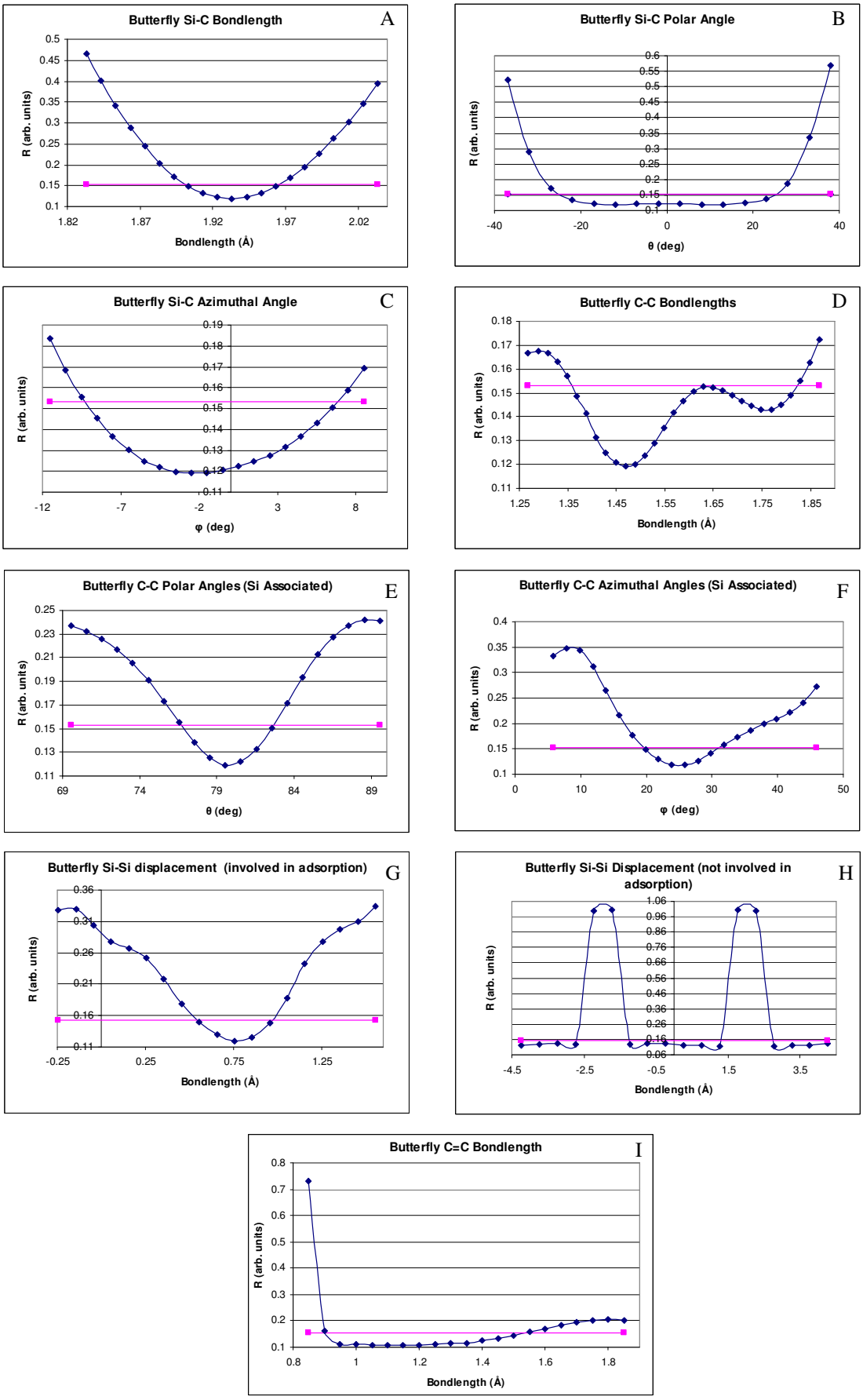

Fig. 5.19. Variance graphs for the SB species in the combined SB/TB model. Note that the sudden change in R-factor in H is due to unphysical displacements resulting in the superposition of the dimer Si atoms.

The variance graphs for the TB parameters detailed in table 5.10 are presented in fig. 5.20, A – K (extending over to the next page).

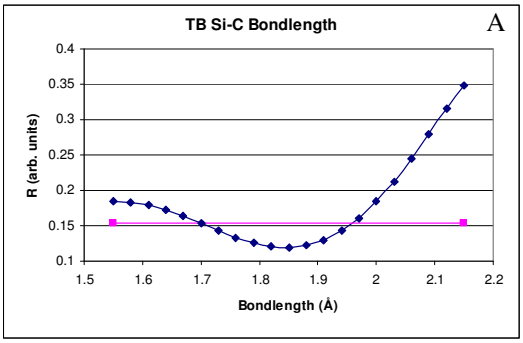

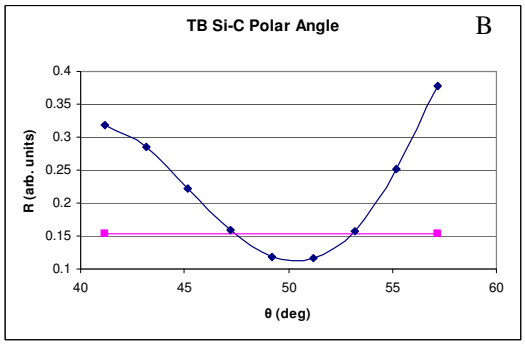

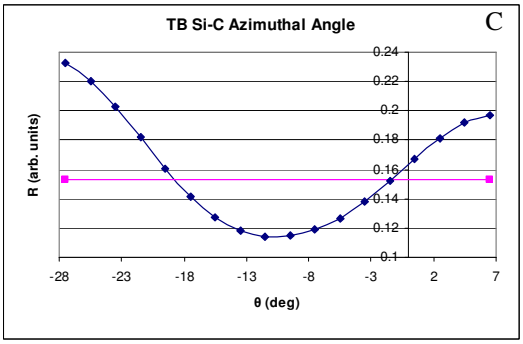

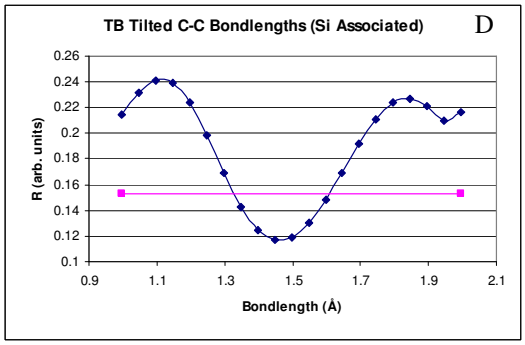

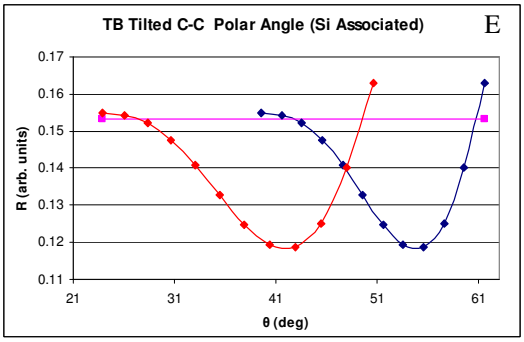

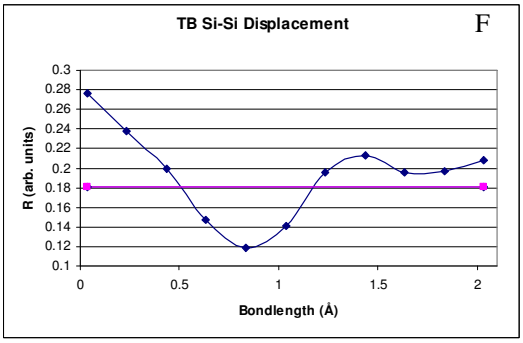

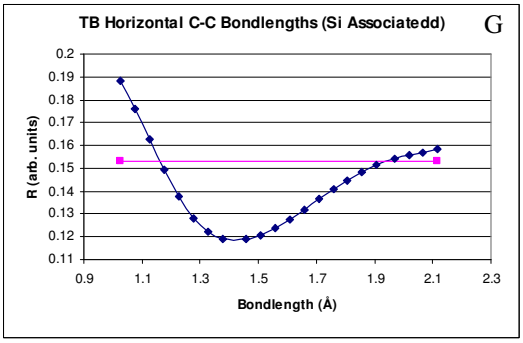

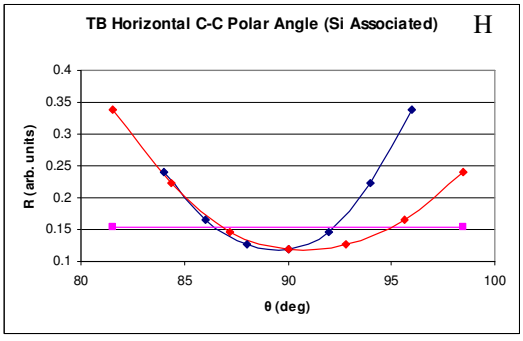

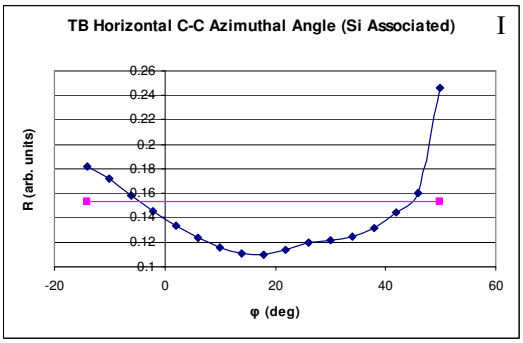

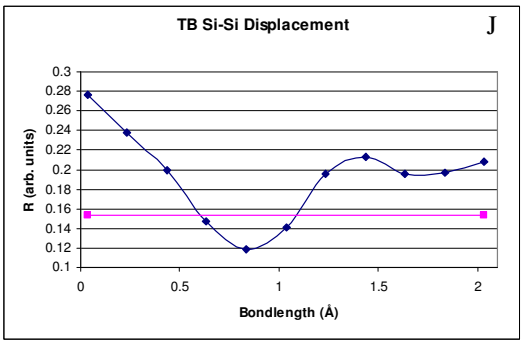

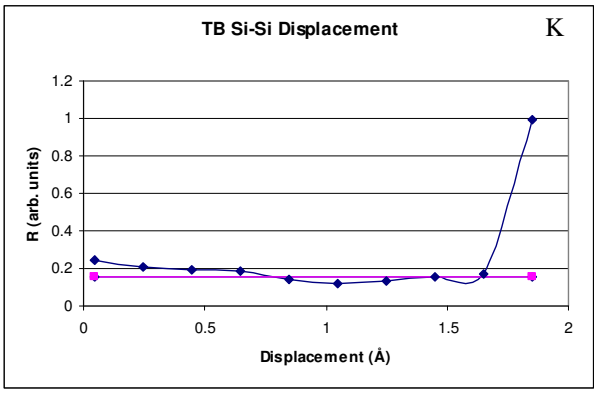

Fig. 5.20. Variance graphs for the TB species in the combined SB/TB model. Graphs E and H show both θ and wing tilt in blue and red respectively.

As shown in table 5.10, the dimer bond lengths are measured indirectly. In the case of the dimer directly involved in SB adsorption in the combined model (now denoted SB_c^* while SB_s^* will be used for the same dimer in the separately optimised model where the subscripts c and s stand for combined and separate), its length can easily be derived giving a value of 2.45 ± 0.38 Å, which is in good agreement with previous studies. The difference of 0.29 Å between SB_c^* and SB_s^* (2.74 Å) falls within the variance.

The discrepancy in dimer separation is more pronounced with a high value of 3.75 Å for the SB_s model compared with a value of 3.59 Å ± 0.7 for the SB_c model. This is likely influenced by the considerable distortion resulting from the unaccounted for TB structure; however, the non-trivial nature of this influence has been mentioned already.

In contrast to the dimer separation of 3.36 Å suggested by Hofer et al. [54], 3.59 ± 0.7 Å seems a bit high. Although an important point is that their study is for a low coverage system. The difference in dimer separation might be a real result of an increased symmetry about the SB_c^* dimer arising from a more ordered overlayer. Credibility is given to this by the fact that the occurrence of any dimer separation less than 3.84 Å for the SB structure shows that the dimer separation is sensitive to neighbouring adsorbates. The Si-C, C-C, and C=C bond lengths are all in excellent agreement with previous studies for the SB model.

While the TB model is accompanied by more extreme distortions than the SB model the structural parameters are, for the most part, consistent with those presented in previous work. For example the C-C bond lengths of 1.37 +0.47/-0.29 Å and 1.50 +0.16/-0.12 Å for the horizontal and tilted bonds respectively fall within the range of C-C bond lengths proposed in the literature [9,52,53] (1.36-1.50 Å) when the variance is considered. The C=C bond length of 1.40 Å is significantly higher than might be expected in the light of previous studies but the difference falls well within the error limits of the current analysis. The tilt of the TB wing is found to be 49.7º which is in the range of 21º-53º proposed by Silvestrelli et al. [9] (derived from their results). The Si-C bond length of 1.85 +0.10/-0.15 Å is in good agreement with Wolkow et al. [52] but the Si-C* bond length is significantly lower. This may be a result of the constraints imposed by the structural definition meaning only the Si-C or the Si-C* bond lengths can be properly optimised as bond lengths in a given model the others are merely optimised in terms of the relative positions of the Si atoms. The sensitivity of PhD to bond lengths over its sensitivity to bond angles and lateral displacements has been mentioned already and will be discussed further in the following chapter but suffice it to say that when the Si-C* bond length is optimised in term of relative positions it is optimised using the more limited capabilities of PhD. A similar point can be made for the extreme distortion of the dimer bond lengths and separation.

5.4 Conclusion

The analysis of C_6H_6 adsorption is difficult due the degree of coupling amongst the structural parameters. In the case of CO adsorption on Pt(111) altering the C≡O bond length had relatively little effect on any of the other structural parameters. In this case however, altering the C=C bond length, for example, effects the Si-C bonding geometry. In fact altering any of the structural parameters will have an influence on the other structural parameters. Furthermore, referring back to table 5.8, the change in the optimized structural data as a result of the inclusion of a second species shows that the parameter coupling extends beyond the intramolecular parameters of the adsorbate to the intermolecular parameters of the entire adsorption/substrate system.

Despite these difficulties, the final results are in reasonable agreement with previous studies. Most significantly, the formation of a single species adsorbate/substrate system has been eliminated achieving a minimum R-factor of 0.2337. Additionally, the T, TwB, P, TDBB and

DBB models have been dismissed on the basis of their high R-factors of 0.6268, 0.4506, 0.4722, 0.3504 and > 0.3504 respectively. The combined TB/SB model is clearly distinguished from all of the other models by an exceptionally low R-factor of 0.1183. In general, the optimised SB and TB structures in the combined model are in good agreement with previous studies especially with regard to the directly optimised bond lengths. Parameters involving more lateral displacements are less convincing on consideration of their limits; something that might be remedied in future work through the use of vertically polarized radiation which will be discussed in the following chapter.

6 The Use of Vertically Polarized Radiation in PhD

6.1 Introduction

Currently PhD is performed with a suitable channeltron detector positioned in the polarization plane of the incident synchrotron radiation. This results in both the directly emitted and scattered components being detected. The advantage of this approach is that the directly emitted component provides a fixed reference wave with which the scattered wave interferes, meaning that a somewhat intuitive interpretation of the modulations can be given (refer to the beginning of section 4.4). Another advantage is that the signal to noise ratio is high. A disadvantage however, is that the directly emitted photoelectron component is dominant, drowning out to a significant extent, the structurally rich information contained in the scattered component. A new technique is proposed in which a photon polarization plane perpendicular to the detector plane is considered.

In chapter 2 a somewhat simplified explanation of PhD is presented. While this provides an adequate introduction for chapters 4 and 5, an explanation of some of the omitted details relating to polarization is required for the current chapter.

6.1.1 Effects of Polarization on Spherical Waves

The PhD technique is based on the reduced angular momentum expansion theory (RAME) proposed by Fritzsche and Rennert [18]. The current discussion is by no means intended to be an exposition of the theory in its entirety but merely an attempt to extract and present the portions relevant to the given chapter title. According to this theory the total wave function at r (any position defined by a vector r) for the scattering problem is the sum of the incident wave φ and the outgoing wave ψ_s

$$\psi(r) = \varphi(r) + \psi_s(r) \qquad 6.1$$

The incident wave φ can be described as spherical representing either the wave function of the primary excited electron or the scattered wave of a preceding scattering process. For the purposes of describing the effects of perpendicular polarization on core level photoemission, only the incident wave function will be discussed, and more specifically the incident wave

function in the case of a primary excited electron. The general form of a spherical wave emitted from an atom in the origin of the coordinate system is given in terms of RAME. This takes the form of a Spherical Hankel function of the first kind coupled to a spherical harmonic expansion with the same reduced angular momentum according to the approximative expression:

$$\varphi_L(r) \approx \sum_{\tilde{L}} \mathrm{h}_{\tilde{l}}(kr)\, Y_{\tilde{L}}(r)\, P_{\tilde{L}L}(R) \qquad 6.2$$

Where $L=(l,m)$= angular momentum, $\tilde{L}=\left(\tilde{l},\tilde{m}\right)$= {(0,0); (1,-1); (1,0); (1,1)}= reduced angular momentum, $\mathrm{h}_{\tilde{l}}$ is a spherical Hankel function of the first kind and of order $\tilde{l}$, k is the photoelectron wave number given by k = $2\pi\sqrt{2}$mE/h, $Y_{\tilde{L}}$ are the spherical harmonics with polar and azimuthal quantum numbers $\left(\tilde{l},\tilde{m}\right)$ and $P_{\tilde{L}L}$ are the projection coefficients for an arbitrary position of R (these are defined elsewhere [18] but essentially describe the transformation of spherical harmonics under a rotation of the coordinate system and are used to bring the z-axes of the basis system into the direction of R).

The real parts of three spherical Hankel functions $h_0^{(1)}$, $h_1^{(1)}$ and $h_2^{(1)}$ given by equations 6.3 to 6.5 [66] respectively are presented in fig. 6.1 corresponding to the polar quantum numbers 0, 1 and 2.

$$h_0^{(1)} = j_{l=0}^{(1)} + ij_{l=0}^{(2)} = -ie^{ix}\frac{1}{x} \qquad 6.3$$

$$h_1^{(1)} = -e^{ix}\frac{x+i}{x^2} \qquad 6.4$$

$$h_2^{(1)} = ie^{ix}\frac{x^2+3ix-3}{x^3} \qquad 6.5$$

Where $j_l^{(1)}$ and $j_l^{(2)}$ are Bessel functions of the first and second kind respectively and $i=\sqrt{-1}$.

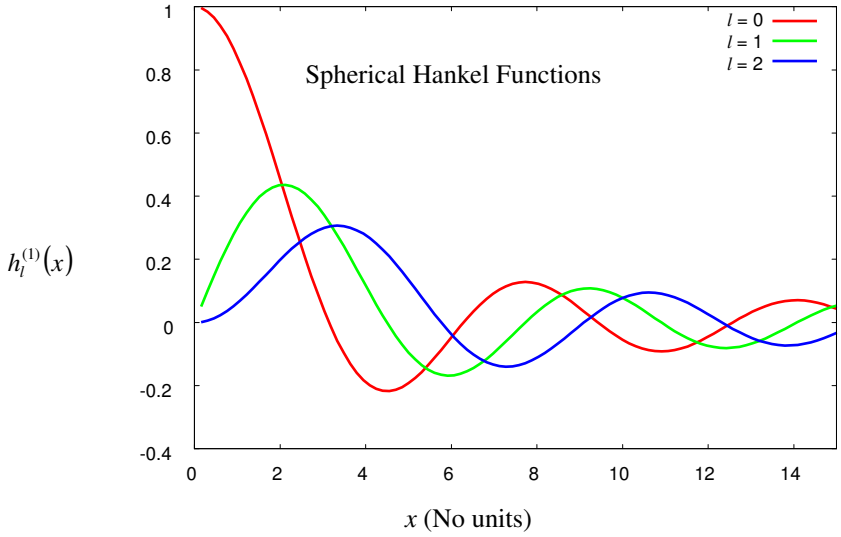

Fig. 6.1. A graphical representation of the real parts of the spherical Hankel functions $h_0^{(1)}$, $h_1^{(1)}$ and $h_2^{(1)}$.

These modify the intensities of the probability amplitudes resulting from the spherical harmonic expansion which is the part of expression 6.2 which is most relevant to the current discussion. The spherical harmonics are given in spherical polar coordinates by the general equations [67]:

$$Y_{l,m}(\vartheta,\varphi) = \Theta_{l,m}(\vartheta)\ \Phi_{l,m}(\varphi) \qquad 6.6$$

$$\Phi_m(\varphi) = \frac{1}{\sqrt{2\pi}} e^{im\varphi} \qquad 6.7$$

$$\Theta_{l,m}(\vartheta) = \left[\frac{2l+1}{2}\frac{(l-m)!}{(l+m)!}\right]^{1/2} P_{l,m}(\vartheta) \qquad 6.8$$

Where ϑ and φ are the polar and azimuthal angles respectively and $P_{lm}(\vartheta)$ is the associated Legendre polynomial. The first four normalized spherical harmonics are presented in table 6.1.

l	m	$\mathbf{Y}_{l,m}(\theta,\phi)$
0	0	$\frac{1}{\sqrt{4\pi}}$
1	0	$\sqrt{\frac{3}{4\pi}}\cos\theta$
1	±1	$\mp\sqrt{\frac{3}{8\pi}}\sin\theta\ e^{\pm i\phi}$
1	1	$\sqrt{\frac{3}{8\pi}}\sin\theta\ \cos\phi$ (real)
1	-1	$-i\sqrt{\frac{3}{8\pi}}\sin\theta\ \sin\phi$ (imaginary)

Table 6.1. First four normalized spherical harmonics.

Deriving the spherical harmonics becomes increasingly difficult with increasing l and m. Fortunately this is simplified in RAME which only requires an exact solution for the 4 spherical harmonics corresponding to $\tilde{L}=\left(\tilde{l},\tilde{m}\right)$. The spherical harmonics for higher values of l are approximated according to the expressions:

$$Y_{l,0}\approx\left[1-\frac{l(l+1)}{2}\right]\sqrt{2l+1}\ Y_{0,0}+\frac{l(l+1)}{2}\sqrt{\frac{2l+1}{3}}\ Y_{1,0}\,, \qquad 6.7$$

$$Y_{l,\pm1}\approx\sqrt{\frac{l(l+1)(2l+1)}{6}}\ Y_{1,\pm1}\,, \qquad 6.8$$

$$Y_{l,m}\approx 0\ \text{ for }\ |m|\geq 2\,. \qquad 6.9$$

Plotting $Y_{l,m}^2$ for the first four angular momenta reveals the familiar orbital shapes shown in fig. 6.2 A-D.

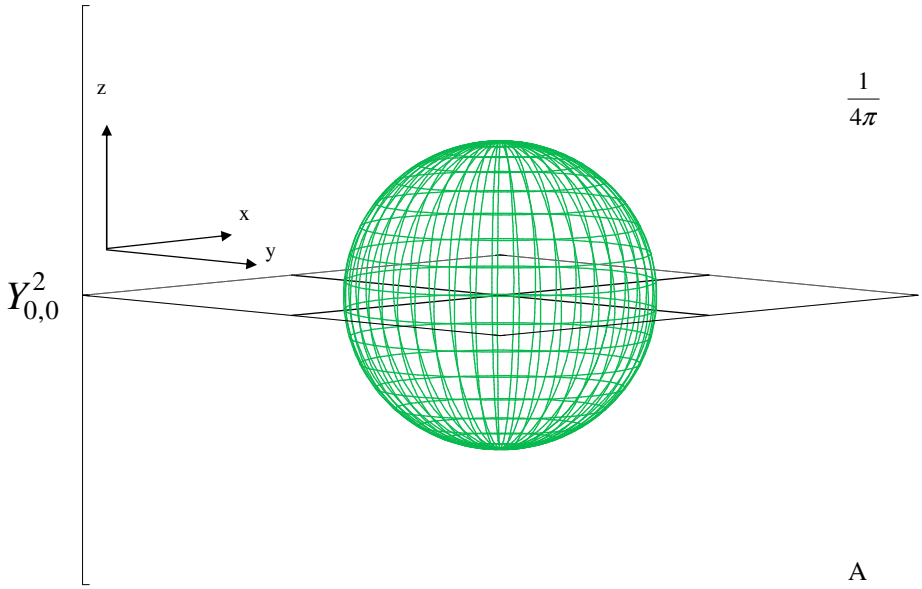
z
x
y
$Y^2_{0,0}$
$\frac{1}{4\pi}$
A

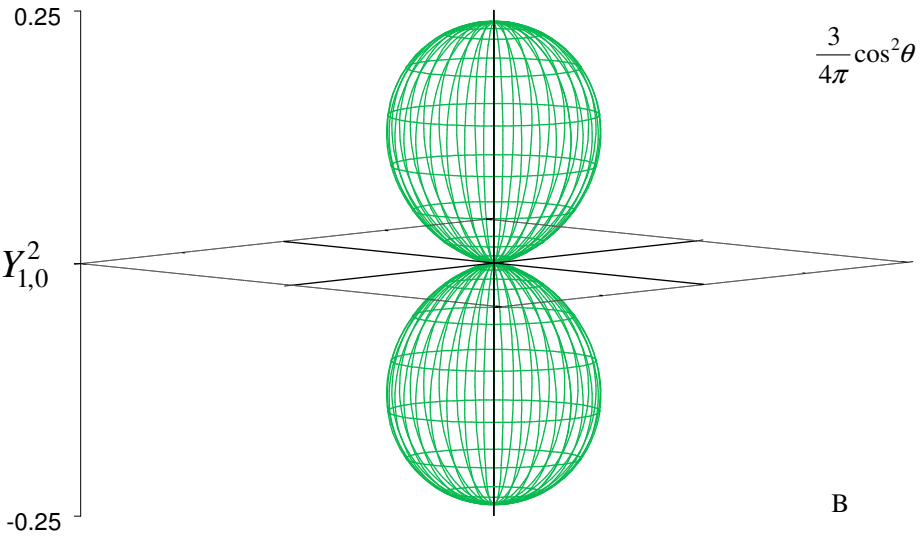
0.25
-0.25
$Y^2_{1,0}$
$\frac{3}{4\pi}\cos^2\theta$
B

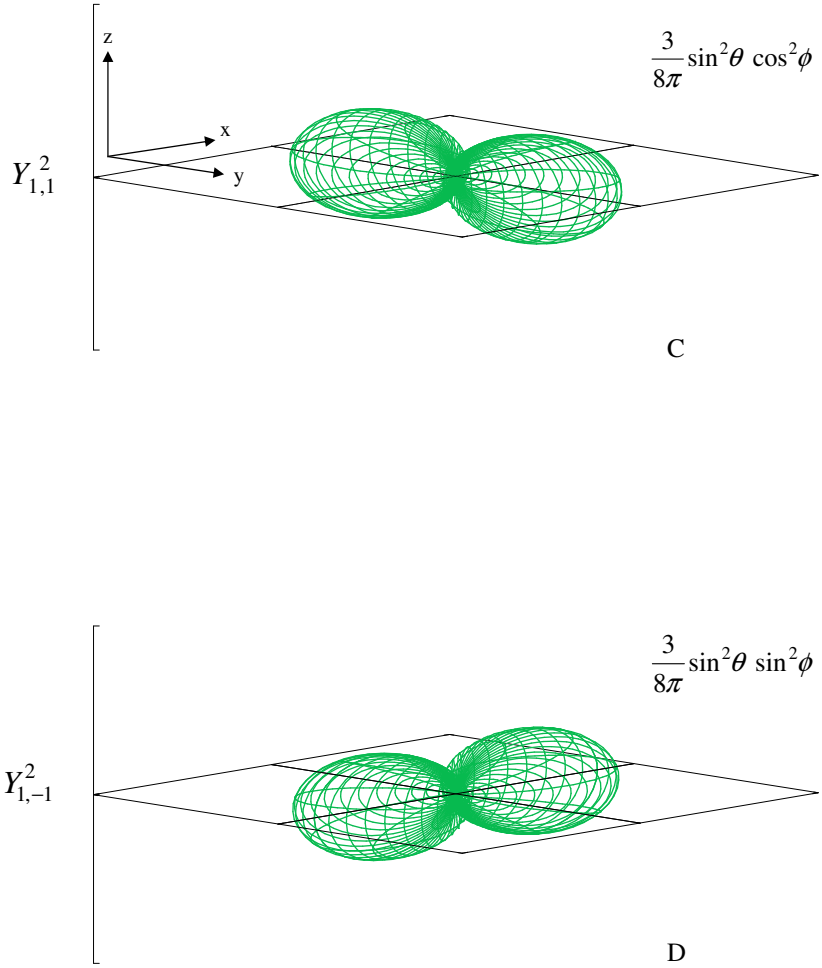

Fig. 6.2. Three dimensional plots of the square of the spherical harmonics where plots A-D correspond to the angular momenta (0,0), (1,0), (1,1) and (1,-1) respectively.

In a dipole k state to n state transition, the transition probability is proportional to the square of the matrix elements of the dipole transition:

$$\mathrm{D}_{k,n} = \int \psi_k^* \mathrm{p}\, \psi_n d\tau, \qquad 6.10$$

where ψ_k^* is the complex conjugate of the *k*-state wavefunction, ψ_n is the n-state wave function, p is the dipole moment of the system and $d\tau = \sin d\vartheta\, d\varphi$.

This can be expressed in its three Cartesian components as:

$$\mathrm{D}^{x}_{k,n} = -e\int \psi^{*}_{k} x \psi_{n} d\tau \ , \qquad 6.11$$

$$\mathrm{D}^{y}_{k,n} = -e\int \psi^{*}_{k} y \psi_{n} d\tau \ , \qquad 6.12$$

$$\mathrm{D}^{z}_{k,n} = -e\int \psi^{*}_{k} z \psi_{n} d\tau \ , \qquad 6.13$$

where z, for the purpose of the following argument, is the direction of the photon polarization vector.

Assuming the electrons move in a central field of force, the wave functions can be written in spherical polar coordinates as [68]:

$$\psi = e^{im\varphi} P_{l,m}(\vartheta) \ , \qquad 6.14$$

where the exponential term gives the dependence on the azimuthal angle φ and $P_{lm}(\vartheta)$ is the part of the function which depends on the polar angle. Substituting 6.14 into 6.11, and expressing Cartesian coordinates as spherical polar coordinates gives,

$$\mathrm{D}^{x}_{k,n} = \frac{e}{2}\int e^{-im\varphi} P_{l,m} \cos\varphi \sin\vartheta \ e^{im'\varphi} P_{l',m'} d\varphi \sin\vartheta \ d\vartheta \qquad 6.15$$

Using the trigonometric/complex exponential relationships,

$$\cos\varphi = \frac{e^{i\varphi} + e^{-i\varphi}}{2} \ , \qquad 6.16$$

$$\sin\varphi = \frac{e^{i\varphi} + e^{-i\varphi}}{2i} \ , \qquad 6.17$$

the components of the transition moments can be written as:

$$\mathrm{D}^{x}_{k,n} = \frac{e}{2}\int_{0}^{2\pi}\left(e^{i(m'-m+1)\varphi} + e^{i(m'-m-1)\varphi}\right)d\varphi\int_{0}^{\pi} P_{l,m}P_{l',m'}\sin^{2}\vartheta\, d\vartheta \qquad 6.18$$

$$\mathrm{D}^{y}_{k,n} = \frac{e}{2i}\int_{0}^{2\pi}\left(e^{i(m'-m+1)\varphi} - e^{i(m'-m-1)\varphi}\right)d\varphi\int_{0}^{\pi} P_{l,m}P_{l',m'}\sin^{2}\vartheta\, d\vartheta \qquad 6.19$$

$$\mathrm{D}^{z}_{k,n} = e\int_{0}^{2\pi} e^{i(m'-m)\varphi}d\varphi\int_{0}^{\pi} P_{l,m}P_{l',m'}\cos\vartheta\sin\vartheta\, d\vartheta \qquad 6.20$$

$\mathrm{D}^{z}_{k,n}$ differs from zero only when $m = m'$ for example, if $m = 0$ and $m' = 1$ then:

$$e^{i(1-0)\varphi} = e^{i\varphi} = \cos\varphi + i\sin\varphi \qquad 6.21$$

Substituting this back into the azimuthal part of 6.20 gives:

$$e\int_{0}^{2\pi}(\cos\varphi + i\sin\varphi)d\varphi =$$

$$i\sin 2\pi - i\sin 0 = 0 \qquad 6.22$$

On the other hand if both m and m' are equal i.e. $\Delta m = 0$, $e^{i(m'-m)\varphi}$ is equal to 1 meaning that $\mathrm{D}^{z}_{k,n}$ is dependent only on the polar angle. Furthermore, when $\Delta m = 0$ $\mathrm{D}^{x}_{k,n}$ and $\mathrm{D}^{y}_{k,n}$ are both equal to zero; for example taking the azimuthal part of 6.18 and setting $m = m'$ gives,

$$\frac{e}{2}\int_{0}^{2\pi}\left(e^{i(m'-m+1)\varphi} + e^{i(m'-m-1)\varphi}\right)d\varphi =$$

$$\frac{e}{2}\int_{0}^{2\pi}\left(\cos\varphi + i\sin\varphi + \cos\varphi - i\sin\varphi\right)d\varphi =$$

$$\frac{e}{2}\int_0^{2\pi}(2\cos\varphi)\ d\varphi =$$

$$e(\sin 2\pi - 2\sin 0) = 0 \qquad 6.23$$

Doing the same for 6.19 gives,

$$\frac{e}{2i}\int_0^{2\pi}\left(e^{i(m'-m+1)\varphi} - e^{i(m'-m-1)\varphi}\right)\ d\varphi$$

$$= \frac{e}{2i}\int_0^{2\pi}(\cos\varphi + i\sin\varphi - \cos\varphi + i\sin\varphi)\ d\varphi$$

$$= e\int_0^{2\pi}(\sin\varphi)\ d\varphi$$

$$= e(-\cos 2\pi + \cos 0) = 0 \qquad 6.24$$

Thus, excitation by polarized radiation imposes a selection rule for the magnetic quantum number *m*, meaning only certain definite transitions will take place; if the light is linearly polarized the result will be transitions in which the magnetic quantum number remains constant ($\Delta m=0$) [68]. Consequently, the z-axis or π component of the n-state wavefunction must be parallel to the polarization vector (fig 6.3).

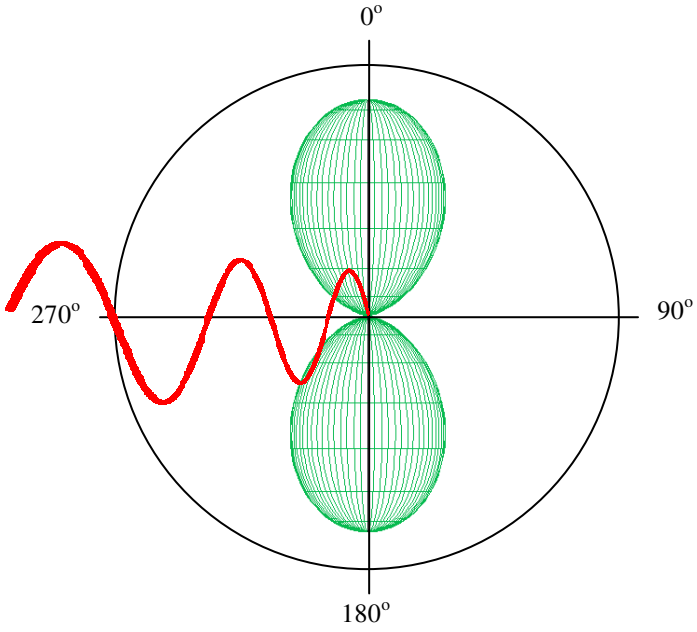

Fig.6.3. Angular distribution of k-shell photoemission with respect to the incident radiation polarization vector (ε) indicating a ε·R dependency for a simplified single atom case.

The diagram in fig. 6.3 shows a simplified depiction of the $\varphi_L^2(r)$ function which includes only the spherical harmonic function for an angular momentum of (1,0). While the influences of other angular momenta, the spherical Hankel functions and neighbouring atoms have been omitted, an angular dependence showing a maximum along the 0°/180° axis which is parallel to the radiation vector and a minimum in the 90°/270° axis is reasonably represented [69], [70].

In essence, the use of radiation linearly polarized in the plane perpendicular to the detector plane results in none of the directly emitted electrons being detected, leaving only the detection of the scattered electrons. A difficulty which is immediately evident from this principle is that the signal strength is greatly reduced which in turn results in a reduction in the signal to noise ratio. The benefit on the other hand, is less obvious and only becomes apparent on simulation of the PhD experiments and takes the form of a significant increase in the modulation strength (whether or not this is mirrored experimentally remains to be seen). A theoretical comparison of the modulation strengths resulting from the use of vertically and horizontally polarized radiation will be presented.

6.2 Aim

The aim of this chapter is to explore the effects of using vertically and horizontally polarized radiation on PhD modulation amplitudes and more importantly, determining the sensitivity of each method to various structural parameters. To this end, comparative simulations have been undertaken using the structural data for CO adsorption on Pt(111) obtained in chapter 4, and that for benzene adsorption on Si(001) obtained in chapter 5.

6.3 Results and Discussion

6.3.1 CO Adsorption on Pt(111)

Using the Pt(111)c(5x√3)rect.3CO structure optimized in chapter 4, theoretical modulation functions for several emission angles were produced. The emission angles were composed of polar angles ranging from normal emission to normal incidence in 10º steps, and azimuthal angles ranging from 0º corresponding to the $[\bar{1}10]$ direction to 90º corresponding to the [011] direction, also in 10º steps. At a polar angle of 0º the modulation functions for all of the azimuthal angles are equivalent. This however is not the case for non-zero polar angles. Table 6.2 shows some of the equivalent azimuthal angles for C 1s photoemission.

Equivalent Azimuthal Angles between 0º - 90º				
Atop			Bridge	
0	60		0	60
10	50	70	10	70
20	40	80	20	80
30	90		30	90
			40	
			50	

Table 6.2. Equivalent Azimuthal Angles between 0º - 90º for non-zero polar angles.

This equivalence arises due to the fact that six domains, rotated through 60º with respect to one another have been included in the simulation model (refer back to section 4.3.2). For example 60º degrees in the first symmetry is equivalent to zero degrees in the second symmetry which is rotated by 60º. For the atop species a further equivalence arises due to the configuration of the

atop sites (see fig.6.4). For example the 20º direction with respect to site A is equivalent to the 40º direction when compared with site B through a rotation of 120º.

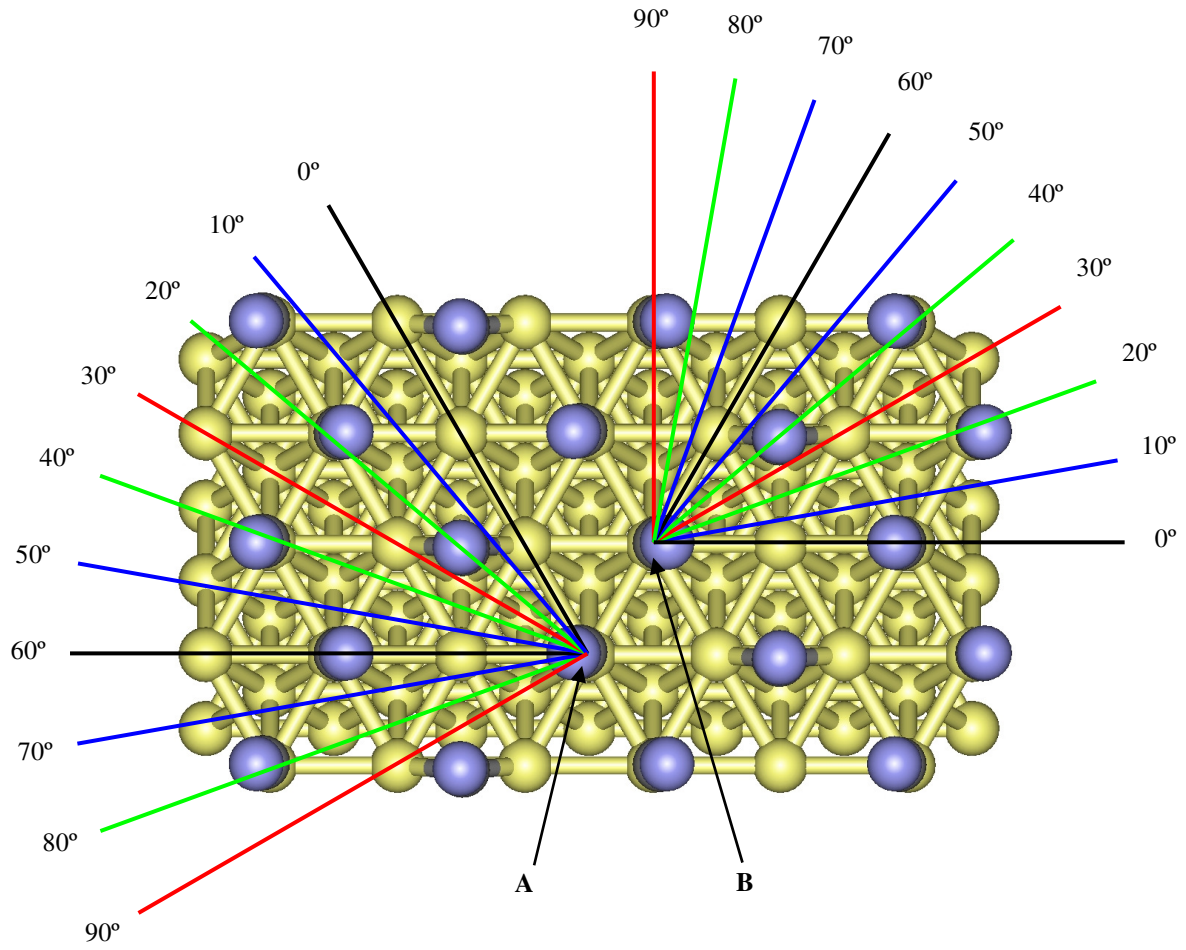

Fig. 6.4. Diagram showing the equivalence of angles 0º and 60º and 20º and 40º for domains rotated by 120º. Sites A and B are equivalent through a rotation of 180º

As the modulation function is independent of the azimuthal angle at normal emission, only one azimuthal angle is necessary for comparison of the modulation functions for each polarization vector. Fig. 6.5 shows a comparison of the modulation functions for perpendicular polarization PhD (PPPhD) and conventional PhD for normal emission. PPPhD, at first glance exhibits only a marginal increase in amplitude compared with PhD, however, taking the RMS of both modulation amplitudes reveals an increase of a factor of 2. This becomes even more pronounced when considering the bridge species where the amplitude is increased by a factor of 3.

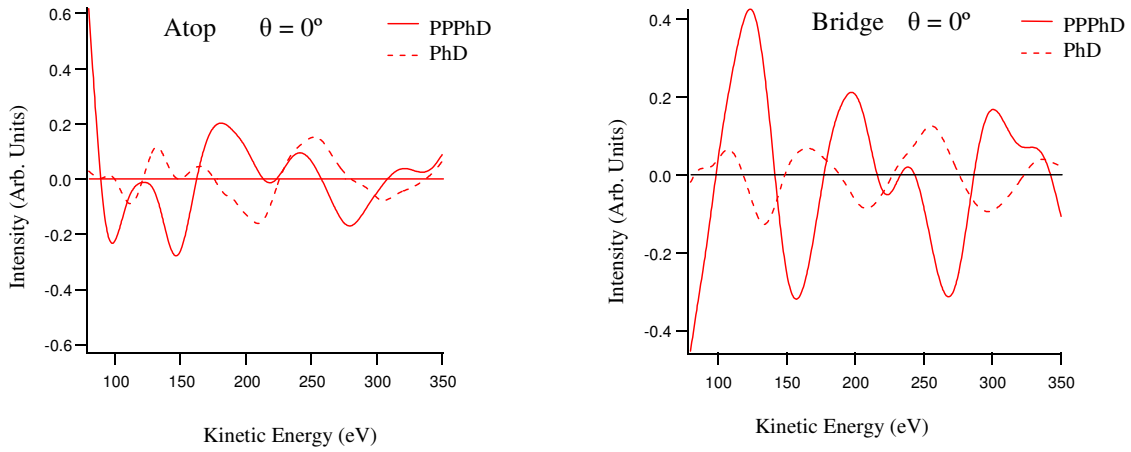

Fig. 6.5. Comparison of theoretical modulation functions for PhD and PPPhD at θ = 0º for Pt(111)c(5x√3)rect.3CO.

The PPPhD exhibits greater modulation amplitudes than PhD throughout all of the angles considered. Table 6.3 shows the root mean square (RMS) ratios for the PPPhD/PhD modulation functions for all of the above mentioned emission angles given by equations 6.24 and 6.25.

$$I_{rms} = \sqrt{\frac{1}{n}\sum_{i=1}^{n} I_i^2} \qquad 6.24$$

$$\frac{I_{rms}(PPPhD)}{I_{rms}(PhD)} \qquad 6.25$$

Atop							
θ / **ϕ**	0º	10º	20º	30º	40º	50º	60º
0º	1.99	1.53	3.72	6.64	4.39	4.50	4.55
10º	1.99	1.18	2.16	3.04	2.06	8.10	4.50
20º	1.99	1.30	2.58	3.30	2.67	8.14	10.26
30º	1.99	1.71	3.95	3.39	3.77	4.97	4.43
Bridge							
0º	3.21	3.45	3.97	3.57	2.87	3.63	2.46
10º	3.21	3.03	4.06	2.43	2.91	3.64	2.64
20º	3.21	4.19	3.02	6.94	4.92	3.30	5.90
30º	3.21	4.16	5.28	2.70	6.48	4.06	2.55
40º	3.21	3.69	5.71	5.98	3.89	2.80	6.30
50º	3.21	4.37	4.48	1.57	3.90	3.08	1.98

Table 6.3. Angle dependence of the PPPhD/PhD RMS ratios for the Pt(111)c(5x√3)rect.2CO system.

The smallest PPPhD/PhD ratio is observed for the atop species in the emission directions involving the 10º polar angles. This might be expected due to the 10° tilt in the atop species and the favourable PhD backscattering along the CO axis. However, this is an over simplified explanation as the RMS amplitudes for the normal emission directions are marginally higher than those for the 10^{o}_{0} directions yet the RMS ratios are also higher. The changes in PPPhD/PhD amplitude ratios seem to be resistant to the formulation of simple rules of thumb. This is because the reference wave is lost and the modulations are due to the relative phases of the singly and multiply scattered waves.

While the sensitivity to the azimuthal angle generally increases beyond a polar angle of 10º for both methods, this is markedly enhanced in PPPhD (see fig. 6.6, A-D).

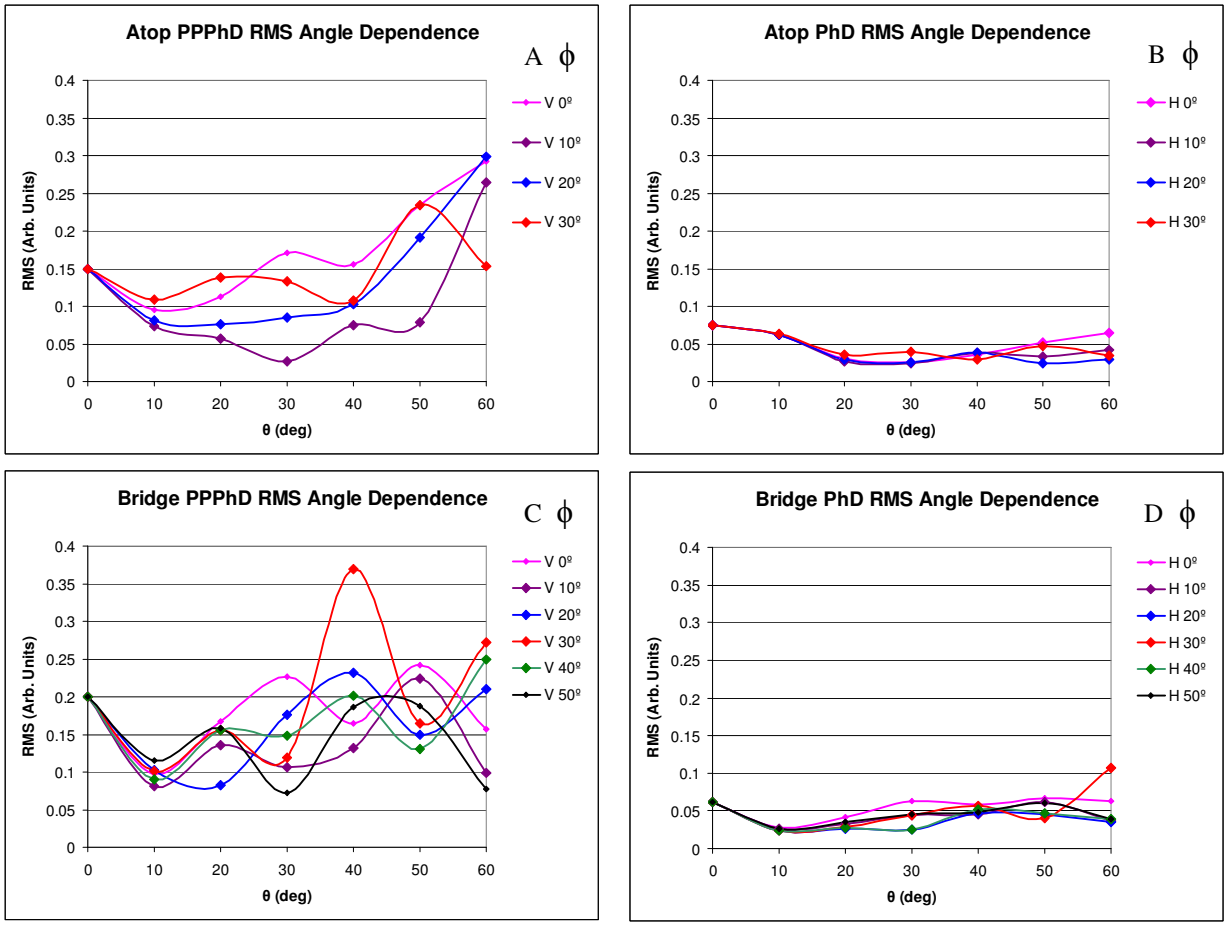

Fig. 6.6 Graphs A-D are presented with the same scale to allow a direct comparison of the RMS amplitudes. A and B correspond to the atop PPPhD and PhD amplitudes respectively and show that the range of intensities is considerably more pronounced for PPPhD. C and D correspond to the bridge PPPhD and PhD amplitudes and also reveal a general increase in intensity and a greater range in amplitudes for PPPhD.

The graphs A-F from which the RMS amplitudes have been calculated, are presented in figs. 6.6 - 6.8. They are shown with the same offset between modulation curves of 0.4 so that a direct comparison can be made. The increased amplitude for polar angles of 40º and above necessitated the doubling of the offset for graphs G-L in figs. 6.9 – 6.11 for clarity.

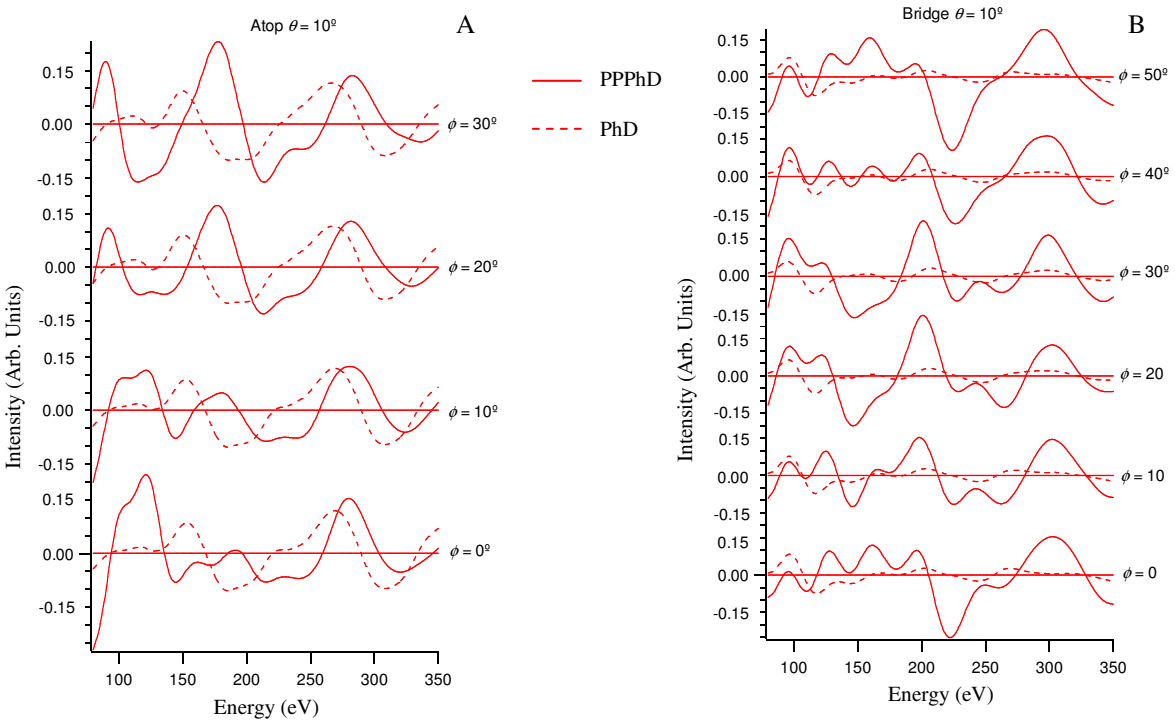

Fig. 6.6. Comparison of modulation functions for PPPhD and PhD for the Pt(111)c(5x√3)rect.2CO system at θ = 10º for azimuthal angles ranging from 0º to 50º

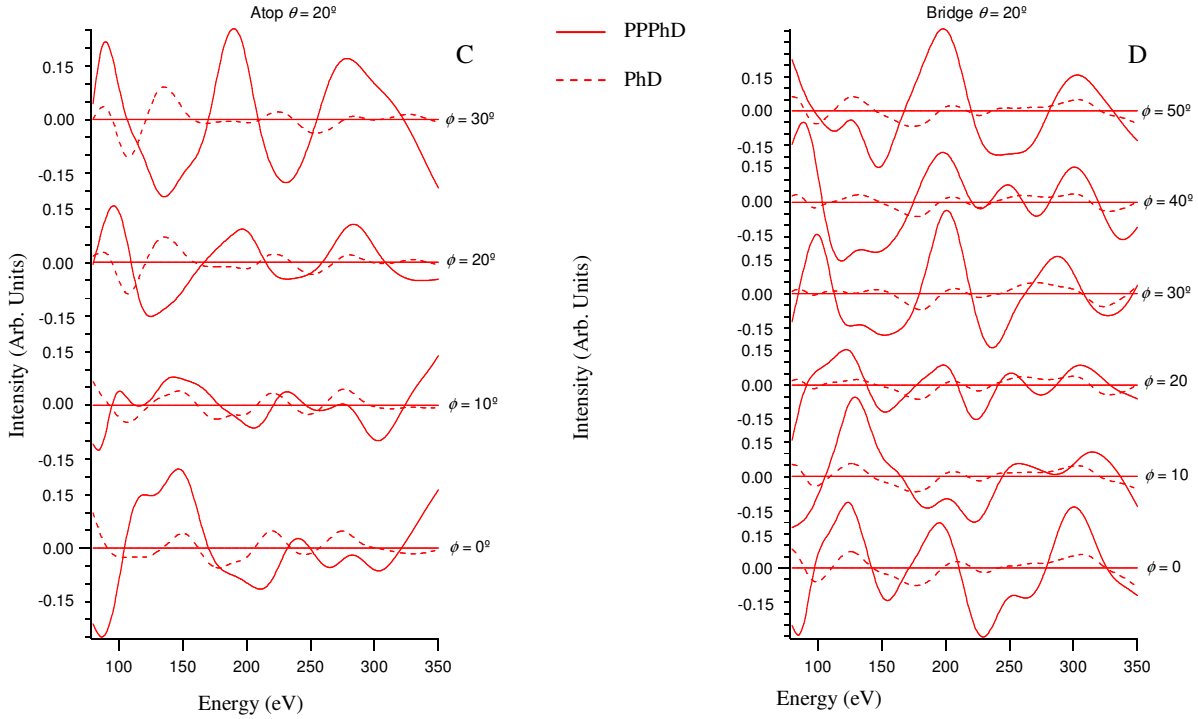

Fig. 6.7. Comparison of modulation functions for PPPhD and PhD for the Pt(111)c(5x√3)rect.2CO system at θ = 20º for azimuthal angles ranging from 0º to 50º

Increasing the polar angle to 20º further increases the difference between PPPhD and PhD for the atop species along the 0º and 30º azimuthal directions. However a slight decrease is observed in the 10º and 20º directions. A more general increase is observed for the bridge species with the one exception at 20º where there is a marginal decrease. Although this decreased difference still represents a stark contrast between PPPhD and PhD.

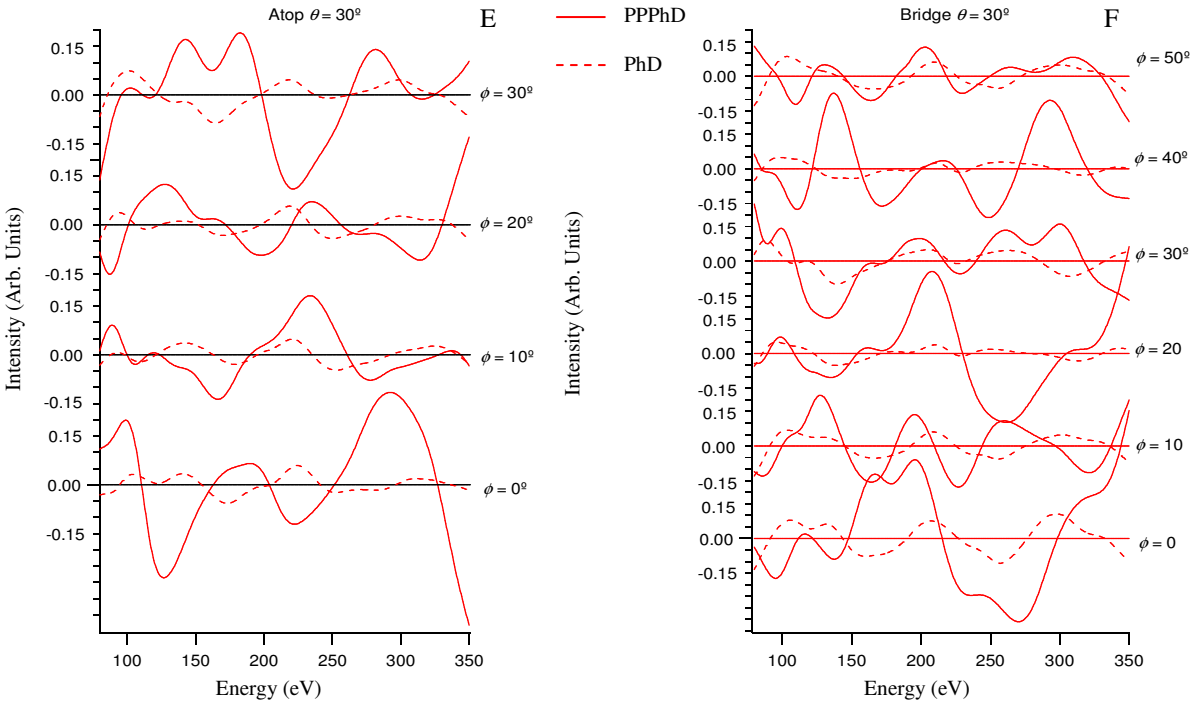

Fig. 6.8. Comparison of modulation functions for PPPhD and PhD for the Pt(111)c(5x√3)rect.2CO system at θ = 30º for azimuthal angles ranging from 0º to 50º

As the polar angle is increased further to 30º the gap between PPPhD and PhD continues to grow. Again there are exceptions; 20º for the atop species and 30º and 50º for the bridge species show a slight reduction in modulation amplitude compared with those calculated at θ = 20º.

Increasing the polar angle to 40º results in little change in the modulation amplitude for most directions excepting 30º and 50º where the modulation amplitude is almost quadrupled for the bridge species.

While these comments are mainly descriptive, the general idea emerging is that the modulation amplitudes increase with polar angle. This however, is coupled with a significant dependence on the azimuthal angle especially beyond ϕ = 10º obscuring any definite trend there might be.

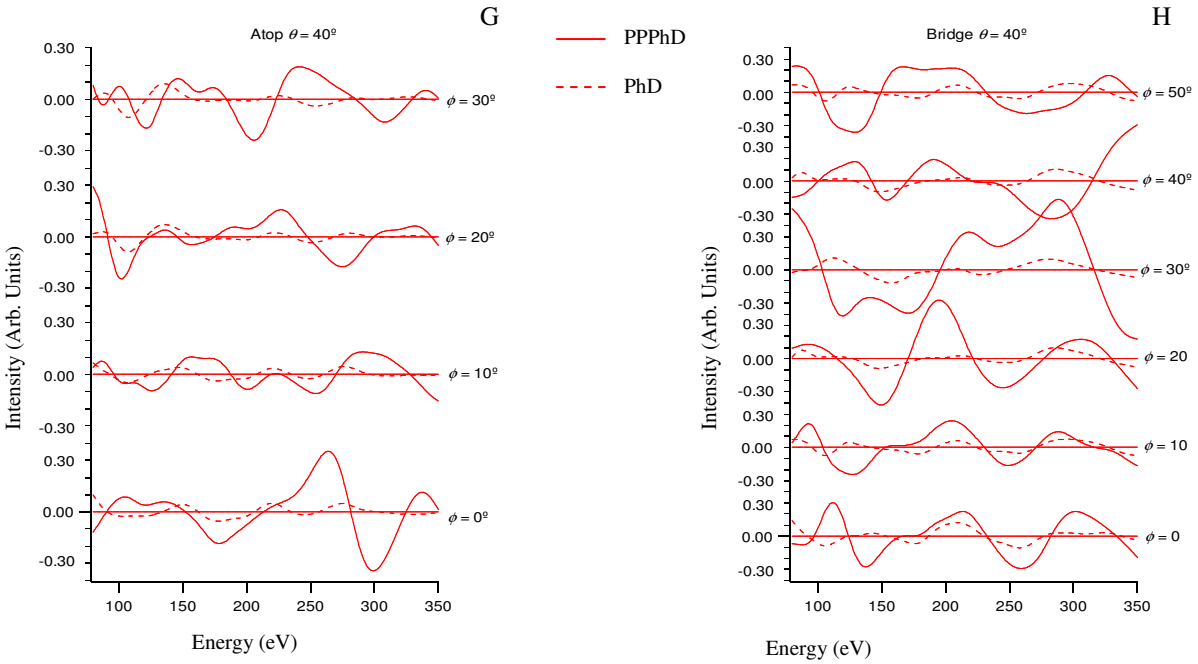

Fig. 6.9. Comparison of modulation functions for PPPhD and PhD for the Pt(111)c(5x√3)rect.2CO system at 40º for azimuthal angles ranging from 0º to 50º

Increasing θ to 50º results in a small increase in the modulation amplitude for PPPhD with the exception of the 30º azimuthal direction for the bridge species.

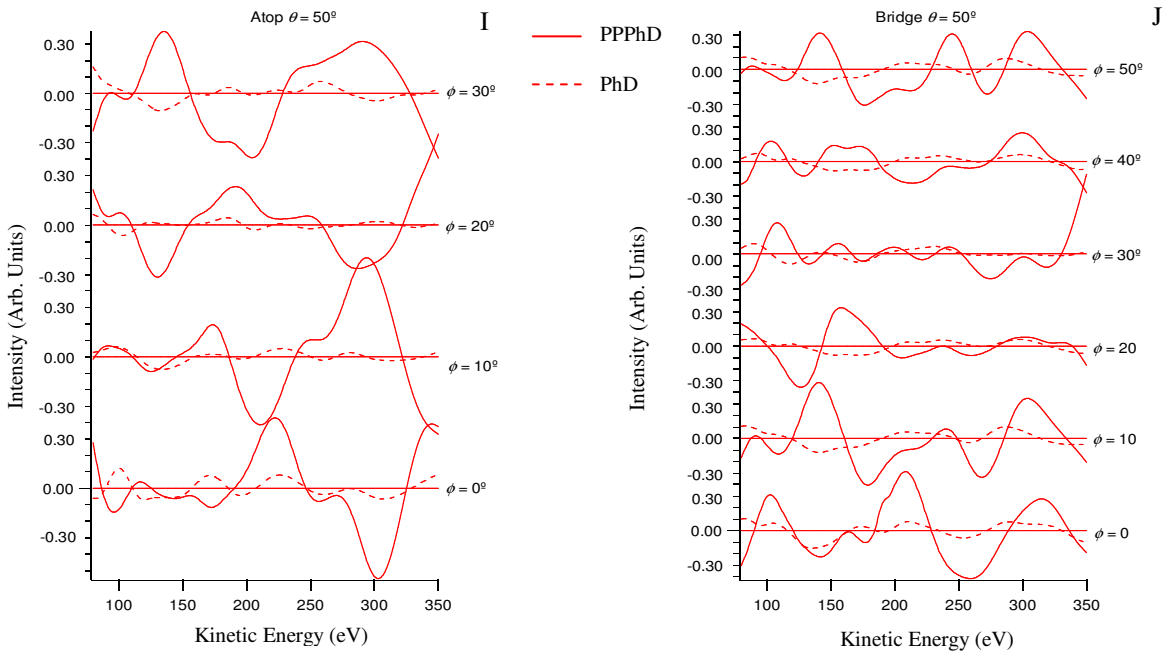

Fig. 6.10. Comparison of modulation functions for PPPhD and PhD for the Pt(111)c(5x√3)rect.2CO system at 50º for azimuthal angles ranging from 0º to 50º.

Finally increasing θ to 60º reveals a further increase in modulation amplitude in the 20º azimuthal direction. The change in amplitude throughout these angles for PhD is relatively insignificant.

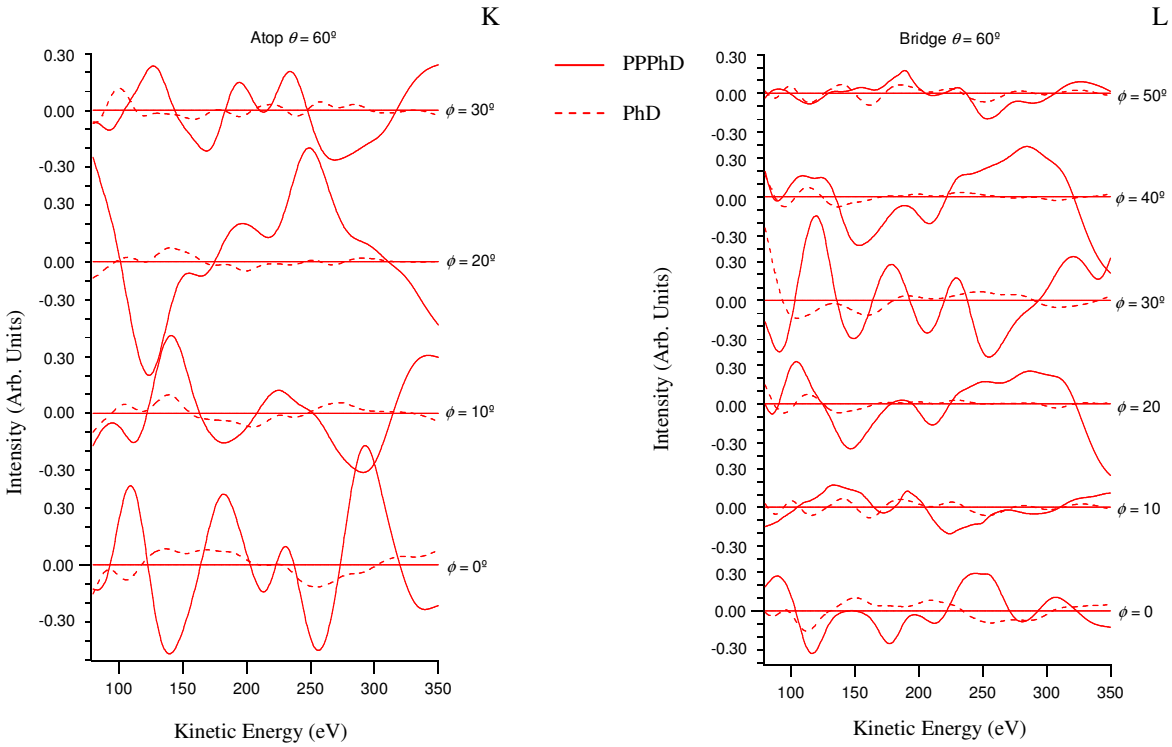

Fig. 6.11. Comparison of modulation functions for PPPhD and PhD for the Pt(111)c(5x√3)rect.2CO system at 60º for azimuthal angles ranging from 0º to 50º

In summary, while no definite pattern to the changing modulation strength is discernable, it can at least be said that the modulation strengths are normally much greater for PPPhD than PhD for CO adsorption on Pt(111). The question that naturally arises from this is whether or not this increase translates to a general increase in sensitivity to the structural parameters. To answer this question a selection of emission angles was chosen (tabulated in table 6.4) using the theoretical modulation functions as a reference. Various parameters were varied from their original values causing the R-factor to deviate from a value of zero. The extent of this deviation as a result of the changing parameter gives an indication of the sensitivity of the technique to that parameter.

Atop		Bridge	
θ	ϕ	θ	ϕ
0º	0º	0º	0º
10º	10º	10º	10º
20º	20º	20º	20º
30º	30º	30º	30º
40º	40º	40º	40º
40º	0º	40º	0º
50º	50º	50º	50º

Table 6.4. Emission angles used in PPPhD and PhD. An extra comparison in which the angles in blue replaced the angles in red was carried out on consideration of the Pt-C_{bridge} bond length.

This dependence is best expressed graphically. However, in order to quantify this dependence for a numerical comparison, the concave section of the graphs about the minimum were fitted with a 2nd order polynomial. Taking the second derivative of the polynomial gives a single value for the degree of change with respect to the changing parameter. Taking these values for both methods and dividing that for PPPhD by that for PhD gives a crude, but useful comparison of the sensitivity of the two methods for a given parameter. For the purposes of this chapter this will be referred to as the sensitivity ratio.

Additionally, the variance obtained in chapters 4 and 5 for each structural parameter is used to give an approximation of the expected variance for the theoretical PhD data. This is done by taking the range given by the experimental variance and determining the R-factor at which this range is matched on the theoretical variance curve. A new horizontal line is drawn at the said R-factor and the intercepts on the PPPhD variance curve gives the approximate PPPhD variance (see fig. 6.12).

Fig. 6.12 shows the PPPhD and PhD variance graphs for the atop Pt-C bond lengths. Clearly, the PhD graph changes more steeply than the PPPhD graph. The sensitivity ratio is 0.31 meaning that the degree of change in R-factor with bond length for PPPhD is around 0.31 times that for PhD. Taking the variance of ± 0.02 Å for the Pt-C_{Atop} bond length gives an approximate variance for PPPhD of ± 0.04 Å.

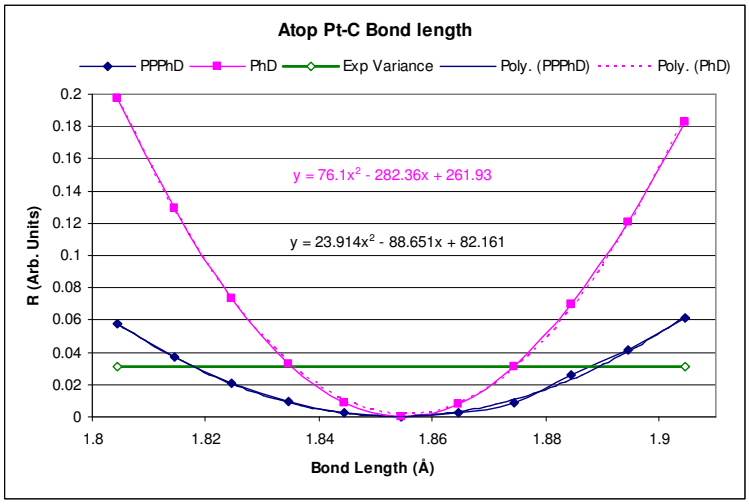

Fig. 6.12. PPPhD/PhD comparison for the atop Pt-C bond length yielding a sensitivity ratio of 0.31 and giving an approximate PPPhD variance of ± 0.04 Å.

The Pt-C bond length parameter represents the pinnacle of PhD sensitivity in the CO/Pt(111) system because the method mainly exploits the interference between the directly emitted wave function and backscattered wave function which is predominantly influenced by the distance between the emitter and the backscattering atom (see fig.2.8). The absence of this information in PPPhD might intuitively be interpreted as the reason for its reduced sensitivity to this parameter. However, this interpretation is an oversimplification which can be demonstrated as follows. The Pt-C_{bridge} bond axis lies at 44º in the [110] direction; replacing the emission angle composed of θ = 40º and ϕ = 0º by that composed of θ = 40º and ϕ = 40º should result in reduction in the sensitivity of PhD to the Pt-C_{bridge} bond length. It does, marginally. However the sensitivity of PPPhD is also reduced resulting in a drop in the sensitivity ratio from 1.22 to 1.04. Fig.6.13 shows the comparison of PPPhD and PhD for both sets of emission angles.

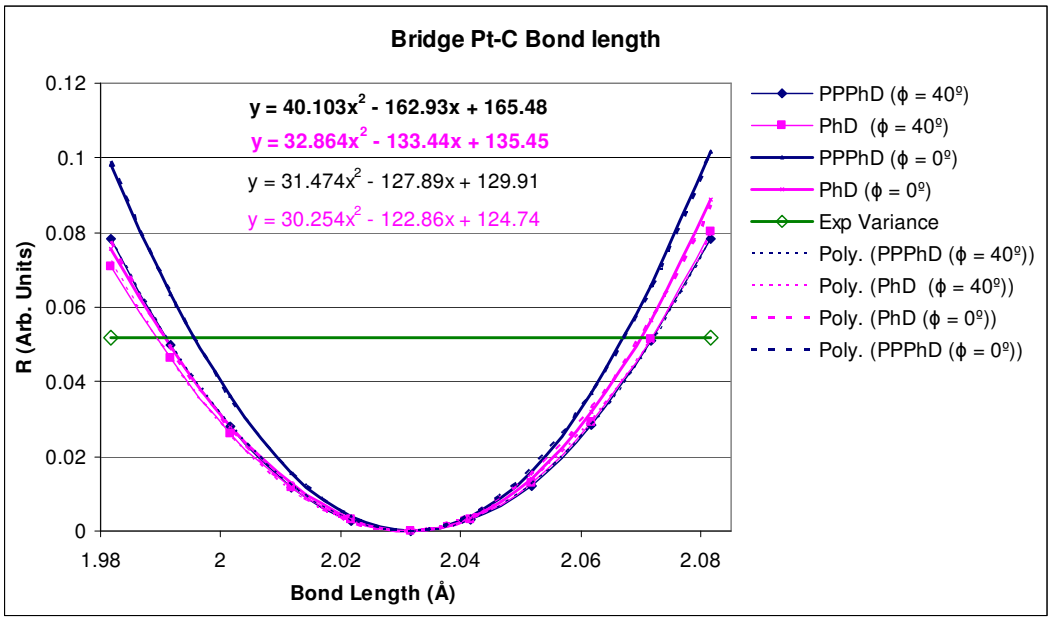

Fig. 6.13. PPPhD/PhD comparison for the bridge Pt-C bond length. The thin lines represent the comparison made when the emission angle composed of 40º$_\theta$ and 40º$_\phi$ was included. The bold lines represent the comparison made when the emission angle composed of 40º$_\theta$ and 0º$_\phi$ was used. The respective sensitivity ratios were 1.04 and 1.22. The variances for PPPhD and PhD (ϕ = 40º) are ± 0.038 Å and ± 0.040 Å respectively. Those for PPPhD and PhD (ϕ = 0º) are ± 0.035 Å and ± 0.038 Å, respectively.

A PPPhD/PhD comparison for the C-O$_{atop}$ and C-O$_{bridge}$ bond lengths presented in fig. 6.14 and 6.15 reveals that in both cases PhD appears to be the more sensitive technique.

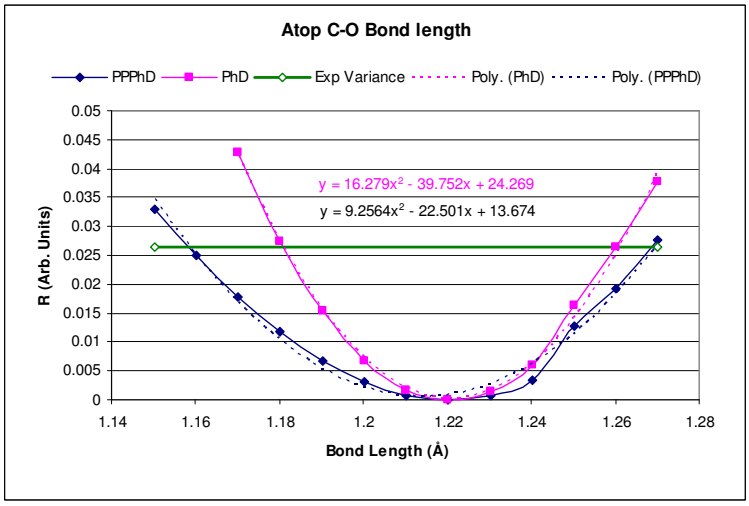

Fig. 6.14. PPPhD/PhD comparison for the atop C-O bond length yielding a sensitivity ratio of 0.57, a PPPhD variance of +0.048/-0.061 Å, and a PhD variance of ± 0.039 Å.

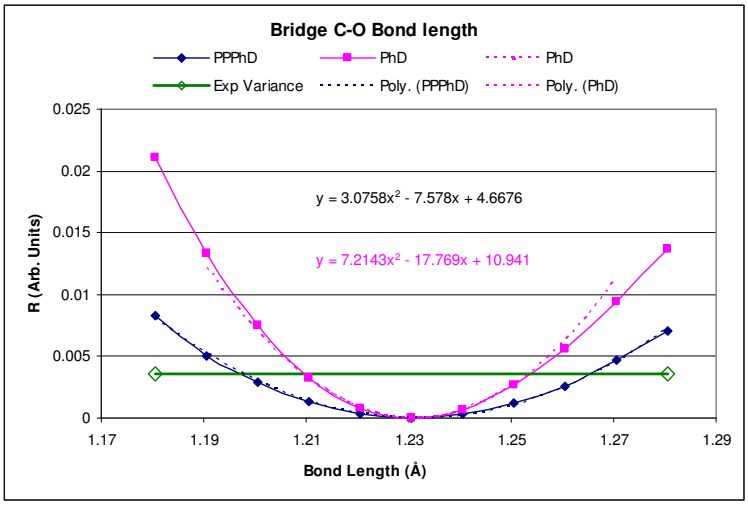

Fig. 6.15. PPPhD/PhD comparison for the bridge C-O bond length yielding a sensitivity ratio of 0.4, a PPPhD variance of +0.035/-0.034 Å, and a PhD variance of +0.020/-0.024 Å.

The more lateral parameters such as $\theta_{\text{(atop Pt-C)}}$, $\phi_{\text{(atop Pt-C)}}$ and $\phi_{\text{(bridge Pt-C)}}$ all appear to be more discernable with the PPPhD method (see figs 6.16- 6.19).

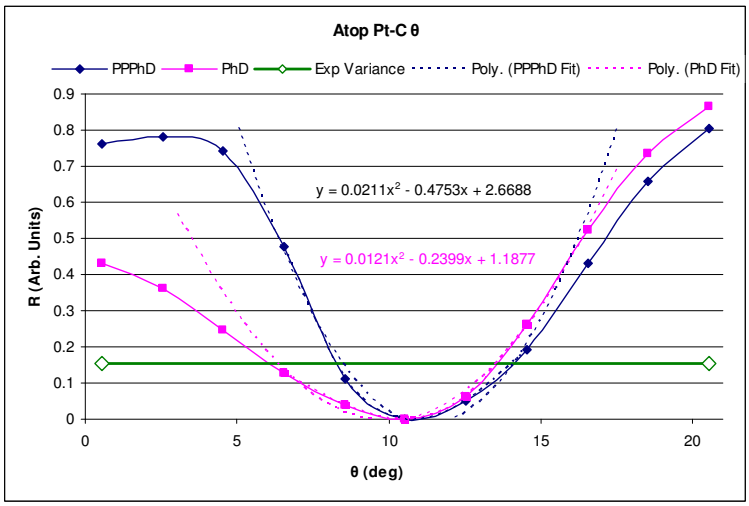

Fig. 6.16. PPPhD/PhD comparison for the atop Pt-C polar bond axis yielding a sensitivity ratio of about 1.75, a PPPhD variance of +3.58º/-2.24º and a PhD variance of +3.07º/-4.56º.

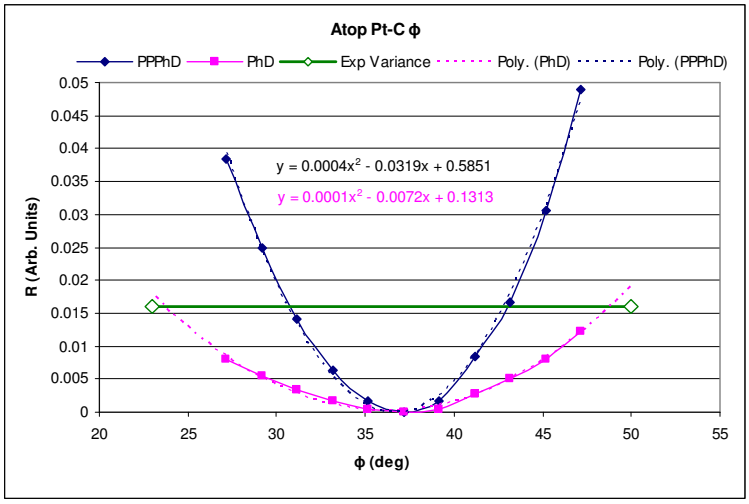

Fig. 6.17 PPPhD/PhD comparison for the atop Pt-C azimuthal bond axis yielding a sensitivity ratio of 4.0, a PPPhD variance of +2.54°/-2.74° and a PhD variance of +5.02°/-5.72°.

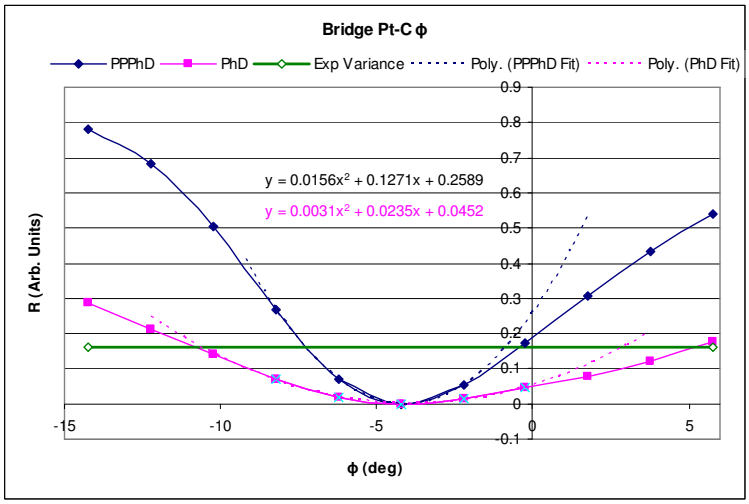

Fig. 6.18 PPPhD/PhD comparison for the bridge Pt-C azimuthal bond axis yielding a sensitivity ratio of 5.0, a PPPhD variance of +4.03/-3.1 and a PhD variance of +6.71°/-9.77°.

The fact that PhD seems to be more sensitive to the Pt-C_{atop}, C-O_{atop} C-O_{bridge} bond lengths while PPPhD appears to be more sensitive to parameters such as $\theta_{Pt\text{-}C}$(atop), $\phi_{Pt\text{-}C}$(atop) and $\phi_{Pt\text{-}C}$(bridge), suggests that PhD and is more sensitive to vertical displacements while PPPhD is more sensitive to lateral displacements. To explore this point further, the $\theta_{Pt\text{-}C}$(bridge) parameter was considered. The Pt-C_{bridge} bond axis as mentioned earlier, sits at an angle 44° from normal; changing this angle results in similar lateral and vertical displacements which, if the preceding argument is correct, should yield similar results for each method. Fig. 6.16 shows that the results are in fact similar for PPPhD and PhD giving a sensitivity ratio of 0.95.

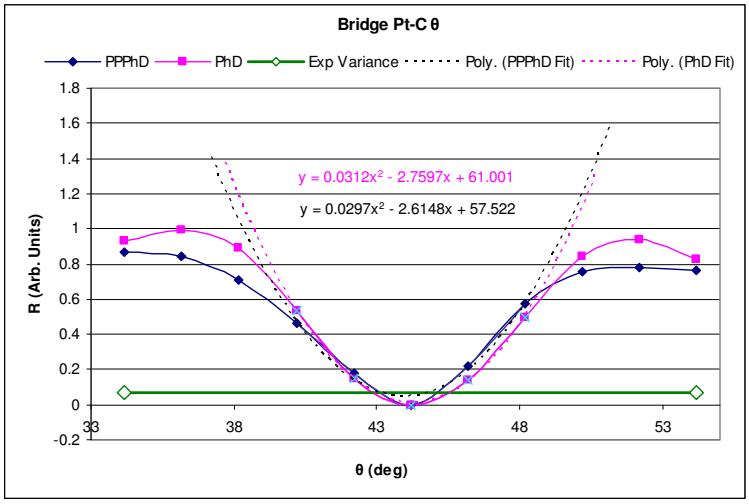

Fig. 6.19 PPPhD/PhD comparison for the bridge Pt-C polar bond axis yielding a sensitivity ratio of about 0.95, a PPPhD variance of +0.98º/-1.07º and a PhD variance of ±1.35º.

Changing the Pt-C_{bridge} bond length also results in similar vertical and lateral displacements and indeed results in a sensitivity ratio of 1.04 when the emission angle composed of $40º_{\theta}$ and $40º_{\phi}$ was included. However, as already mentioned, when an emission angle inline with the Pt-C_{bridge} bond axis is used, this ratio is increased to 1.22.

A question arising from this is whether or not the sensitivity ratios are dependent on the emission angles used. Replacing the emission angle composed of $\theta = 40º$ and $\phi = 0º$ by that composed of $\theta = 40º$ and $\phi = 40º$ when considering the Pt-C_{bridge} bond length clearly had some influence, on the sensitivity ratio. To clarify this dependence, line scans for the Pt-C_{atop} bond length, and the $\theta_{Pt\text{-}C}$(bridge) and $\phi_{Pt\text{-}C}$(atop) parameters were carried out using the alternative emission angles given in table 6.5.

Atop		**Bridge**	
θ	**ϕ**	**θ**	**ϕ**
0º	0º	0º	0º
10º	0º	20º	0º
60º	0º	40º	0º
10º	30º	20º	30º
20º	30º	40º	30º
50º	30º	60º	30º

Table 6.5 Alternative emission angle used for the determination of the influence of emission angle selection on the PPPhD/PhD sensitivity ratio used in the line scans for the Pt-C_{atop} bond length, and the $\theta_{Pt\text{-}C}$(bridge) and $\phi_{Pt\text{-}C}$(atop) parameters.

These parameters were selected because they cover the range where the sensitivity ratio is <1, ~1, and >1, respectively. The ratio for the Pt-C_{atop} bond length showed no change at all, that for the $\theta_{Pt\text{-}C}$(bridge) parameter showed virtually no change (0.9519 compared with 0.9455), while that for the $\phi_{Pt\text{-}C}$(atop) increased from 4 to 5 which, when considering the change in the variance from ± 6.17º to 6.01º, is also very little. While the example which gave rise to this discussion (fig. 6.13), reveals a change in the sensitivity ratio from 1.04 to 1.22, the change in the predicted variance is very small (from 0.035 to 0.038 for PPPhD and 0.038 to 0.040 for PhD), meaning that relative sensitivities of PPPhD and PhD are essentially independent of the emission angles used.

In conclusion then, PhD appears to be the more sensitive technique when considering mainly vertical displacements while PPPhD appears to be the more sensitive technique when considering mainly lateral displacements and when the parameters involve change in both lateral and vertical directions in similar amounts, both techniques are equally sensitive. This potentially makes PPPhD ideal for adsorption systems in which the adsorbates lie across the substrate such as benzene adsorbed on Si(001).

6.3.2 Benzene Adsorption on Si(001)

Using the optimised Si(001)(2x1)-C_6H_6 structural model from chapter 5 consisting of both butterfly and tight bridge species, the sensitivity of PPPhD was explored as above.

A comparison of the theoretical modulation functions for PPPhD and PhD was carried out for several emission angles. The polar and azimuthal angles from which these emission angles are composed are given in table 6.6 along with their respective PPPhD/PhD RMS amplitude ratios.

PPPhD/PhD RMS Ratios							
θ ϕ	0°	10°	20°	30°	40°	50°	
0°	7.34	7.79	22.23	15.34	6.87	11.23	2.86
10°	7.34	7.59	12.37	10.47	4.80	7.28	2.21
20°	7.34	6.82	4.85	7.54	11.94	11.07	6.59
30°	7.34	6.75	3.12	7.81	10.76	3.71	4.27
40°	7.34	7.56	8.32	9.10	11.78	4.75	2.80
50°	7.34	7.68	8.43	9.75	10.87	4.09	2.45
60°	7.34	7.02	2.98	8.09	8.99	3.13	2.72
70°	7.34	6.90	6.91	6.62	8.60	9.15	7.11
80°	7.34	7.41	16.24	9.26	5.22	7.89	2.39

Table 6.6. The ratios for RMS values for the amplitudes of the PPPhD/PhD modulation functions.

The RMS amplitudes from which these ratios have been calculated are plotted in fig. 6.20

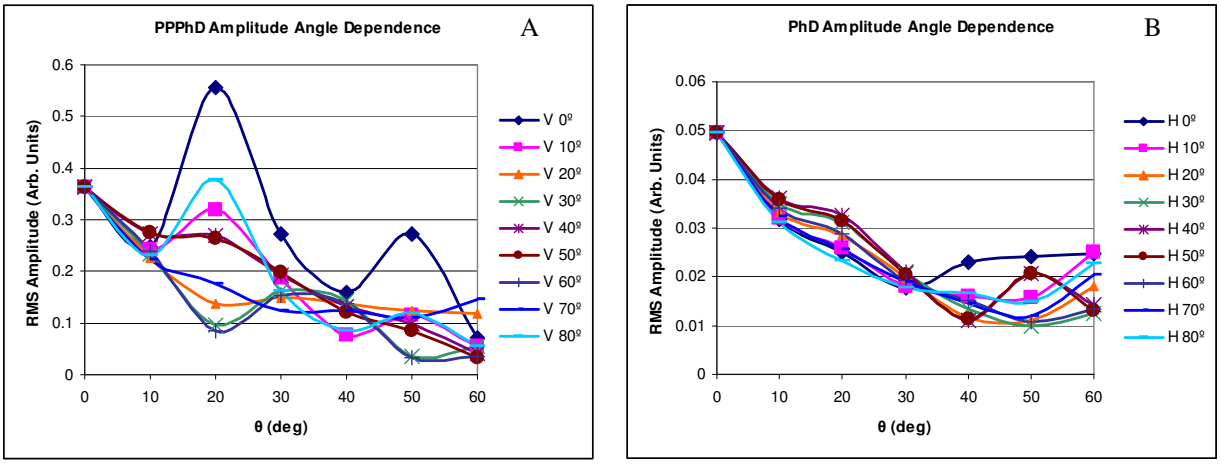

Fig. 6.20 and B correspond to the PPPhD and PhD RMS amplitudes, respectively. Note that the scale in A is a factor of 10 higher than that in B and that the range of intensities is considerably more pronounced for PPPhD.

As was the case in the Pt(111)c(5x√3)rect.3CO system and to an even greater degree, the modulation functions produced by the PPPhD method are more intense than those produced using PhD. Fig. 6.21 shows some typical PPPhD modulation functions compared with their corresponding PhD modulations.

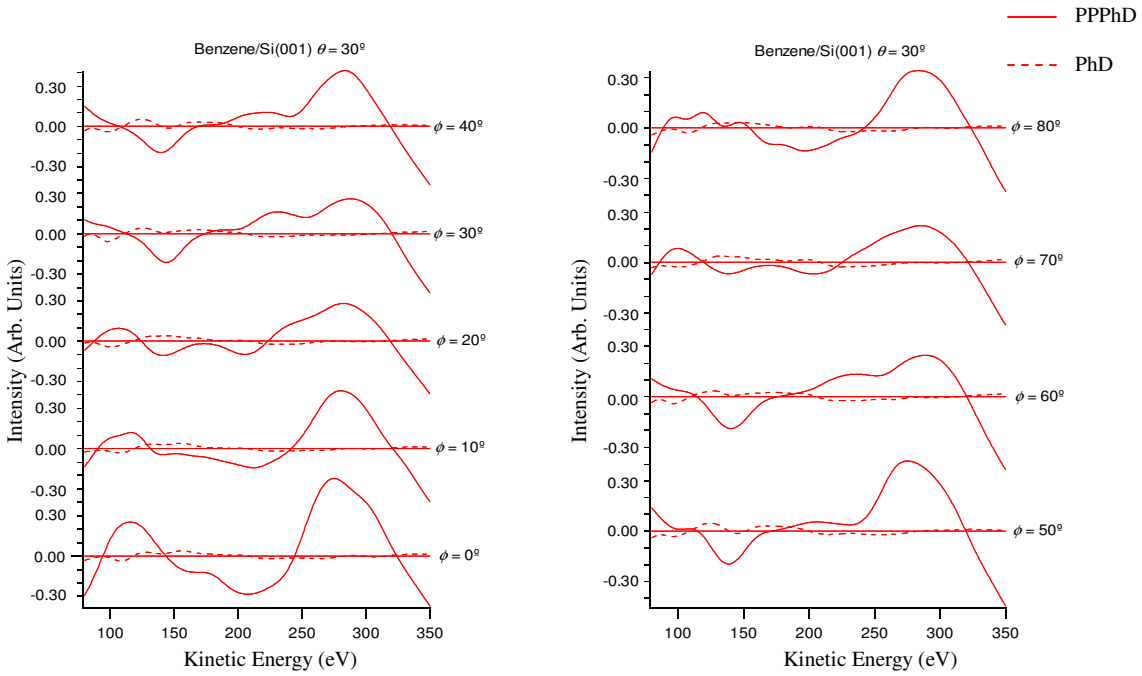

Fig.6.21. Comparison of PPPhD and PhD modulation functions produces from benzene adsorbed on Si(001). As before, the solid and dotted lines corresponds to PPPhD and PhD respectively.

The modulation functions used to compare the variance of PPPhD and PhD are presented in fig. 6.22 and were selected to include a different azimuthal angle for each polar angle used.

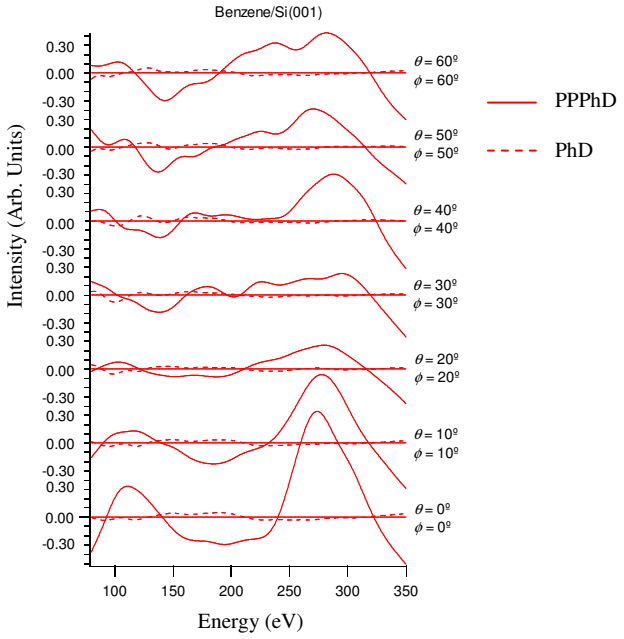

Fig.6.22. Modulation functions used to compare the sensitivity of PPPhD and PhD to the structural parameters of the benzene/Si(001) adsorption system.

The comparison of PPPhD and PhD as applied to the benzene/Si(001) system appears to be consistent with that for the CO/Pt(111) system which shows that PhD is more sensitive to

parameters involving mainly vertical displacements. The Si-$C_{butterfly}$ bond axis is tilted from the normal axis by 12º which means changing the bond length mainly involves a vertical displacement. Again, PhD exhibits a greater sensitivity to this kind of displacement than PPPhD (see fig. 6.23).

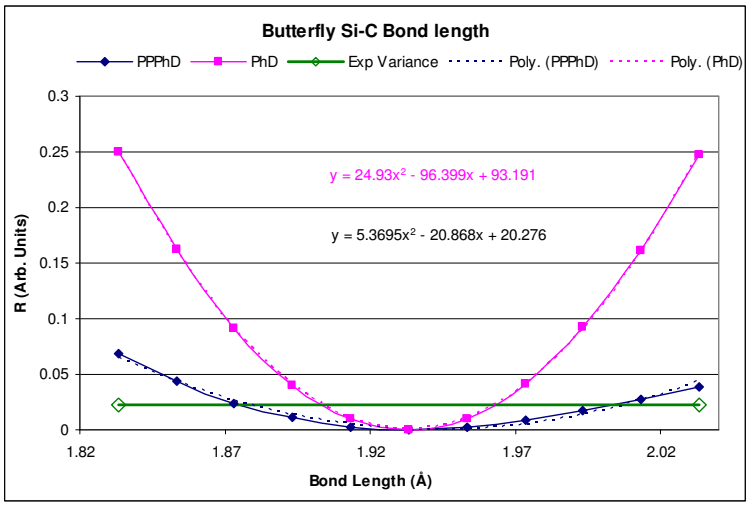

Fig. 6.23. PPPhD/PhD comparison for the butterfly bond length yielding a sensitivity ratio of 0.22, a PPPhD variance of +0.06/-0.07 Å and a PhD variance of ±0.03 Å.

The Si-C_{TB} bond axis on the other hand is tilted from the normal axis by an angle of 49º which means that changing the bond length results in a marginally greater lateral than vertical displacement leading to the expected result that PPPhD is the more sensitive method (see fig. 6.24).

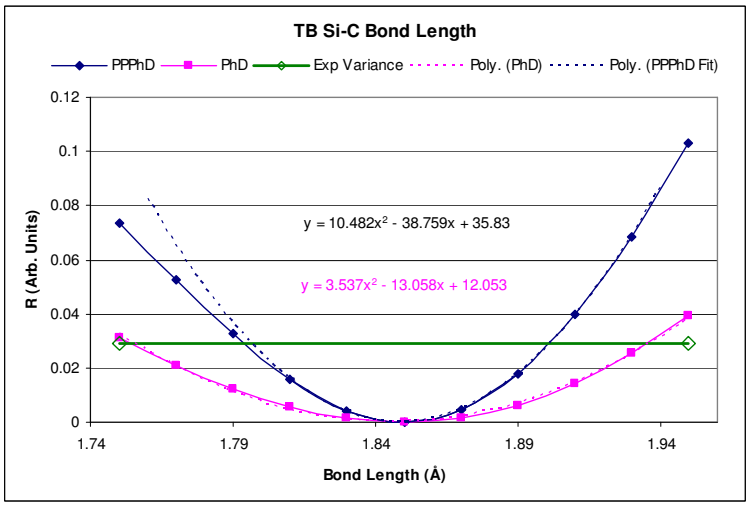

Fig. 6.24. PPPhD/PhD comparison for the TB Si-C bond length yielding a sensitivity ratio of 2.96, a PPPhD variance of ± 0.05 Å and a PhD variance of +0.08/-0.09 Å.

Further support for this concept is provided in figs. 6.25 – 6.26 which involve mainly lateral displacements. Again the PPPhD method is more sensitive than PhD.

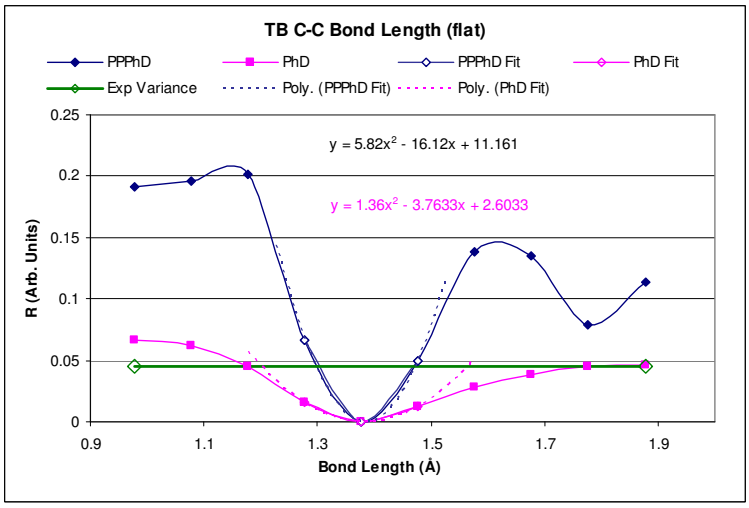

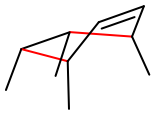

Fig. 6.25. PPPhD/PhD comparison for the TB C-C bond length (indicated by the red lines in the diagram on the right), yielding a sensitivity ratio of 4.28, a PPPhD variance of +0.09/-0.07 Å and a PhD variance of +0.20/-0.38 Å.

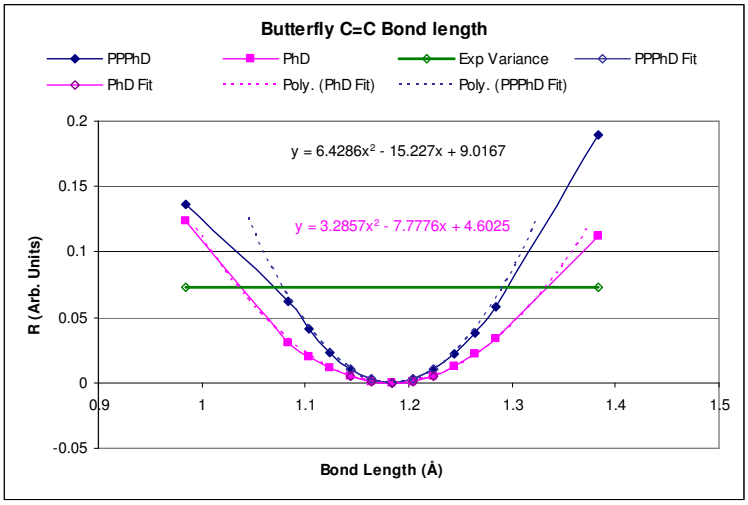

Fig. 6.26. PPPhD/PhD comparison for the butterfly C=C bond length yielding a sensitivity ratio of 1.96, a PPPhD variance of ± 0.11 Å and a PhD variance of +0.15/-0.14 Å.

Finally, figs 6.27 – 6.28 show that PPPhD is more sensitive than PhD when the parameters involved consist mainly of vertical displacements.

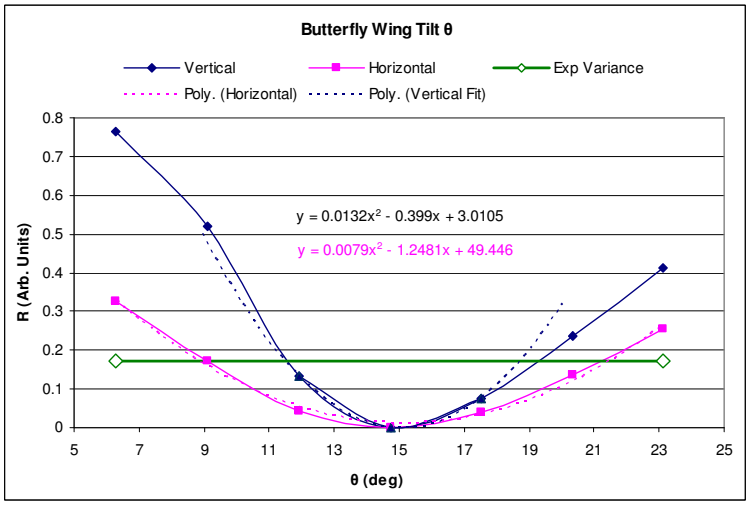

Fig. 6.27. PPPhD/PhD comparison for the butterfly wing tilt yielding a sensitivity ratio of 1.67, a PPPhD variance of +3.1º/-4.52º and a PhD variance of +6.4º/-5.5º.

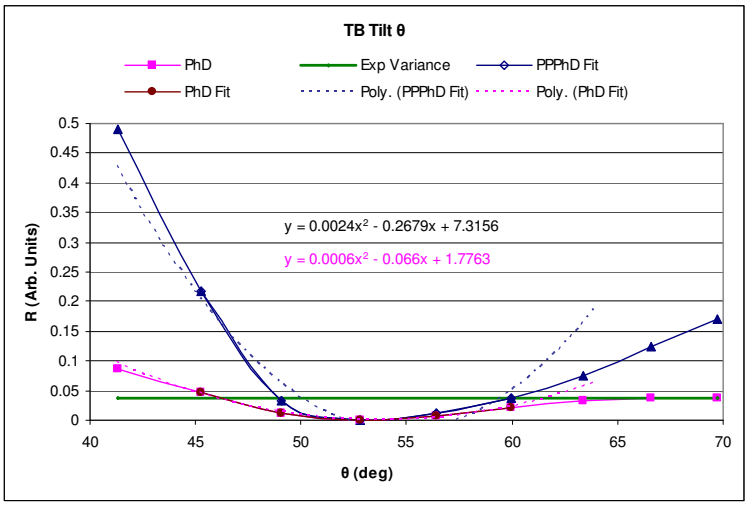

Fig. 6.28. PPPhD/PhD comparison for the TB wing tilt yielding a sensitivity ratio of 4, a PPPhD variance of +7.2º/-3.8º and a PhD variance of +12.4º/-6.8º.

As detailed in chapter 5, PhD was not sensitive enough to distinguish between separate domains and mixed domains. Comparing the theoretical spectra for the three mixed domains, A, B and C depicted in fig. 5.13, with the theoretical spectra for separate domains model for both PPPhD and PhD methods gives the R-factors tabulated in table 6.7.

Mixed Domain Model	PPPhD R-Factor	PhD R-factor
A	1.1932	0.0019
B	0.8153	0.0014
C	1.4297	0.0054

Table 6.7 Comparison of PPPhD and PhD R-Factors for the three domain models A, B and C using the theoretical modulation function from the separate domain model for comparison.

The R-factors for PPPhD are dramatically higher than those for PhD and significantly different from one another, meaning that PPPhD is clearly more sensitive to neighbouring adsorbates than PhD which is consistent with the developing idea that PPPhD is more sensitive to lateral structural information than PhD.

An inherent problem with PPPhD mentioned earlier is the reduction in signal intensity due to the absence of the directly emitted photoemission component. The theoretical average intensities for the CO/Pt(111) and benzene/Si(001) systems are presented in Table 6.8.

Spectra	θ	ϕ	Average Raw Intensity	PPPhD/PhD Intensity Ratio
CO/Pt(111) Atop PPPhD	0º	0º	0.248	0.125
CO/Pt(111) Atop PhD	0º	0º	1.977	
CO/Pt(111) Atop PPPhD	50º	50º	0.021	0.024
CO/Pt(111) Atop PhD	50º	50º	0.885	
CO/Pt(111) Bridge PPPhD	0º	0º	0.054	0.016
CO/Pt(111) Bridge PhD	0º	0º	3.348	
CO/Pt(111) Bridge PPPhD	50º	50º	0.008	0.009
CO/Pt(111) Bridge PhD	50º	50º	0.901	
Benzene/Si(001) PPPhD	0º	0º	0.016	0.009
Benzene/Si(001) PhD	0º	0º	1.811	
Benzene/Si(001) PPPhD	60º	60º	0.156	0.456
Benzene/Si(001) PhD	60º	60º	0.342	

Table 6.8 Comparison of theoretical average intensities for PPPhD and PhD for the Pt(111)c(5x√3)rect.3CO and Si(001)(2x1)-C_6H_6 systems.

While the intensities are only relative intensities and are not normalized to factors such as beam current or slit spacing (see fig.3.4), they do provide a valid means of comparing the expected intensities for both techniques. An intensity of around 1/100 of that expected for PhD (in the more extreme cases of CO/Pt(111) Bridge at θ = 50º and ϕ = 50º and benzene/Si(001) at θ = 0º and ϕ = 0º) might initially throw doubt on the feasibility of PPPhD, however with the correct optimisation; adjusting parameters such as beam intensity, dwell time, and magnification, compensation for such a reduction could be achievable.

Another important factor in considering the feasibility of PPPhD is its sensitivity to the physical orientation of the sample. For example, plotting the PPPhD and PhD modulations for the graphs in fig. 6.7 separately and without an offset shows the degree of variation in the modulation function as a result of changing the azimuthal angle (see fig.6.26). While a definite change in the amplitudes is apparent in PhD, the PPPhD amplitudes change to such a degree that they exhibit characteristics of a 180º phase shift.

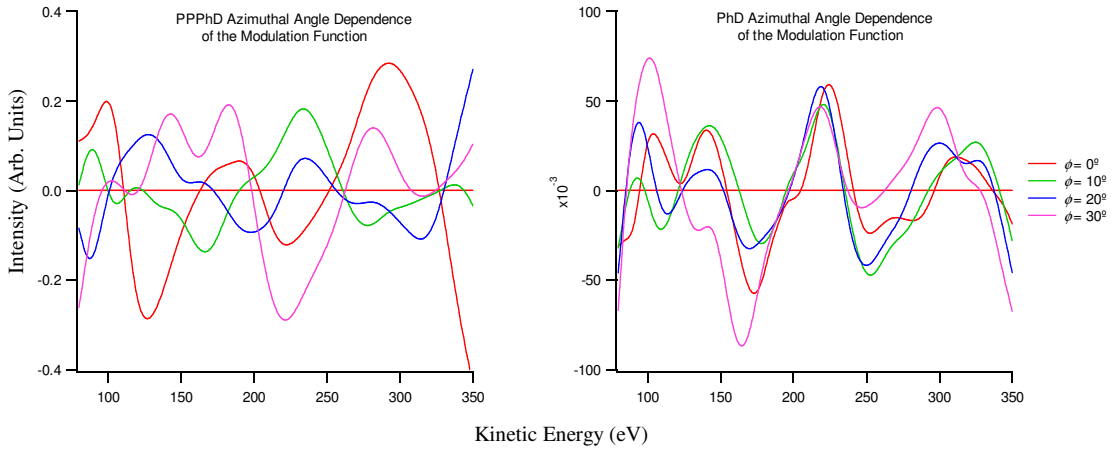

Fig. 6.26. Comparison of the azimuthal angle dependence for the CO/Pt atop species for PPPhD and PhD at a polar angle of 30º. Note that different scales have been used for clarity.

As can be seen from the graphs, PPPhD is more sensitive to the azimuthal positioning of the sample than PhD. To clarify this point, simulations for the CO/Pt(111) and benzene/Si(001) systems were carried out using the simulated modulation functions as a reference as in the preceding paragraphs. This time however an error of 3º in the polar angles and then the same in the azimuthal angles was introduced. The resulting R-factors are presented in table 6.9.

System	**R-factor**	
	θ	**ϕ**
CO/Pt(111) Atop PPPhD	0.1571	0.2151
CO/Pt(111) Atop PhD	0.1853	0.0106
CO/Pt(111) Bridge PPPhD	0.3165	0.1819
CO/Pt(111) Bridge PhD	0.2240	0.0083
Benzene/Si(001) PPPhD	0.1411	0.0459
Benzene/Si(001) PhD	0.0851	0.0227

Table 6.9. Effects of 3º errors in the polar and azimuthal emission angles.

While PPPhD is more sensitive to the polar angle than PhD in each case except for the atop system, the difference really becomes apparent, when the azimuthal dependence is considered. Clearly measurements undertaken for PPPhD would have to be considerably more precise than those for PhD. However the fact that PPPhD is more sensitive to this parameter might also result in greater accuracy.

6.3 Conclusion

A comparative theoretical analysis of PPPhD and PhD has been undertaken with a view to exploring the potential benefits of PPPhD and its feasibility as an alternative or complementary technique.

It has been shown that PPPhD yields modulation functions with intensities often being several times those observed in PhD. Whether or not these increased modulations translate to enhanced structural information has also been examined. PPPhD is shown to be more sensitive when the parameters involve mainly lateral displacements and vertical displacements not involving bond lengths. The sensitivity of PhD on the other hand exceeds that of PPPhD only when dealing with bond lengths involving mainly vertical displacements. Parameters involving similar vertical and lateral displacements show similar sensitivities for both methods.

A potential weakness which can be expected from the theory is the reduced signal to noise ratio resulting from the absence of the directly emitted photoelectron component. Whether or not this presents an insurmountable problem remains to be seen. However, the fact that normal PhD is sensitive to structural parameters other than nearest neighbour bond lengths means that the information from multiple scattering events is accessible. This suggests that with the proper optimization, PPPhD should prove to be a valuable if not vital complement to PhD.

Another potential weakness is the sensitivity of PPPhD to the sample positioning however this is simply a mechanical issue and does not reflect any inherent difficulties.

Ultimately, the preceding discourse is only theoretical and like any theory must be validated by experimentation. This could be achieved quite efficiently by performing the PPPhD and PhD scans in the emission angles presented in table 6.4 and fig. 6.19 for the CO/Pt(111) and benzene/Si(001) systems respectively. Optimization would have to be done in a trial and error fashion varying experimental parameters including photon beam current, dwell time, magnification, monochromator resolution, detector resolution etc. One further limitation which potentially limits the feasibility of PPPhD arises from the fact that increasing the signal to noise ratio will almost inevitably involve increasing the beam intensity as already mentioned. This in turn increases the likelihood of damaging the structure. This could easily be checked using

LEED and XPS. A further check for damage that might not present itself in LEED or XPS could be performed in which the modulation function for a full PhD spectrum for a freshly prepared sample could be compared with smaller sections, each too, measured after a fresh preparation of the sample.

7 Conclusion and Future Work

The structural determination of the Pt(111)c(5x√3)rect.-CO phase formed by 0.6 ML of adsorbed CO has been undertaken using scanned-energy mode photoelectron diffraction utilising the two distinct components of the C 1s photoemission peak. Earlier assignments of CO to atop and bridge sites have been confirmed as well as the respective 2:1 ratio of these assignments. Additionally, quantitative local structural details have been obtained. In particular, the Pt-C chemisorption bond lengths for the atop and bridging sites are 1.86 ± 0.02 Å and 2.02 ± 0.04 Å respectively. These values are similar to those obtained in previous studies for the 0.5 ML coverage c(4 x 2) phase involving an atop:bridge occupation ratio of 1:1. The results also indicate a definite tilt in the CO_{atop} species of 10.7º +1.5º/-3.1º consistent with earlier investigations using electron-stimulated desorption ion angular distribution, LEED, Monte Carlo and IR. The C-O_{Bridge} tilt was found to be 8.3º +12.7º/-29.8º, which, as allowed by the variance, is consistent with a vertical orientation. The C-O bond lengths are significantly longer than those reported for the c(4x2) system (1.24 +0.05/-0.04 Å compared with 1.15±0.05 Å), although the difference falls within the variance. The C-O bond length for the bridge species (1.25 +0.16/-0.14 Å) is sensibly longer than that for the terminal species but again the difference falls within the variance.

The local structure of benzene adsorbed on Si(001) has also been investigated using scanned-energy photoelectron diffraction. The standard butterfly (SB), tilted (T), tight bridge (TB), pedestal (P), twisted bridge (TB), and diagonal bridge butterfly (DDB) models were optimized and compared. The lowest R-factors were achieved for SB and TB models (0.2337 and 0.2641 respectively). Further optimization was performed for a mixed overlayer (0.25 ML) consisting of SB and TB domains in various proportions. A significant improvement in the R-factor was achieved for a combined model in which 58 ± 35 % of the overlayer is composed of the SB structure. Detailed structural parameters have also been obtained for both species including Si-C bond lengths and out of plane tilt angles. Also, but with less precision, intramolecular bond lengths and Si dimer bond lengths. As was the case with the CO/Pt(111) the determination of parameters involving lateral displacements is significantly less precise than that for vertical displacements. This might be remedied in future work by the use of PPPhD as a complementary technique.

A comparative theoretical analysis of PPPhD and PhD has been undertaken with a view to exploring the potential benefits of PPPhD and its feasibility as an alternative or complementary technique.

It has been shown that PPPhD yields modulation functions with intensities often being several times those observed in PhD. Whether or not these increased modulations translate to enhanced structural information has also been examined. PPPhD is shown to be more sensitive when the parameters involve mainly lateral displacements and vertical displacements not involving bond lengths. The sensitivity of PhD on the other hand exceeds that of PPPhD only when dealing with bond lengths involving mainly vertical displacements. Parameters involving similar vertical and lateral displacements show similar sensitivities for both methods.

A potential weakness which can be expected from the theory is the reduced signal to noise ratio resulting from the absence of the directly emitted photoelectron component. This however, might be offset in the integration procedure to some extent by the fact that the modulations are also greater, meaning the degree of variation in the peak intensity is greater. Whether or not the low signal intensity presents an insurmountable problem remains to be seen. However, the fact that normal PhD is sensitive to structural parameters other than nearest neighbour bond lengths means that the information from multiple scattering events is accessible. This suggests that with the proper optimization, PPPhD should prove to be a valuable if not vital complement to PhD.

Another potential weakness is the sensitivity of PPPhD to the sample positioning however this is simply a mechanical issue and does not reflect any inherent difficulties and in fact might be an exploitable advantage.

As has already mentioned, the PPPhD analysis is only theoretical and like any theory must be validated by experimentation which would be the natural starting point of future work. This could be achieved quite efficiently by performing the PPPhD and PhD scans in various emission angles for the CO/Pt(111) and benzene/Si(001) systems. A consequence of the poor signal to noise ratio in PPPhD will almost inevitably necessitate increasing the beam intensity which in turn increases the likelihood of damaging the sample. This could possibly be circumvented by panning the sample as the PhD scan progresses, however, while this would be a trivial matter at normal incidence, the situation would be more complicated for other emission

angles requiring precise and simultaneous adjustments in the x and y axes so as not to unduly effect the signal intensity by changing the sample distance from the analyser. Further optimization would have to be done on a trial and error basis on various other experimental parameters including photon beam current, dwell time, magnification, monochromator resolution, detector resolution etc. If these measures are successful an unprecedented level of structural detail might be achievable.

8 References

1 K.W. Kolasinski, p xiv, Surface Science, Wiley, (2002).
2 K.W. Kolasinski, p xv, Surface Science, Wiley, (2002).
3 http://globaltechforum.eiu.com/index.asp?layout=rich_story&doc_id =8648&title=Global+semiconductor+outlook--June+2006&categoryid=15&channelid=5
4 http://en.wikipedia.org/wiki/Moore's_Law, 10/09/2007.
5 http://www.intel.com/technology/mooreslaw/index.htm, 26/10/2007.
6 Vee S. C. Len, , R. E. Hurley, N. McCusker, D. W. McNeill, B. M. Armstrong and H. S. Gamble, Solid-State Electronics 43, 6 (1999) 1045-1049.
7 http://www.freepatentsonline.com/6281095.html (September 2007).
8 http://www.tech.co.uk/computing/upgrades-and-peripherals/processors/features/the-future-of-the-cpu?page=1, 01/11/2007
9 Pier Luigi Silvestrelli, Francesco Ancilotto, and Flavio Toigo. Phys. Rev. B, 62 (2000) 1596.
10 http://hyperphysics.phy-astr.gsu.edu/hbase/tables/photoelec.html, 07/05/2003.
11 http://xray.uu.se/hypertext/EBindEnergies.html, 08/05/2003.
12 Kurt W. Kolasinski, p55, Surf. Sci., Wiley, (2002).
13 http://whome.phys.au.dk/~philip/q1_05/surflec/node25.html, 26/10/2007
14 D.P. Woodruff and A M Bradshaw, Rep.Prog.Phys. 57 (1994) 1029 1080.
15 V. Fritzsche, J. Phys. Condens. Matter 2 (1990) 1413-1424.
16 V. Fritzsche, J. Phys. Condens. Matter 2 (1990) 9735-9747.
17 V. Fritzsche, Surf. Sci., 265 (1992) 187-195.
18 V.Fritzsche and P.Rennert. phys.stat.sol.(b) 135, 49 (1986).
19 N.A. Booth, R. Davis, R. Toomes, D. P. Woodruff, C. Hirschmugl, K.M. Schindler, 0. Schaff, V. Femandez, A. Theobald, Ph. Hofmann, R. Lindsay, T. GieBel, P. Baumgartel and A. M. Bradshaw, Surf. Sci., 387 (1997) 152 –159.
20 Jon Tobias Hoeft, PhD Thesis, The University of Warwick, p20, (2002).
21 Mathieu Pascal, PhD Thesis, p48, The University of Huddersfield, (2002).
22 G. S, Blackman, et al. Phys. Rev. Lett. 61 (1998) 2352.
23 H. Steininger, S. Leehwald and H. Ibach, Surf. Sci., 327 (1995) 193.
24 D.F. Ogletree, M.A. Van Hove, G.A. Somorjai. Surface Science 173 (1986) 351.
25 C.A. Lucas, N.M. Markovic and P.N. Ross. Surf. Sci., 425 (1999) L381.
26 M.Ø. Pedersen, M.-L. Bocquet, P. Sautet, E. Laegsgaard, I. Stensgaard and F. Besenbacher. Chem. Phys. Let., 299 (1999) 403-409.
27 N.V. Petrova, I.N. Yakovkin. Surf. Sci. 519 (2002) 90–100.
28 B. N. J. Persson, M. Tüshaus J. Chem. Phys., 92 (8) 1990.
29 N. R. Avery, J. Chem. Phys., 74 (7) 1981
30 M. Song, K. Yoshimi, M. Ito. Chem. Phys. Let., 263 (1996) 587-590.
31 A. Alavi, P. Hu, T. Deutsch, P.L. Silvetrelli, J. Hutter. Phys. Rev. Lett., 80 (1998) 3650.
32 M. Lynch and P. Hu Surf. Sci., 458 (2000) 1-14.
33 D.P. Woodruff, Phys. Rev. Let. 90 (2003) 116104.
34 M.Kiskinova, A. Szaco and J.T. Yates, Jr. Surf. Sci. 205 (1988) 215–229.
35 R.Brako and D. Sokcevic. Vacuum 61 (2001) 89-93.
36 I. Zasada, Surf. Sci. 498 (2002) 293-306.
37 Van Hove, http://electron.lbl.gov/graphs/figures/PtCO.html 30/05/2003.
38 Klaus Hermann (Fritz-Haber-Institut Berlin, Germany) and Michel A. Van Hove (Lawrence Berkeley National Laboratory, Berkeley, and University of California, Davis, USA).Made by K. Hermann (FHI) and M. A. Van Hove (LBL) (2002).
39 http://www.spsu.edu/math/tile/symm/ident17.htm 19/09/2007
40 F. Bondino. Surf.Sci. 459 (2000) 467-474.
41 A. Beutler, E. Lundgren, R. Nyholm, J.N. Andersen, B.J. Setlik, D. Heskett, Surf. Sci. 396 (1998) 117.
42 S. R. Longwitz, J. Phys. Chem. B, 108 (2004) 38.
43 P.R. Chalker, Diamond in Electronics and Optics, page 1,3, 4/11/1993
44 P Baumgärtel, R Lindsay, O Schaffy, T Gießel, R Terborg, J T Hoeft, M Polcik, A M Bradshaw, M Carbone, M N Piancastelli, R Zanoni, R L Toomesk and D P Woodruff. New Journal of Physics 1 (1999) 20.1-20.15.
45 http://www.psc.edu/science/Bernholc/Bernholc.html 07/03/2006
46 Schlier R E and Farnsworth H E 1959 J. Chem. Phys. 30 917

47 Y. Taguchi, M. Fujisawa, T. Takaoka, T. Okada and M. Nishijima J. Chem. Phys. 95 (9), 1 November 1991

48 G. P. Lopinski, T. M. Fortier, D. J. Moffatt, and R. A. Wolkow. J. Vac. Sci. Technol. A 16(3), (1998).

49 S. Gokhale, P. Trischberger, D. Menzel, and W. Widdra. Journal Of Chemical Physics Vol. 108, 13 (1998).

50 Sarah K. Coulter, Jennifer S. Hovis, Mark D. Ellison, and Robert J. Hamers. J. Vac. Sci. Technol. A 18(4), (2000).

51 Borovsky, Michael Krueger, and Eric Ganz. Physical Review B, Vol. 57, 8 (1998).

52 R.A. Wolkow, G.P. Lopinski, D.J. Moffatt. Surface Science 416 (1998) L1107-1113.

53 W.A. Hofer, A.J. Fisher, G.P. Lopinski, R.A. Wolkow. Surf. Sci. 484-485 (2001) 1181-1185.

54 W. A. Hofer, A. J. Fisher, G. P. Lopinski and R. A. Wolkow. Physical Review B, Vol. 63, 085314 (2000).

55 P. Kruse and R. A. Wolkow. Applied Physics Letters Volume 81, 23 (2002).

56 H.D. Jeong, S. Ryu, Y.S. Lee, S. Kim. Surface Science 344 (1995) L1226-L1230.

57 U. Birkenheuer, U. Gutdeutsch, N. Rösch. Surface Science 409 (1998) 213-228.

58 N. Witkowski, M. Nagasono, M. N. Piancastelli. Physical Review B, 68 (2003) 115408.

59 M. Shimomura, M. Munakata, K. Honma, S. M. Widstrand, L. Johansson, T. Abukawa And S. Kono. Surface Review and Letters, Vol. 10, Nos. 2 & 3 (2003) 499-503.

60 Y. K. Kim, M. H. Lee, and H. W. Yeom. Physical Review B 71, 115311 (2005).

61 J. Kong, A.V. Teplyakov, J.G. Lyubovitsky, S.F. Bent. Surf. Sci. 411 (1998) 286

62 Jung-Yup Lee and Jun-Hyung Cho. Phys. Rev. B 72 (2005) 235317.

63 http://www.chem.swin.edu.au/modules/mod2/bondlen.html (September 2007).

64 R.J. Hamers and U.K. Köhler, J. Vac. Sci. Technol. A **7**, 2854 (1989).

65 Feng Tao, Zhong Hai Wang, Guo Qin Xu. Surf. Sci. 530 (2003) 203.

66 http://mathworld.wolfram.com/SphericalHankelFunctionoftheFirstKind.html (April 2007).

67 http://hyperphysics.phy-astr.gsu.edu/hbase/math/sphhar.html (April 2007).

68 The Physical Basis of Polarized Emission**.** Petr Petrovich Feofilov. Page 19, 37.

69 R. D´ıez Muino, D. Rolles, F.J. Garcıa de Abajo, F. Starrost, W. Schattke, C.S. Fadley , M.A. Van Hove Journal of Electron Spectroscopy and Related Phenomena 114 (2001) 99.

70 Charles S. Fadley Progress in Surf. Sci. 16 (1984) 275.

Abbreviations

AES:	Auger electron spectroscopy
ARUPS:	Angle resolved ultra-violet photoelectron spectroscopy
BESSY:	Berliner Electronenspeicherring-Gesellschaft für Synchrotronstrahlung m.b.H.
CAT:	Constant analyser transmission
CVD:	Chemical vapour deposition
DFT:	Density function theoretical
EDC:	Energy distribution curve
EELS:	Electron energy loss spectroscopy
fcc:	Face-centred cubic
hcp:	Hexagonal close-packed
HE-TGM:	High energy toroidal grating monochromator
HREELS:	High resolution electron energy loss spectroscopy
L:	Langmuir
LEED:	Low-energy electron diffraction
MD:	Molecular-Dynamics
ML:	Monolayer
NEXAFS:	Near edge x-ray absorption fine structure
PhD:	Scanned-energy mode photoelectron diffraction
RAIRS:	Reflection absorption infrared spectroscopy
R-factor:	Reliability factor
SEXAFS:	Surface extended x-ray absorption fine structure
STM:	Scanning tunnelling microscopy
TPD:	Temperature programmed desorption

Appendix

TSP:	Titanium sublimation pump
UHV:	Ultra high vacuum
XPS:	X-ray photoelectron spectroscopy
XRD:	X-ray diffraction

List of Publications

Bond Lengths and Bond Strengths in Weak and Strong Chemisorption: N2, CO, and CO/H on Nickel Surfaces.
D. I. Sayago, J.T. Hoeft, M. Polcik, and M. Kittel, R. L. Toomes, J. Robinson, and D. P.Woodruff, M. Pascal, C. L. A. Lamont, and G. Nisbet. Phys. Rev. Lett, 90 (2003) 11.

Local adsorption sites and bondlength changes in Ni(100)/H/CO and Ni(100)/CO.
J.T. Hoeft, M. Polcik, D.I. Sayago, M. Kittel, R. Terborg, R.L. Toomes, J. Robinson, D.P. Woodruff, M. Pascal, G. Nisbet, C.L.A. Lamont. Surf. Sci. 540 (2003) 441.

Circular Dichroism in Core Level Photoemission from an Adsorbed Chiral Molecule.
M. Polcik, F. Allegretti, D. I. Sayago,1 G. Nisbet, C. L. A. Lamont, and D. P.Woodruff Phys. Rev. Lett, 92 (2004) 23.

Local structure determination of a chiral adsorbate: Alanine on Cu(110).
D.I. Sayago, M. Polcik, G. Nisbet, C.L.A. Lamont, D.P. Woodruff, Surf. Sci. 590 (2005) 76

Can circular dichroism in core-level photoemission provide a spectral fingerprint of adsorbed chiral molecules?
F Allegretti, M Polcik, D I Sayago, F Demirors, S O'Brien, G Nisbet, C L A Lamont and D P Woodruff. New J. Phys. 7 (2005) 109.

Structural analysis of Pt(111)-c(v3 x 5)rect.CO using photoelectron diffraction.
G. Nisbet, C.L.A. Lamont, M. Polcik, R. Terborg, D.I. Sayago, J.T. Hoeft, M. Kittel, R.L. Toomes, D.P. Woodruff. Surf. Sci. 601 (2007) 1296.

Acknowledgements

Firstly, I would like to thank my supervisor, Dr Christine Lamont for her hard work and guidance throughout the course of my PhD; I am truly thankful. I would also like to thank my second supervisor, Prof. Phil Woodruff and experimental supervisor, Martin Polcik who showed considerable patience when I was learning to use some *very* expensive equipment.

I spent several months in Berlin at the BESSY II facility and am grateful to the team I was working with. Specifically, I would like to thank Ralf Terborg, David Sayago, Martin Kittel, Rachel Toomes, Simon O'Brian and Jon-Tobias Hoeft. I would also like to thank Ralf, David and Martin for their help with the initial setup of the simulation program.

I am also grateful to the University of Huddersfield for my studentship and to the Fritz-Haber-Institute der Max-Plank-Gesellschaft for the use of their facilities.

Finally I would like to thank my wife, Brenda for her continued support, her patience truly has been tested, and my daughter Kaya, for lifting our spirits on those darker days.